Motion in the solid state studied by NMR and extended time scale MD simulation

ILOTT, ANDREW,JOHN

Motion in the solid state studied by NMR and extended time scale MD simulation

Andrew John Ilott

A thesis presented for the degree of
Doctor of Philosophy

Department of Chemistry
Durham University
England
February 2011

Motion in the solid state studied by NMR and extended time scale MD simulation

Andrew John Ilott

Submitted for the degree of Doctor of Philosophy
January 2011

Abstract

The ability to characterise dynamic processes in the solid state is crucial to our understanding of many important materials. Nuclear magnetic resonance (NMR) and molecular dynamics (MD) simulations are two, highly complementary techniques that can be used in this pursuit, with NMR providing robust measurements of kinetic parameters across a large range of time-scales while MD can give insight into the form that the motion takes. The aim of the work presented in this thesis has been to demonstrate the extent of this complementarity by combining both techniques to investigate interesting systems, and also to expand upon it by implementing extended time scale MD methods that allow slower dynamic processes to be accurately simulated.

Atomistic simulations of a urea inclusion compound and of octafluoronaphthalene (OFN), a molecular solid, illustrate the dynamic range and complicated nature of motions that can be present in solid phases of matter, and the inherent difficulty of modeling them without explicit knowledge of their form. Whilst the MD simulation can provide this information, there are computational limits to the range of time-scales it can conventionally access. The OFN system provides an example of this limit, as slow molecular motions observed by NMR experiments are shown to be inaccessible to long, ambient temperature simulations. To combat this deficiency, the metadynamics extended time scale technique has been implemented, allowing rare dynamic events to be observed in very short simulations, and the effects of complex correlated motions to be explored.

Declaration

The work in this thesis is based on research carried out in the groups of Dr. Paul Hogkinson and Prof. Mark Wilson in the Chemistry Department at Durham University, England. No part of this thesis has been submitted elsewhere for any other degree or qualification and it is all my own work unless referenced to the contrary in the text.

Acknowledgements and dedication

First and foremost I would like to offer my sincerest thanks to Dr. Paul Hodgkinson and Prof. Mark Wilson for their excellent supervision and support throughout my studies, without which this work would not have been possible. I have greatly enjoyed and benefited from our discussions and interactions over the course of my PhD and am grateful for their unwavering dedication and enthusiasm.

I am also grateful to Dr. Sebastian Palucha, who not only performed some of the simulations from which results are presented in this thesis, but also 'showed me the ropes', helped me to run my first simulations and passed on some useful scripts. I also owe much to all of the other members of Paul and Mark's research groups, both past and present, for their scientific input and friendship. Likewise, I would like to thank Prof. Robin Harris, Dr. David Apperley and Fraser Markwell for their insight and the pleasure of their company over the last 3 years.

I am deeply indebted to my parents for their unconditional love, support and encouragement; I don't know where I would be without it. This thesis is dedicated to them, and to my brother and sister. An honourable mention also goes to Maisy (feline), who was by my side for a lot of my thesis writing, and whose utter lack of sanity was sometimes the only thing that reminded me that I still had mine.

Last but not least, I would like to thank everyone in Durham who made my time so enjoyable throughout my many years there. You should know who you are, but just in case: Anuji, Richard, Elena, Ben, James, Jo, Dave S., Pete, Jess, Roy, Sian, Jesus, Maykel, Louise, Daniela, Brad, Becky, Dave B., Sandra and Judith (for always cheering up my days), Anne, Milena, Alessandra and many more. Thank you!

Contents

Chapter 1

General introduction: motion in the solid state

Although solid materials are often considered to be rigid because of their macroscopic properties, this is not the case at the atomic level, and every solid displays some motional behaviour at finite temperatures, even if this is limited to lattice vibrations. Many solid compounds display significantly more dynamics however, ranging from stretching modes of bonds and angles, dynamic conformational changes, molecular reorientations or even exchange processes or the translation of entire molecules. Often this dynamic behaviour can be a critical property of the material and can be responsible for its functionality, phase behaviour or other more general properties of the compound. Being able to understand and characterise dynamic behaviour in the solid state is therefore crucial in our hopes of explaining, and also manipulating, the properties of materials.

Nuclear magnetic resonance (NMR) spectroscopy is a particularly versatile technique for studying dynamic processes in the solid state and has many traits that make it suitable for this pursuit. Firstly, it can be used to probe motion occurring on a wide range of timescales (rates from Hz from MHz), that matches well with the typical regime associated with interesting dynamics in solids. The sampling properties are also highly favourable, as NMR records a collective signal from the whole ensemble of spin states in the experiment, probing the local environment of each atom. It also has the benefit of being nucleide-specific, meaning that samples can be selectively labeled to

investigate the behaviour of specific parts of molecules or structures. This specificity also allows complicated correlation experiments to be performed, where magnetisation can be transferred between different local species in a time-sensitive manner to obtain remarkably detailed information about atomic structure and dynamics.

The major drawback of using NMR to study motional processes is that the results do not provide a direct link to the precise form of the underlying molecular behaviour. Instead, results need to be fit against motional models that are based on evidence from other experimental studies, or simply from chemical intuition. Other techniques, such as Raman spectroscopy or inelastic neutron scattering (INS) also share this problem, where information can be obtained about the energy levels of molecular normal modes and the kinetic energy of molecules, respectively, but there is not a link to the precise atomic motion. X-ray diffraction on the other hand, is insensitive to the motion itself because it measures the long range order of crystalline compounds. However, it can measure the structural disorder which is a consequence of molecular motion, and in the right regimes can therefore infer that dynamics are present and give information about the form that it takes.

In simple systems where the the motional processes are relatively straight forward it is usually also straight forward to decide on the correct motional form and construct models that are accurate enough to obtain representative parameters from fits to experimental results. An example for such a process is the C_3 rotation of methyl groups in various compounds, which has been studied extensively by NMR, commonly using a simple 3-site jump model to explain the results. In systems where the motion is more complicated, coming up with an accurate motional model becomes increasingly difficult. This is where theoretical approaches can be extremely useful, and molecular dynamics (MD) simulation is one such technique that can simulate dynamics in complicated systems on timescales from picoseconds up to hundreds of nanoseconds. It can "see" how the atoms and molecules behave in the system, so can not only provide models by which to fit experimental results, it can also be used to study processes directly, and on a level of detail that could never be accessed by experiment. Likewise, the comparison of MD results with those from experiment provides a validation of the simulation results and gives credibility to the more thorough analysis they can provide.

For the reasons described above, NMR and MD simulation are highly complementary techniques, and there have been many successful studies combining them to gain insight into key areas. Two such areas that have relevance to the current work are now described.

Biological membranes One area in which both NMR experiments and MD simulation have made a considerable impact is in the study of biological systems. Here, dynamic behaviour explains much of the functionality of systems, such as the folding of protein molecules or the interactions between biologically important species. An example relevant to the current discussion of condensed phases is that of biological membranes. Membranes are complicated systems, normally composed of a lipid bilayer, but also containing other functional molecules that can demonstrate complex behaviour, such as by forming channels or receptors, acting as signal transducers, or accumulating as toxins. Understanding how these processes work is important, but made difficult by the size of the systems and their overall dynamic nature across a range of timescales.

Solid-state NMR is very well suited to looking at such systems, and whole membranes can be studied *in vitro*, rather than individually studying the constituent species. NMR studies have concentrated on two areas, firstly on studying the average structural and orientational properties of the membrane molecules as well as other membrane constituents. Obtaining this information from NMR is straight forward, as structural order parameters can be extracted directly from measured quadrupolar and dipolar couplings (this is discussed later in the context of liquid crystals, Section 3.5.1, and solid inclusion compounds, Chapter 4) [1, 2]. In early studies, simple models were proposed to link the experimental parameters with hypotheses about the nature of the molecular motion. More recently, MD simulations have been used to calculate time averaged order parameters that can be directly compared to NMR results [3–5]. Analysis of the simulation has then explained the orientational behaviour in terms of the specific motion of the lipid chains (specifically, conformation changes in the backbone) and other structural details.

The second use of NMR has been in the measurement of T_1 relaxation times [6].

This can lead to information about the dynamics of the membrane molecules, but once again the problem lies in linking the dynamics to the correct motional model. MD simulations have been utilised for this task, and combined studies are becoming more common [7, 8], in which autocorrelation functions calculated from simulation have been used to calculate relaxation times so that comparisons could be made with experimental values (see Section 3.5.2 and Chapter 5). As in the case of the order parameters, the molecular behaviour can be accurately extracted from the simulation, showing the contributions from motional processes acting on different timescales. Long simulations of approximately 100 ns in length have been required for this task because slower processes associated with the reorientation and diffusional motion of whole molecules have also been implicated as contributing to the relaxation mechanism.

The comparison of the simulations with the NMR parameters has also been used as a way to validate the simulations, giving confidence to other properties that can be calculated, such as diffusion coefficients [9] and information about the normal modes [4], which are difficult to probe experimentally.

The lengths of simulation required (hundreds of nanoseconds) to reliably estimate the properties of membranes are on the edge of what is currently possible for systems of this size. As such, extended-timescale simulation techniques are also being utilised in this field to extend the range of sampling, and both replica exchange methods [10, 11] and metadynamics [12] have been implemented in membrane systems.

Molecular machines An area that has attracted considerable attention for some time is that of artificial molecular machines. The hope of this field is to emulate nature in being able to produce a supramolecular functionality from collections of interacting molecules. In a similar way to conventional machines, these systems would be designed to react to an external stimuli, such as changes in light conditions or local magnetic fields, in such a way as to produce a collective and useful response.

Chemists have designed and synthesised many molecules that display properties that are similar to components of macroscopic machines. In the literature there are examples of molecular gears [13], turnstiles [14], gyroscopes[15], and even more complicated components such as molecular motors[16]. Clearly, to have control of the

properties of the supramolecular machines made up of these components, it is very important to be able to accurately characterise their kinetic behaviour.

As opposed to the biological examples discussed above, the characterisation of the motion in these cases starts with a well-defined model for the form of the motion, and the emphasis is on extracting the kinetic parameters as accurately as possible. NMR is perfect for such a task, and it has been one of the central techniques used to achieve this [17], with a range of experiments used to study dynamics on different time-scales. Specifically, in studies of potential components for molecular machines, ^{13}C and ^{2}H T_1 relaxation measurements have been used to extract barriers to rotational processes occurring at rates of MHz [18, 19], ^{2}H line shape analysis has given information about dynamics with rates of 100s kHz [20] as well as orientational information about the processes [19–21], and finally, the coalescence of peaks in ^{13}C spectra has been used to give information on much slower rates, of the order of 100s Hz [18, 20–22].

Without the need to establish a motional model, theoretical studies have mostly been carried out to ascertain more information about the potential energy landscape as a function of the key degrees of freedom [21, 23]. However, when more complicated forms of motion are present, full MD simulations have been used [19], providing appropriate motional models and supporting results from the NMR.

Although there are not many examples of combined use of MD simulation and NMR in this field, it is clear that their dual use will be invaluable in the future development of these systems, as they grow in size and complication. Fundamentally, as the number of degrees of freedom increases, describing the behaviour becomes more difficult, but also more exclusively suited to being studied by NMR and MD. It is also likely that extended timescale techniques will be crucial as the complexity of the systems grow, or when the motions of slower molecular components are involved.

1.1 Summary of the current work

This thesis begins by introducing the methods used. Firstly, **Chapter 2** provides an outline of the molecular dynamics technique, giving the basic theory and describing the methodology used to perform simulations. It also outlines general extended timescale

simulation techniques. Likewise, **Chapter 3** is used to introduce NMR spectroscopy and to describe the important nuclear interactions. This Chapter finishes by describing the manner in which solid-state NMR can be used to detect and measure molecular dynamics.

The first set of results are presented in **Chapter 4**, and they are from MD simulations of an acid-containing urea inclusion compound [24]. The simulations are longer and more thorough than any available in the literature, and they are used to demonstrate the rich complexity of dynamic behaviour in these systems. Results are compared to those from experiments in the literature, emphasizing the difficulty and danger of using overly simplified models to try and link experimental results to the underlying molecular motion. NMR parameters are also calculated directly from sets of simulations with slightly different starting conditions, and it is shown that the comparison provides a pathway to distinguish between simulations of varying accuracy.

In **Chapter 5**, results from NMR relaxation measurements are combined with the analysis of large MD simulations and information from several other techniques to investigate the motional properties and phase behaviour of solid octafluoronaphthalene [25]. Analysis of 100 ns MD simulations is used to uncover a complicated potential for the reorientation of the octafluoronaphthalene molecules, corroborating evidence from diffraction measurements. Whilst the resulting motional model could explain the observed motional interference with fast NMR relaxation times (rates of the order of MHz), it could not explain the existence of a slower process interfering in the microsecond regime. The model was thus expanded to allow one further step: the full rotation of the molecules, which was later observed as a rare event in MD simulations at elevated temperatures. The results in this Chapter demonstrate both sides of the complementarity of MD and NMR, firstly the use of MD in building motional models, and secondly the role of NMR in checking the validity of the simulation, in this case providing evidence that the simulation was not sufficiently long to sample all of the reorientation process. Relatively simple MD simulations are also used to compare different phases of octafluoronaphthalene, and show that the phase transition is intimately linked to the reorientation of the molecules.

Finally, in **Chapter 6**, the novel metadynamics method is introduced with refer-

ence to its previous uses in the literature and theoretical basis. Details are given of how the method was implemented to explore the free energy surface associated with the reorientation of rigid molecules, and results are discussed for the application to the octafluoronaphthalene system. The technique is shown to be extremely efficient, exploring the full rotational energy profile of a single molecule in an effective simulation time representing a speed-up of over five orders of magnitude when compared to the unbiased simulation. The accuracy and behaviour of slightly different variations of the algorithm are also described. Finally, results from multi-dimensional metadynamics are discussed, where the rotations of three neighbouring molecules are explored simultaneously to obtain subtle information about their correlated motions. Again, the technique is shown to perform extremely well, recreating a complicated potential energy surface that would not be possible with conventional MD simulation.

Chapter 2

Molecular dynamics

Molecular dynamics (MD) simulation is a method by which the motion of molecules and their constituent atoms can be 'observed' directly. The method itself is simple: empirical models of the interactions between the atoms in the simulation are used to calculate the associated forces, and from these, Newtons equations of motion are solved and used to propagate the atomic positions and velocities. In this manner, MD simulation is deterministic in nature, which differentiates it from related simulation techniques, such as Metropolis Monte Carlo, in which the new atomic positions are determined stochastically. MD simulation allows time-dependent properties of a system to be studied, as well as its statistical properties.

2.1 Statistical mechanics

Understanding how systems behave on a molecular level is one of the main motivations of conducting MD simulations, but it is also crucial to relate this microscopic behaviour to the macroscopic properties of the compound. This link is provided by statistical mechanics.

For a system containing N atoms at volume V and temperature T, classically there exists an infinite number of configurations that can be adopted. Each discrete configuration is defined exclusively in terms of the position vectors, $\boldsymbol{r}^N$, and momenta, $\boldsymbol{p}^N$, of the N atoms. One such configuration is labeled a phase point, $\Gamma(\boldsymbol{r}^N, \boldsymbol{p}^N)$, and the entire collection is called *phase space*.

From this full set of phase points, only a selection are sampled that correspond to a particular set of initial conditions and experimental observables. This subset of phase points is termed an *ensemble*. In MD simulations the most natural of these is the microcanonical, or constant-NVE ensemble, because the solutions of Newton's Equations of motion conserve energy (at least when solved analytically). Likewise in Metropolis Monte Carlo simulations [26], the canonical (constant-NVT) ensemble is sampled by the default method because the positions are selectively advanced by comparing the potential energy change of the system with the Boltzmann factor, which assures that the distribution of energies in the ensemble matches that of the Boltzmann distribution at that temperature.

The macroscopic, observable properties of the system under the particular conditions are a result of the average properties of the phase points in the ensemble. Assuming that the value of the observable, $A(\Gamma)$, can be calculated at each phase point, the only other thing that must be known to calculate ensemble averages is the probability, $\rho(\Gamma)$, of each particular phase point occurring, as they are not necessarily equally populated (this will depend on the ensemble that is being sampled from). This probability is given by,

$$\rho_{\text{ens}}(\Gamma) = \frac{w_{\text{ens}}(\Gamma)}{Q_{\text{ens}}}, \tag{2.1}$$

where w_{ens} is a weight function that describes the likelihood of a particular state and Q_{ens} is the *partition function*; a normalising factor that is simply the sum of all of the weights,

$$Q_{\text{ens}} = \sum_{\Gamma} w_{\text{ens}}(\Gamma). \tag{2.2}$$

The partition function relates the microscopic properties of the system to its macroscopic thermodynamic properties. It can also be used to estimate the ensemble average of any observable, A,

$$\langle A \rangle_{\text{ens}} = \sum_{\Gamma} \frac{w_{\text{ens}}(\Gamma) A(\Gamma)}{Q_{\text{ens}}}. \tag{2.3}$$

Obtaining an accurate estimation of the partition function is the main goal of simulations that aim to understand the macroscopic properties of a system. However, for

most systems the partition function cannot be evaluated exactly because the required sum in Equation 2.2 is over the contributions from an infinite number of phase points. Instead, simulation techniques rely on preferentially sampling the most important contributions, so that the rate of sampling for a particular phase point is proportional to $\rho_{\text{ens}}(\Gamma)$, which has a different distribution depending on the ensemble that is being sampled from. In this manner, the estimation of Q_{ens} improves as the simulation goes on, until eventually a stationary solution is found.

There is a distinct difference between sampling from the phase space stochastically, as in Monte Carlo, and deterministically, as in MD simulation; stochastic sampling can enable the system trajectory to 'tunnel' through energy barriers that would be difficult to traverse for the trajectory of an MD simulation. Nevertheless, provided every point in phase space is accessible to the MD trajectory with a finite probability, the simulation is *ergodic*. This property ensures that, if the simulations are run for long enough, the final results are independent of the initial conditions. It also means that the MD trajectory is sampling appropriately from the ensemble, and thus the ensemble average in Equation 2.3 can be replacing by an average over the discrete time-steps, τ, in the simulation,

$$\langle A \rangle_{\text{ens}} = \frac{1}{\tau_{\text{obs}}} \sum_{\tau=1}^{\tau_{\text{obs}}} A(\Gamma(\tau)). \tag{2.4}$$

2.2 The molecular dynamics method

The theoretical basis for MD simulations comes from classical mechanics, and to study the time evolution of a system of particles we must construct and solve the relevant equations of motion. The energy of the system is simply the sum of the potential, $\mathcal{U}(\boldsymbol{r}_N)$, and the kinetic, $\mathcal{K}(\boldsymbol{p}_N)$, energies, summed over the positions $\boldsymbol{r}^N = (\boldsymbol{r}_1, \boldsymbol{r}_2..\boldsymbol{r}_N)$ and momenta $\boldsymbol{p}^N = (\boldsymbol{p}_1, \boldsymbol{p}_2..\boldsymbol{p}_N)$ of all N particles. This sum gives the Hamiltonian:

$$\hat{\mathcal{H}}(\boldsymbol{r}, \boldsymbol{p}) = \mathcal{K}(\boldsymbol{p}^N) + \mathcal{U}(\boldsymbol{r}^N). \tag{2.5}$$

The kinetic energy is given by

$$\mathcal{K} = \sum_{i=1}^{N} \frac{\boldsymbol{p}_i^2}{2m_i}, \tag{2.6}$$

where m_i is the mass of particle i. The potential energy of the system is expressed in terms of a force field that usually uses approximate functional forms to model the bonding, angle and non-bonded interactions, which are parameterised by fitting their behaviour to empirical results. Force fields are described in Section 2.5.

Hamilton's equations are applied to Equation 2.5 to obtain a pair of coupled first order differential equations which describe the time evolution of the position and momentum of each particle:

$$\dot{\boldsymbol{p}}_i = -\frac{\partial}{\partial \boldsymbol{r}}\hat{\mathcal{H}} = -\frac{\partial}{\partial \boldsymbol{r}}\mathcal{U}(\boldsymbol{r}) = \boldsymbol{f}_i \tag{2.7}$$

$$\dot{\boldsymbol{r}}_i = -\frac{\partial}{\partial \boldsymbol{p}}\hat{\mathcal{H}} = \frac{\boldsymbol{p}_i}{m_i}. \tag{2.8}$$

These expressions are relatively straight forward, and solving them to obtain the trajectories of large systems of particles is trivial, even for large systems with complicated potentials. The difficulty lies in solving them in an efficient manner so as to minimise the computation required, and to do so accurately. Calculating the derivative of the potential energy is the most computationally demanding part of the calculation and so efficient algorithms minimise the number of times this has to be evaluated. Clearly the time evolution has to occur in discrete steps and the length of this timestep is crucial; it must be long enough to make the simulation useful but short enough to make it accurate. Shorter timesteps are also usually more efficient at conserving energy.

2.3 Integrating algorithms

There are many ways to find solutions to the classical equations of motion and thus evolve a system of interacting particles with time. The simplest type of method is the *finite difference* approach, where the information about the positions and dynamic properties of the system at time t are used to find the properties at a future time, $t+\Delta t$. These methods are based on a Taylor series expansion of the system properties, for instance for the positions

$$\boldsymbol{r}(t+\Delta t) = \boldsymbol{r}(t) + \boldsymbol{v}(t)\Delta t + \frac{\boldsymbol{f}(t)}{2m}\Delta t^2 + \frac{\Delta t^3}{3!}\dddot{\boldsymbol{r}} + \mathcal{O}(\Delta t^4).. \tag{2.9}$$

Likewise, expressions for the velocities and accelerations (and higher order time derivatives) can be obtained, and each of the expansions used to propagate the corresponding variables. However, this method does not observe Equation 2.7, and as the positions change the interaction strengths change without any modifications to the accelerations. This effect is corrected for by calculating the forces at the new positions, obtaining updated estimates of the acceleration, and correcting the previously obtained positions accordingly. The correction step is iterated through until an accurate solution is found. In practice, however, the calculation of the forces is the most expensive part of the computation and so the correction step is computationally demanding and the number of correcting iterations should be minimised.

An alternative form of the finite difference approach, that requires only a single force calculation at each time step, is the Verlet integrating scheme. This method, and others based on it, are amongst those most frequently used because they are simple, accurate and compact (in that they require only a small number of variables to be stored at any one time). It combines the Taylor expansion for the forward propagation of the positions in time, as in Equation 2.9, with the Taylor expansion for the previous step,

$$\boldsymbol{r}(t-\Delta t) \;=\; \boldsymbol{r}(t) - \boldsymbol{v}(t)\Delta t + \frac{\boldsymbol{f}(t)}{2m}\Delta t^2 - \frac{\Delta t^3}{3!}\dddot{\boldsymbol{r}} + \mathcal{O}(\Delta t^4).. \tag{2.10}$$

which can be summed to give an expression for the positions in the next step, $\boldsymbol{r}(t+\Delta t)$, provided the positions at the previous step, $\boldsymbol{r}(t-\Delta t)$ have been stored:

$$\boldsymbol{r}(t+\Delta t) = 2\boldsymbol{r}(t) - \boldsymbol{r}(t-\Delta t) + \frac{\boldsymbol{f}(t)}{m}\Delta t^2 + \mathcal{O}(\Delta t^4). \tag{2.11}$$

The odd terms of the expansion cancel, leaving an error of the order of Δt^4. Because the velocity terms are amongst those that are cancelled, they need to be calculated separately, from the difference of Equations 2.9 and 2.10,

$$\boldsymbol{r}(t+\Delta t) - \boldsymbol{r}(t-\Delta t) = 2\boldsymbol{v}(t)\Delta t + \mathcal{O}(\Delta t^3) + ... \tag{2.12}$$

$$\boldsymbol{v}(t) = \frac{\boldsymbol{r}(t+\Delta t) - \boldsymbol{r}(t-\Delta t)}{2\Delta t} + \mathcal{O}(\Delta t^2). \tag{2.13}$$

The velocities are needed at each time step in order to calculate the kinetic energy of the system, and thus the total energy, as well as other properties of the system such as the temperature. Without storing more variables in order to improve the calculation, this method only estimates the velocity to an accuracy of the order of Δt^2. However, there are two popular variants of the Verlet algorithm that deal with the velocities more satisfactorily: the Leapfrog and Velocity Verlet methods.

The Leapfrog variant of the Verlet algorithm is so called because the positions are evolved using velocities that are permanently out of sync by half a time step. The mid-step velocities are first calculated by the expression,

$$\boldsymbol{v}(t + \frac{1}{2}\Delta t) = \boldsymbol{v}(t - \frac{1}{2}\Delta t) + \frac{\boldsymbol{f}(t)}{m}\Delta t + \mathcal{O}(\Delta t^3), \tag{2.14}$$

which is obtained from the difference of the Taylor series expansions, this time for the velocities with half-time step intervals. The velocities at the time-steps themselves are calculated using the average of the mid-step values from either side, now with an error of the order of Δt^3. The velocity is used to update the positions,

$$\boldsymbol{r}(t + \Delta t) = \boldsymbol{r}(t) + \boldsymbol{v}(t + \frac{1}{2}\Delta t)\Delta t. \tag{2.15}$$

The advantages of this algorithm are that it is simple to program, requires only a single calculation of the forces per time step, and it is precise because the forms of the equations limit the propagation of rounding errors. This algorithm has been used in this thesis, for the MD work in Chapters 4-6.

The other variation on the Verlet algorithm, the Velocity Verlet method, propagates the particle positions using the velocities and forces from the current time step but then uses a combination of the current and future accelerations to work out the new particle velocities.

2.4 Statistical ensembles

As outlined above, the natural ensemble from which MD samples is the microcanonical ensemble, in which the number of atoms, volume and system energy remain constant.

Ensemble	Probability of visiting a phase point, Γ	Thermodynamic potential $(-\ln Q)$
Microcanonical, constant-NVE	$\delta(\hat{H}(\Gamma) - E)$	$-\frac{S}{k_\mathrm{B}}$
Canonical, constant-NVT	$\exp(-\frac{\hat{H}(\Gamma)}{k_\mathrm{B}T})$	$-\frac{A}{k_\mathrm{B}T}$
Isothermal-isobaric, constant-NPT	$\exp(-\frac{\hat{H}(\Gamma)+PV}{k_\mathrm{B}T})$	$-\frac{G}{k_\mathrm{B}T}$

Table 2.1: Table of properties for different types of ensemble, where S is the entropy, A is the Helmholtz free energy, $A = U - TS$, and G is the Gibbs free energy, $G = H - TS$ where H is the enthalpy.

This corresponds to an isolated system. However, with fixed energy, the number of interesting properties that can be explored is limited. For instance, in the work described here, we are interested in studying rare events that are energy-activated and so the simulation must be allowed to sample states with various energies. Fortunately this is possible with MD, and various methods have been implemented to keep various properties of the system constant, particularly the pressure and the temperature. Table 2.1 lists three ensembles that are popularly studied in MD, together with their sampling behaviour and the thermodynamic potential they can be used to obtain information about.

The physical interpretation of a system at constant temperature is one which is in contact with an external heat bath at the desired temperature, $\mathcal{T}$. Likewise, simulations under constant pressure can be thought of as being in contact with a piston that can react to changes in the system by modifying the volume. There are various methods by which the temperature and pressure of a simulation can be constrained to constant values. In the case of temperature, the most direct way is to scale the velocities of the particles by intermittently reassigning some or all of their velocities stochastically according to the Maxwell-Boltzmann distribution for the appropriate temperature. The Berendsen [27] thermostat scales the velocities non-stochastically by the factor,

$$\chi = \left(1 + \frac{\Delta t}{t_T}\left(\frac{T}{\mathcal{T}} - 1\right)\right)^{\frac{1}{2}} \tag{2.16}$$

which efficiently drives the system towards the correct kinetic energy distribution for

the temperature, $\mathcal{T}$, at a rate controlled by the parameter t_T which is a time constant. The Berendsen thermostat is most useful for equilibrating systems to the correct temperature but, like the other velocity scaling techniques, it does not generate states in the canonical ensemble.

The Nosé-Hoover thermostat [28] does generate states in the canonical ensemble, however, and works by introducing a frictional term in the equations of motion to constrain the overall temperature,

$$\dot{\boldsymbol{r}} = \frac{\boldsymbol{p}}{m} \tag{2.17}$$

$$\dot{\boldsymbol{p}} = \boldsymbol{f} - \xi \boldsymbol{p} \tag{2.18}$$

where the friction coefficient, ξ, is given by

$$\dot{\xi} = \frac{f}{Q}(k_{\mathrm{B}}\mathcal{T} - k_{\mathrm{B}}T) \tag{2.19}$$

where f is the number of degrees of freedom in the system and Q is the thermal inertia parameter which controls the timescale over which the temperature is allowed to fluctuate. This method can also be extended by modifying the friction coefficient to include terms for volume fluctuations and adding in an extra degree of freedom corresponding to an inertia for the volume fluctuations. These additions can ensure that the pressure of the system is also constrained, generating states from the isothermal-isobaric, constant-NPT ensemble. The Nosé-Hoover thermostat and barostat are amongst the most widely used in MD simulation for generating constant pressure and temperature ensembles.

There are also other methods for sampling at constant temperatures and pressures that involve coupling the system to an external variable, corresponding to the 'thermal inertia' of the heat reservoir in the case of the thermostat, and the inertia of the coupled piston in the case of the barostat [29, 30].

2.5 Force fields

If a system is to be accurately simulated so that the dynamic processes observed are representative of the real system, the interactions between the constituent atoms must also be representative of the real interatomic forces. However, there is a trade-off between accuracy and computational expense: the MD time step must be shorter than the time scale of the fastest interaction, so introducing high frequency vibrations or any electronic terms, will result in much shorter time-steps being required and therefore much shorter overall simulation lengths. Conventional MD does not consider the motion of electrons, although some variants have been developed with the introduction of electronic degrees of freedom [31]. Functional forms for the different interactions are also picked for their computational efficiency.

The model used to describe the interactions in MD is called a *force field*, and it consists of a parameterised set of interactions for different atomic species in different molecular environments. There are a few different approaches and "flavours" of force field in general use:

- **All-atom** force fields treat each atom in the system separately, with a single interaction site for each. The intramolecular interactions are often parameterised by fits to *ab initio* data, while the charges and other non-bonded parameters are tuned by the ability of the simulation to recreate empirical results. Examples of general-use all-atom force fields are OPLS-AA [32], AMBER [33] and CHARMM [34].

- **United-atom** force fields combine multiple atomic sites into a single interaction site. For example, the CH_2 in the methylene groups of an alkane can be combined into a single interaction site. The interactions between these "beads" can then be fit to all-atom results for the same compound (i.e. dihedral angle distributions). Whilst the inherent approximations prevent some properties of the system being investigated, reducing the number of interaction sites greatly enhances the speed of the simulations, allowing larger systems to be simulated for longer in comparison to all-atom approaches. Many all-atom force field have united atom variants, other popular examples are the TraPPE-UA force field [35] and GROMOS [36].

- **Polarisable** force fields introduce an extra degree of freedom that allows the charge distribution around the particles to fluctuate, either in magnitude or spatially. The fixed charges used in most force fields can poorly reproduce interactions that are influenced heavily by charge polarisation effects, which can be the case in simulations of high dielectric medium, such as water, and also in the interactions of metal atoms. There are various ways in which this class of force fields can be implemented, a good review describing many of these methods is given in ref. [37].

Coarse graining methods and *ab initio* MD methods also exist, and treat the interactions differently again. However, they also involve a slightly different methodology, by either including quantum calculations to describe the motion of the electrons in the case of the latter, or by changing the types of interactions considerably, as in the former.

Force fields are normally developed for specific types of molecules and the parameters are fit to certain values under particular thermodynamic conditions. This can mean that they are not very transferable, to new atom types or to the investigation of different observables that they were not fitted to. The key to conducting good simulation lies in rigorously ensuring that the force field used is fit for purpose. The simulations performed as part of this work have been done on condensed phases of small organic molecules. It was judged that the OPLS-AA force field would be most suitable for simulating these systems. In each implementation further fitting of the interaction parameters was also performed. Details of the OPLS-AA force field are now discussed.

The OPLS-AA force field The original formulation of the OPLS-AA force field focused mainly on Monte Carlo fitting of the internal degrees of freedom of a large number of small organic molecules, and combining their accurate parameterisation with fits of the non-bonded interactions between atoms. Many of the other parameters were taken from other force fields such as AMBER [33] and CHARMM [34]. Their aim was to create a good general force field that could be used for simulations of much larger protein molecules.

As with most force fields, the overall system potential from OPLS-AA is constructed as a sum of the terms for all of the different components,

$$\mathcal{U}(\boldsymbol{r}^N) = \mathcal{U}_{\text{non-bonded}}(\boldsymbol{r}^N) + \mathcal{U}_{\text{bonded}}(\boldsymbol{r}^N). \tag{2.20}$$

The non-bonded terms include the van der Waals interactions between two nuclei, approximated by the Lennard-Jones equation, and the contribution from the Coulomb interaction in the case of charged nuclei

$$\mathcal{U}_{\text{non-bonded}} = \sum_i \sum_{j>i} \left(v_{\text{lj}}(\boldsymbol{r}_i, \boldsymbol{r}_j) + v_{\text{coulomb}}(\boldsymbol{r}_i, \boldsymbol{r}_j) \right), \tag{2.21}$$

where

$$v_{\text{lj}}(\boldsymbol{r}_i, \boldsymbol{r}_j) = 4\epsilon_{ij} \left[\left(\frac{\sigma_{ij}}{r_{ij}} \right)^{12} - \left(\frac{\sigma_{ij}}{r_{ij}} \right)^{6} \right], \tag{2.22}$$

$$v_{\text{coulomb}}(\boldsymbol{r}_i, \boldsymbol{r}_j) = \frac{Q_i Q_j}{4\pi\epsilon_0 r_{ij}}. \tag{2.23}$$

σ_{ij} is the radius of the interaction and ϵ_{ij} is the well depth, Q_i is the charge on atom i and ϵ_0 is the permittivity of free space. The charges and Lennard-Jones parameters were at first estimated from previous studies but then fit to results of large Monte Carlo simulations of the different organic test molecules, comparing simulated and experimental values of the density, heat of vaporisation, molecular volume and heat capacity. In OPLS-AA the charges of a given functional group are transferable between different molecules. The same non-bonded parameters are used for the intra-molecular interaction between atoms separated by more than three bonds, but they are scaled by half for atoms separated by 3 bonds (including the charges). The Lennard-Jones parameters are calculated for the interactions between like atoms, i.e. σ_{ii} and ϵ_{ii}, and the terms for heterogeneous pairs of atoms are given by the geometric mean mixing rules, $\sigma_{ij} = \sqrt{\sigma_{ii}\sigma_{jj}}$ and $\epsilon_{ij} = \sqrt{\epsilon_{ii}\epsilon_{jj}}$.

The rest of the contributions to the potential energy are from the bonding terms,

$$\mathcal{U}_{\text{bonded}} = \sum_{\text{bonds}} v_{\text{bond}} + \sum_{\text{angles}} v_{\text{angle}} + \sum_{\text{torsions}} v_{\text{torsion}}, \tag{2.24}$$

where the bond stretching and angle bending terms are approximated with the harmonic potential and the torsional potential as a cosine series,

$$v_{\text{bond}} = K_r(r - r_{\text{eq}})^2, \tag{2.25}$$

$$v_{\text{angle}} = K_\theta(\theta - \theta_{\text{eq}})^2, \tag{2.26}$$

$$v_{\text{torsion}} = \frac{V_1}{2}[1 + \cos(\phi)] + \frac{V_2}{2}[1 - \cos(2\phi)] + \frac{V_3}{2}[1 + \cos(3\phi)]. \tag{2.27}$$

The force constants K_r and K_θ and equilibrium positions, r_{eq} and θ_{eq} are taken from the AMBER [33] and CHARMM [34] force fields, while emphasis was placed on obtaining good fits for the torsional potentials by first fitting the V coefficients to rotational energies calculated from *ab initio* methods, and then tuning them against the structural properties as obtained from gas phase MC conformational exploration and against the liquid properties as described for the non-bonded interactions.

2.6 Extended timescale techniques

Although the general properties of a molecular system are often of interest, MD can also be used to investigate specific processes involving particular atoms or molecules in the system. Processes of interest can be things like chemical reactions, the aggregation of particles, or a complex conformational change in a molecule such as those observed in protein folding (which can involve the concerted twist of the molecule's backbone dihedral angles and the formation of intra-molecular hydrogen bonds). Often large energy barriers have to be overcome to allow such processes, but standard MD simulations that sample from the canonical or isothermal-isobaric ensembles (which are used to simulate these processes as they explore phase points with different energies) visit states exponentially less often as their energy increases (see Table 2.1). These processes are thus sampled very rarely in simulation, and are termed *rare events.*

A key quantity when considering the types of process described above is the *potential of mean force* (PMF). The PMF represents the effective potential energy surface for the process, and is a function of a *reaction coordinate*, $S(\boldsymbol{R})$, that is characteristic of the process and is a function of a subset of the system coordinates, $\boldsymbol{R}(\boldsymbol{r}^N)$. If the event

of interest was a chemical reaction between two atoms, the reaction coordinate would simply be the distance between the two species, and the PMF would map the effective potential energy change as a function of that distance. In that case, the energy surface would be dominated by contributions from the non-bonded charge and van der Waals interactions, but would also include averaged contributions from interactions with the rest of the system.

In the canonical and isothermal-isobaric ensembles, the probability that the simulation visits a particular point in phase space is governed by the energy of that state (see Table 2.1). If a high level of sampling has been achieved by the simulation (i.e. the estimate of the partition function has reached a stationary value), so that accurate estimates are known for the probabilities of all of the different states occurring, the PMF can be calculated as

$$F(S_1, S_2, ...S_N) = -k_{\mathrm{B}}T \ln P(S_1, S_2, ...S_N), \tag{2.28}$$

which is just a combination of the energies of discrete steps along the reaction pathway. Practically, this can be achieved quite simply by constructing a histogram for the S^N values along the reaction pathway to get $P(S_1, S_2, ...S_N)$, and then taking the logarithm and scaling by $k_{\mathrm{B}}T$.

Clearly the flaw in the method described above is that when high energy states are involved, the sampling is not sufficient to give accurate values for the probabilities. Often in these situations, phase points along the reaction pathway can be so high in energy that they are not sampled at all. However, methods have been developed to improve the sampling in these regions, so that the full PMF can be calculated. These methods fall into two broad classifications in which the system trajectory is either *restrained* to sample regions along the reaction coordinate (umbrella sampling methods [38]), or *constrained* to sample discrete positions along the reaction pathway (methods involving thermodynamic integration [39]). The basics of umbrella sampling are now described, as they are directly relevant to the extended timescale approach implemented in this thesis.

2.6.1 Umbrella Sampling

In umbrella sampling [38] an artificial biasing potential, $V_{\mathrm{b}}(S)$, is added to the system potential in order to improve the rate of sampling of the areas of phase space that are of interest. Ideally this potential should compensate for the PMF so that the system trajectory can move unhindered along the reaction pathway and achieve a good level of sampling of S.

The inclusion of V_{b} means that the system trajectory no longer visits phase points according to their equilibrium free energy. However, the unbiased, equilibrium distribution functions can be recovered, using the relationship

$$\langle P(S)\rangle_E = \frac{\langle P(S)\exp(-\frac{V_{\mathrm{b}}(S)}{k_{\mathrm{B}}T})\rangle_V}{\langle \exp(-\frac{V_{\mathrm{b}}(S)}{k_{\mathrm{B}}T})\rangle_V}, \tag{2.29}$$

where the angled brackets on the right hand side are averages over the biased simulations.

In practical applications, V_{b} cannot completely compensate for the PMF, because that is the unknown quantity that is being investigated. Instead, V_{b} is chosen to maximise the sampling of the appropriate areas of phase space, the only practical limitation for it's choice being that it should sample S uniformly to avoid excessive errors when the exponential is calculated in Equation 2.29. It is normally too difficult to guess the form of the PMF in order to allow a suitably efficient V_{b} to be chosen that will uniformly sample the full reaction pathway. Instead, the calculation is split up into many 'windows' centred at discrete values of S, labeled S_i. The form of the biasing potential in these windows is often chosen as a harmonic function that couples the simulation trajectory to the specific values of S_i,

$$v_i(S) = \frac{1}{2}K(S - S_i)^2, \tag{2.30}$$

A series of simulations are performed, the unbiased distribution functions are recovered using Equation 2.29 and then they are combined by comparing the regimes in which the $v_i(S)$ overlap, to recreate the sampling profile along the reaction pathway and thus to estimate the PMF.

One of main problems with this, the most basic form of the method, is that recombining the sampling from the different windows introduces error into the overall evaluation of the PMF. The regions of the simulations corresponding to the required overlaps between the different windows also represent a considerable redundancy in simulation effort. There are many methods used to combat these problems, such as the *weighted histogram analysis method* (WHAM) [40] in which the results from all of the different windows are dynamically weighted and combined into a histogram that estimates the unbiased distribution function, including values from all of the overlapping regions.

There are also methods that modify umbrella sampling to improve the efficiency of the biasing potentials and match them more closely to the underlying energy surface: methods such as *adaptive umbrella sampling* [41], in which the form of a single biasing potential is iteratively improved until it is effective in compensating for the PMF. The metadynamics method [42] is also similar, implementing a time-dependent biasing potential that converges to the underlying free energy surface spanning the reaction coordinates. The metadynamics algorithm is described in more detail in Chapter 6, along with an implementation of the method that explores the free energy surface associated with the reorientation of rigid molecules.

Chapter 3

Solid-state NMR

Nuclear magnetic resonance (NMR) is a spectroscopic technique that measures transitions between the spin states of atomic nuclei. The energy of these states and thus of the energy gap between them, is highly dependent on the local environment that the nucleus is in and as such NMR can resolve very slight differences between chemical environments. Many of the interactions in NMR are anisotropic and so motion on the right sort of timescales can impact on the NMR signal, giving access to information on molecular dynamics.

This section aims to give a brief overview of all of the interactions in NMR, indicating why NMR in the solid state is significantly different and more complicated than that used routinely as an analytical tool for chemists in the solution state. More specific details will then be given about the tools that have been used in the rest of this work to study dynamics on various time scales.

3.1 Angular momentum and the Zeeman interaction

Atomic nuclei have an intrinsic angular momentum. This is often referred to just as their *spin*, with the behaviour of a given nucleus characterised by its *spin quantum number*, I. For a nucleus this fundamental property can vary from 0 upwards in half integer steps, $I = 1/2, 1, 3/2...$ but rarely exceeds I=4. The spin quantum number dictates the magnitude of the angular momentum vector for the nucleus, which is quantised in multiples of $\hbar$ by the relationship $[I(I+1)]^{\frac{1}{2}}\hbar$. This vector has an associated mag-

netic moment, $\boldsymbol{\mu}$, that is parallel and directly proportional to the length of the angular momentum vector, $\boldsymbol{I}$,

$$\boldsymbol{\mu} = \gamma \boldsymbol{I}, \tag{3.1}$$

where γ is the gyromagnetic ratio, unique to the nucleus in question (note that γ can also be negative, making $\boldsymbol{\mu}$ and $\boldsymbol{I}$ anti-parallel).

The direction of $\boldsymbol{I}$, and thus $\boldsymbol{\mu}$, are quantized: their projection onto a set of arbitrary axes can only take discrete values. For an isolated spin these different orientations are degenerate and so the vectors have no preferred orientation. However, in the presence of a magnetic field the degeneracy of the different states is lost. In practice, this is done by applying a large external magnetic field, $\boldsymbol{B}_0$, that, by convention, points along the $+z$ direction. The splitting of the nuclear spin energy levels by this field is called the Zeeman effect and it is the dominant interaction in NMR.

The splitting in energy is caused by the interaction of the nuclear magnetic moment with the external field. The energy depends explicitly on the orientation of $\boldsymbol{\mu}$ with respect to the field,

$$E = -\boldsymbol{\mu} \cdot \boldsymbol{B}_0 = -|\boldsymbol{B}_0||\boldsymbol{\mu}| \sin \theta_{\boldsymbol{\mu},\boldsymbol{B}_0}, \tag{3.2}$$

which is equivalent to the quantized projection of μ onto the z-axis,

$$E = -\mu_z B_0. \tag{3.3}$$

There are $2I + 1$ such projections of $\boldsymbol{\mu}$ onto z, each denoted with a magnetic quantum number, m_I, that takes the values $m_I = -I, -I + 1..0..I$. The quantization is again in units of $\hbar$, making the energy of the different levels,

$$E = -m_I \hbar \gamma B_0. \tag{3.4}$$

NMR spectroscopy probes transitions between these levels. The selection rule in this case, $\Delta m = \pm 1$, allows the transitions to only occur between adjacent energy levels where,

$$\Delta E = \hbar \gamma B_0 = h\nu_0, \tag{3.5}$$

which is equal to the energy of the photons involved. We thus expect to measure a photon with frequency,

$$\nu_0 = \frac{\gamma B_0}{2\pi}. \tag{3.6}$$

This is called the Larmor frequency and is specific to the nucleus in question (because of their different gamma values) and magnetic field strength used. The energy gap described here is due entirely to the Zeeman Effect and it is responsible for an identical splitting between each of the $2I + 1$ nuclear spin energy levels.

When an external magnetic field is applied across the sample the energy gap between the quantised energy levels results in a slight difference in their equilibrium populations. This population difference is governed by the Boltzmann distribution and depends upon the relative energies of the states. However, since the energy gap is very small, the resultant population difference is tiny. For instance, for a proton in a standard 11.7 T field ($\nu = 500$ MHz) the energy difference between the two states for the spin-$^1/_2$ nuclei is approximately 0.005 J mol^{-1}. When compared to the standard thermal energy at room temperature of ~ 2.5 kJ mol^{-1} it is clear just how small the resultant population difference is, and there is only about 10 parts per million preference for the lower state. This fundamentally limits the sensitivity of NMR, significantly so for rare spins. Traditionally this limitation has been combated by using higher field strengths, or by trying to improve the polarisation by other means, such as DNP or the use of NMR nuclei that can be hyperpolarised.

In a conventional NMR experiment, radio frequency radiation in the form of short pulses is applied to the system to perturb it away from its equilibrium state. The coherent precession (at their NMR frequency, ν_0) of the magnetic moments of the nuclei induces an oscillating current in a receiver coil close to the sample. The time-domain signal is recorded, and a Fourier transform is taken to recover the transition frequencies.

3.2 Nuclear interactions

As with any quantum mechanical system, the Schrödinger equation, $\hat{\boldsymbol{H}}\Psi = E\Psi$, must be solved to obtain the eigenvalues and eigenvectors that correspond to the allowed

Zeeman	Quadrupolar	Dipolar	CSA	J-coupling
10^8 Hz	10^6 Hz	10^4 Hz	10^4 Hz	10s Hz

Table 3.1: Approximate magnitudes of the different interactions between nuclear spins.

states and their respective energies. To solve the Schrödinger equation for the spin interactions in NMR, *perturbation theory* is first used to simplify the interplay of the different interactions. The Zeeman effect is treated as the dominant interaction, while the other spin interactions provide first order corrections to the resultant energy levels. In most cases this approximation is a good one because the Zeeman interaction is significantly stronger than the other interactions (see Table 3.1). For systems with strong quadrupolar coupling constants, this approximation does break down and higher order effects must also be considered.

The Hamiltonian for the Zeeman interaction is given by,

$$\hat{\boldsymbol{H}}_z = -\hat{\boldsymbol{\mu}} \cdot \boldsymbol{B}_0, \tag{3.7}$$

where $\hat{\boldsymbol{\mu}}$ is the nuclear magnetic moment operator. The Hamiltonians for the rest of the nuclear interactions take on a similar form,

$$\hat{\boldsymbol{H}} = \hat{\boldsymbol{I}}_1 \cdot \boldsymbol{R} \cdot \hat{\boldsymbol{I}}_2, \tag{3.8}$$

containing terms representing the spin operator of the nuclear spin whose energy is modified, $\hat{\boldsymbol{I}}_1$, as well as the operator for the spin or other vector property (such as the external field) that is the source of the magnetic interaction, $\hat{\boldsymbol{I}}_2$, which is essentially modifying the effective magnetic field experienced by spin 1. $\boldsymbol{R}$ is the interaction tensor that relates the two vector quantities and contains the orientation dependence of the interaction. The form of these interaction tensors for the different types of coupling are given in the following sections.

3.2.1 The interaction tensor and reference frames

The interactions in NMR are between vector quantities. They are anisotropic and so tensor quantities are required to encode the full orientation dependence of the interac-

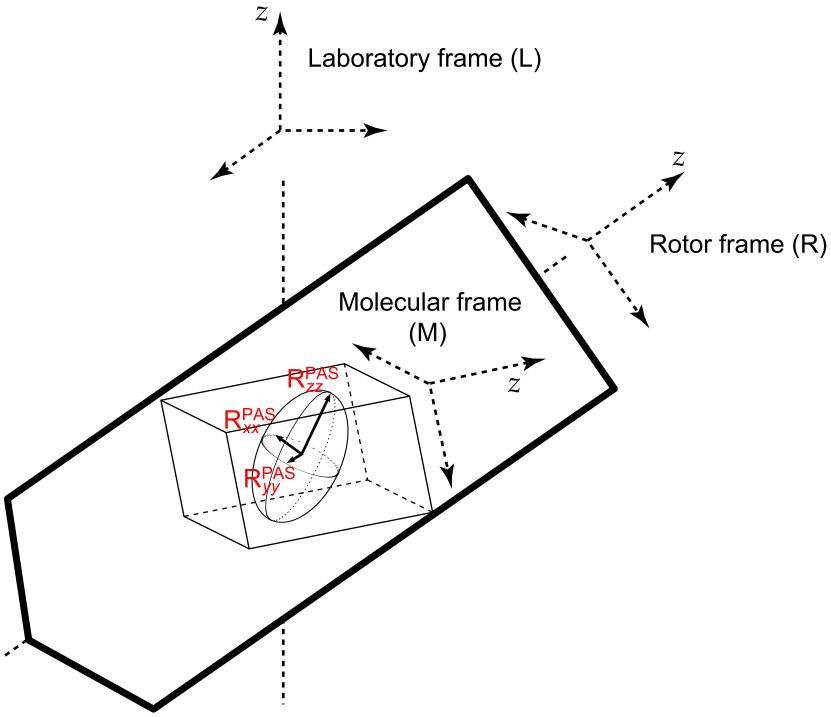

Figure 3.1: Illustration of the different reference frames in solid-state NMR. Modified, with permission, from ref. [43].

tion. $\boldsymbol{R}$ (from Equation 3.8) is a rank 2 tensor; a 3 x 3 matrix with 9 components:

$$\boldsymbol{R} = \begin{pmatrix} R_{xx} & R_{xy} & R_{xz} \\ R_{yx} & R_{yy} & R_{yz} \\ R_{zx} & R_{zy} & R_{zz} \end{pmatrix}. \tag{3.9}$$

The form that this tensor takes depends on reference frame from which the interaction is observed, however. The different reference frames commonly referred to in NMR are shown in Figure 3.1. The matrix representations in different frames are related to each other by rotations.

$\boldsymbol{R}$ can be rotated into a frame which represents the *principle axis system* (PAS) of the interaction. The PAS corresponds to the frame of the interaction itself, which in the case of, say, the dipolar coupling, has its z-axis aligned with the internuclear vector between the interacting dipoles. In the PAS, $\boldsymbol{R}$ is a diagonal matrix, and its *principle values* can be obtained by diagonalising the interaction tensor obtained in any other frame. By convention, the tensor is oriented so that the largest element is R_{zz}^{PAS}. The principle values of the interaction tensor in the PAS are often expressed as alternative

quantities,

$$R_{\text{iso}} = \frac{1}{3}(R_{xx}^{\text{PAS}} + R_{yy}^{\text{PAS}} + R_{zz}^{\text{PAS}}), \tag{3.10}$$

$$\Delta = R_{zz}^{\text{PAS}} - R_{\text{iso}}, \tag{3.11}$$

$$\eta = \frac{R_{xx}^{\text{PAS}} - R_{yy}^{\text{PAS}}}{R_{zz}^{\text{PAS}}}, \tag{3.12}$$

where R_{iso} is the isotropic value, Δ is the anisotropy and η is the asymmetry of the interaction. These quantities are physically significant and can directly affect the NMR spectrum. They can also be used to express the PAS interaction tensor using a different basis, in which the components can easily be grouped by their symmetry properties. For a general rank 2 tensor there are 8 such terms in this *spherical tensor* representation, although only the symmetric components are relevant in NMR. They are,

$$R_{0,0} = R_{\text{iso}} \tag{3.13}$$

$$R_{2,0} = \sqrt{\frac{3}{2}}\Delta \tag{3.14}$$

$$R_{2,\pm1} = 0 \tag{3.15}$$

$$R_{2,\pm2} = \frac{1}{2}\eta\Delta \tag{3.16}$$

where R_{iso}, Δ and η are composed of the principle values of the PAS in the Cartesian basis set as described by Equations 3.10–3.12. The first subscript describes what *rank* the term corresponds to, which reflects its symmetry under rotation, and the second, different components of this rank.

To determine how the relative orientations and motion of the PAS interaction tensor affects the NMR signal, it must be rotated into the lab frame (this is discussed further in Section 3.5.1). The spherical tensor representation of the PAS provides a convenient way of simplifying this rotation, as the only terms that survive the high-field approximation are the rank 2, $R_{2,0}$ term, and the rank 0, $R_{0,0}$ term, which is isotropic and invariant to rotation. Therefore, only the effect of the rotation on the $R_{2,0}$ element of the interaction tensor must be known.

The rotation through Euler angles (α, β, γ) is performed by the rank 2 *Wigner rotation matrix*, $D^{(2)}(\Omega(\alpha, \beta, \gamma))$, which acts on each of the rank 2 terms of the spherical

tensor,

$$R'_{2,m} = \sum_{n=-2}^{2} D^{(2)}_{mn}(\Omega) R_{2,n}. \tag{3.17}$$

The exact form of this rotation matrix is discussed elsewhere[43]. In practice, the rotation from the PAS to the lab frame is split into multiple rotations from the PAS up through the hierarchy of frames (see Figure 3.1) up to the lab frame.

3.2.2 Chemical shielding

Nuclei are surrounded by an electron density that depends on their local chemical environment. When an external field is applied to the system, it causes the electrons to circulate which in turn results in a local magnetic field, which opposes the direction of the externally applied field (according to Lenz's law). This local field acts to reduce the effective field experienced by the local nuclei; they are shielded from the external field. The full Hamiltonian for this interaction is,

$$\hat{\boldsymbol{H}}_{\mathrm{cs}} = -\hat{\boldsymbol{I}} \,.\, \sigma \,.\, \boldsymbol{B}_0, \tag{3.18}$$

where σ is the chemical shielding tensor, that contains information about the distribution of the electrons at the nucleus, which is generally not spherical. The principle axes of the shielding tensor (along which direction the tensor is diagonal) is centred at the nucleus, with its orientation within the molecule decided by the local electron density.

The shielding effect on the nuclear energy levels depends, to first order in perturbation theory, mainly on the σ_{zz} value of the lab-frame tensor, as it is this component that acts in the same direction as the external field. The interaction reduces the effect of the external field, so that instead of experiencing a field of strength B_0, the nucleus sees a reduced field of $(1 - \sigma_{zz})B_0$, modifying the energy of the different spin states to,

$$E = \hbar \gamma m_I B_0 (1 - \sigma_{zz}), \tag{3.19}$$

which has the effect of modifying the NMR transition frequency. However, the exact frequency depends on how the molecule is oriented with respect to the field, because

then the lab frame tensor is rotated and the value of σ_{zz} changes. The full expression, relating the value of σ_{zz} back to the PAS, is given by,

$$\sigma_{zz} = \sigma_{\text{iso}} + \frac{1}{3}\sum_{j}(3\cos^2\theta_j - 1)\sigma_{jj}, \tag{3.20}$$

where the sum over j is for the different components of the PAS interaction tensor and θ_j is the angle between that direction of the PAS and $\boldsymbol{B}_0$.

In solution-state NMR, rapid tumbling of the molecules, and hence rapid reorientation of the PAS, suppresses the second term in Equation 3.20 completely, and only the isotropic chemical shift, σ_{iso}, has an impact on the spectrum. In solids and powder samples all orientations of the PAS are present and, whilst the signal is still shifted by an amount proportional to σ_{iso}, the peak appears broadened because it is a superposition of many peaks, from spins that are each experiencing different effective field strengths because of the varying orientations of electron density surrounding them. The extent of the broadening depends on the anisotropy of the PAS tensor, termed the *chemical shift anisotropy* (CSA).

3.2.3 Dipolar coupling

Nuclear spins themselves are a source of a magnetic field and as such they can interact with each other through space. The full Hamiltonian for the dipolar interaction between two spins j and k is

$$\hat{\boldsymbol{H}}_{\text{dd}} = \hat{\boldsymbol{I}}_{\text{j}} \,.\, \boldsymbol{D} \,.\, \hat{\boldsymbol{I}}_{\text{k}}, \tag{3.21}$$

so the source of the interaction for nucleus j is the dipole corresponding to nucleus k, and $\boldsymbol{D}$ dipolar coupling tensor in the lab-frame. The corresponding modification to the nuclear spin energy levels (for the heteronuclear case) is,

$$E = \frac{1}{2}(3\cos^2\theta - 1)d_{\text{jk}}m_{\text{j}}m_{\text{k}}, \tag{3.22}$$

where θ is the angle between the zz component of the PAS and the external field, and d_{jk} is the dipolar coupling constant;

$$d_{\mathrm{jk}} = -\hbar \left(\frac{\mu_0}{4\pi}\right) \frac{\gamma_j \gamma_k}{r^3}, \tag{3.23}$$

which is also the value of D_{zz} in the PAS. The other two diagonal elements in this frame are equal, $D_{xx} = D_{yy} = -\frac{d_{\mathrm{jk}}}{2}$, and the interaction tensor is axially symmetric. The interaction tensor in the PAS is therefore traceless, meaning that the isotropic component of the dipolar coupling is zero, and so there is no evidence of dipolar coupling in the spectra of solutions. In solid spectra of spin half nuclei, the parallel and anti parallel arrangements of spins j and k contribute two overlapping powder patterns, forming a Pake Doublet with a splitting d_{jk} for a heteronuclear spin pair, and $\frac{3}{2}d_{\mathrm{jk}}$ for a homonuclear spins.

3.2.4 Quadrupolar coupling

For nuclei with spin quantum number, $I > 1/2$, the charge distribution within the nucleus is non-trivial, and is modeled as a quadrupole. The quadrupolar charge distribution interacts with the local electric field gradient (EFG), which in turn affects the nuclear spin energy levels and thus the NMR transition frequency. The full Hamiltonian is given by,

$$\hat{\boldsymbol{H}}_{\mathrm{Q}} = \frac{eQ}{6I(2I-1)\hbar} \boldsymbol{I} \cdot e\boldsymbol{q} \cdot \boldsymbol{I}, \tag{3.24}$$

so that the interaction is between the quadrupole moment of the nucleus, $\mathrm{e}Q$, and the local electric field gradient, which is expressed as the tensor $e\boldsymbol{q}$. This tensor is traceless as in the case of the dipolar coupling tensor and so similarly, there is no isotropic component and therefore no effect on solution-state spectra (although it does provide an extremely efficient method for the magnetisation to relax). The EFG at the nucleus is caused by the local electron density and depends on the symmetry at the nucleus.

The quadrupolar coupling affects each of the Zeeman-split nuclear energy levels by,

$$E = \left\{ \frac{3m_I^2 - I(I+1)}{8I(2I-1)} \right\} \left[(3\cos^2\theta - 1) + \eta \cos 2\phi \sin^2\theta \right] \chi, \tag{3.25}$$

where θ and ϕ are spherical polar angles that relate the orientation of the $e\boldsymbol{q}$ PAS to the external field, and χ and η are the *nuclear quadrupole coupling constant* and quadrupolar asymmetry respectively,

$$\chi = \frac{e^2 Q q_{ZZ}}{h}, \tag{3.26}$$

$$\eta = \frac{q_{YY} - q_{XX}}{q_{ZZ}}. \tag{3.27}$$

In quadrupolar systems, because $I > 1/2$, there are multiple transitions and the effect of the quadrupole coupling on the spin energy levels means that multiple peaks are observed in the NMR spectrum. However, the central transition for systems in which I is an odd multiple of $1/2$ are approximately unaffected by the quadrupolar coupling because the m_I^2 dependence in Equation 3.25, ensures that the $m_I = \pm 1/2$ levels are shifted by the same amount. Therefore, while the rest of the transitions in a powder sample are broadened considerably by the angular dependence, this central transition remains unshifted and narrow.

The quadrupolar coupling can be very strong (100s MHz), and can approach the energies associated with the Zeeman effect. In this regime perturbation theory begins to break down and higher order effects also have to be taken into account.

3.2.5 Scalar coupling

The scalar, or J-coupling is a result of through-bond interactions that communicate the relative states of neighbouring nuclear spins. The Hamiltonian is given by,

$$\hat{\boldsymbol{H}}_{\mathrm{J}} = \hat{\boldsymbol{I}}_{\mathrm{j}} \,.\, \boldsymbol{J} \,.\, \hat{\boldsymbol{I}}_{\mathrm{k}}, \tag{3.28}$$

where $\boldsymbol{J}$ is the J-coupling interaction tensor. The modification to the Zeeman energy levels is,

$$E = m_{\mathrm{j}} m_{\mathrm{k}} \left\{ J_{\mathrm{iso}} + \frac{1}{2}(3\cos^2\theta - 1)\Delta J \right\} h, \tag{3.29}$$

where J_{iso} and ΔJ are the isotropic and anisotropic components of the J-coupling tensor, respectively.

The strength of the J-coupling is only very weak, tens of Hz, making it difficult

to measure in solid state spectra because the other interactions dominate. However, the non-zero isotropic term means that the interaction is present in solution state spectra and a slight splitting is observed that can be used to give information about the local environment of the spins. Together with the isotropic shift, the J-coupling in solution-state NMR is what makes the method invaluable in structure determination.

3.3 Magic angle spinning (MAS)

The anisotropic terms in each of the interactions detailed above can give information about the local environment of a nucleus, but they also complicate spectra significantly by broadening lines and making it difficult to resolve overlapping signals. This is not a problem in the solution state because the stronger coupling interactions that cause significant broadening are averaged to zero by the fast molecular tumbling. This effect is due to the dependence of the splitting in the energy levels on $\frac{1}{2}(3\cos^2\theta - 1)$, which is the second order Legendre polynomial, $P_2(\cos\theta)$. In solution, the molecules reorient quickly on the timescale of the NMR experiment (molecules in a typical solution tumble isotropically at a rate of $\sim 10^{10}$ Hz depending on the size of the molecules) and the PAS frame of the interactions rotates isotropically so that the observed quantity is the average value taken over many orientations, which is zero when the tumbling is fast enough,

$$\int_0^\pi d\theta \sin\theta P_2(\cos\theta) = 0, \tag{3.30}$$

where the $\sin\theta d\theta$ term is the volume element for this coordinate system. The $P_2(\cos\theta)$ terms in Equations 3.20, 3.22, 3.25 and 3.29 all average to zero, suppressing the dipolar and quadrupolar terms completely, and leaving only isotropic effects from the J-coupling and chemical shift.

The effect of motional narrowing can also be reproduced to some extent for powder samples in the solid state by mechanical rotation of the sample. When a sample is spun at an angle θ_R with respect to $\boldsymbol{B}_0$, the angle of the PAS with respect to the field is modulated,

$$\langle 3\cos^2\theta - 1\rangle = \frac{1}{2}(3\cos^2\theta_\mathrm{R} - 1)(3\cos^2\beta - 1), \tag{3.31}$$

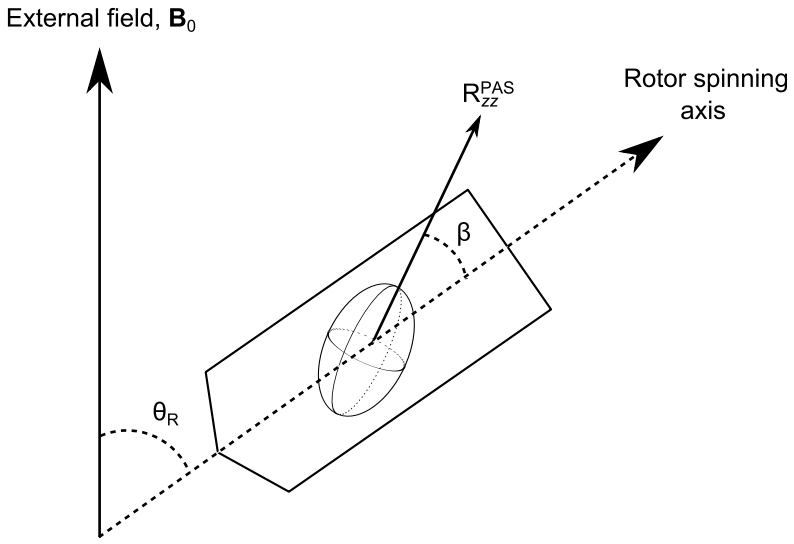

Figure 3.2: Schematic of the magic angle spinning experiment, illustrating the angles β and θ_{R}, reproduced from ref. [44].

where β is the angle between the principal z-axis of the interaction tensor and the rotor axis, as shown in Figure 3.2. In the special case where $\theta_R = 54.74°$, called the magic angle, the first term on the right hand side becomes zero, driving the time average of $P_2(\cos\theta)$ to zero. This has the effect of suppressing the anisotropic terms that depend on $P_2(\cos\theta)$. However, to suppress the terms completely the rate of spinning must be fast compared to the strength of the interaction. With current spinning rates reaching up to approximately 70 kHz, it is possible to suppress most dipolar coupling interactions and the chemical shift anisotropy, but not quadrupole couplings. When the broadening is not completely suppressed, a series of *spinning sidebands* are observed in the frequency spectrum, and rather than a single set of sharp peaks, a series observed, set away from the centreband (which remains at the isotropic frequency) at multiples of the spinning frequency. The intensity pattern of these peaks matches that of the underlying static spectrum and so the sidebands can still be used to fit to the underlying anisotropic behaviour (if enough are present), and can still allow overlapping peaks to be resolved.

3.4 The vector model

The vector model is used to provide a simplified model of the interaction of the RF pulses which are used to excite the nuclear spins in NMR and to manipulate the magnetisation in more complicated experiments. Rather than investigate individual spins in the system, the behaviour of the bulk magnetisation vector, $\boldsymbol{M}$, is considered. When an external field is applied, the equilibrium magnetisation vector points along the direction of the field, adopting the same direction as $\boldsymbol{B}_0$ (which points along the lab-frame z-axis) and has its maximum length, M_0. Under the influence of the field, $\boldsymbol{M}$ precesses around $\boldsymbol{B}_0$ at the Larmor frequency for the observed nucleus. When an RF pulse of frequency ν_{RF} is applied it results in a magnetic field that rotates the precessing bulk magnetisation vector away from its equilibrium position along $\boldsymbol{B}_0$. The exact behaviour of $\boldsymbol{M}$ due to the effects of both fields acting together is complicated. However, the picture can be simplified significantly by observing it from a frame that rotates about $\boldsymbol{B}_0$ at the frequency of the RF, ν_{RF}.

In the rotating frame, if the pulse applied is on resonance, i.e. $\nu_{\mathrm{RF}} = \nu_0$, then the bulk magnetisation is static (off resonance, and it nutates at a frequency of $\nu_{\mathrm{RF}} - \nu_0$), and the magnetisation vector is affected only by the field due to the RF, $\boldsymbol{B}_1$, and it nutates around the axis that the RF is applied along at a frequency of $\omega_1 = 2\pi\nu_1 = \gamma B_1$. To distinguish pulses that act along different directions, an arbitrary axis system is defined, with x- and y-axes orthogonal to each other and to the z-axis which coincides with the external field, $\boldsymbol{B}_0$. An RF pulse is defined as having a *phase* that labels which axis it acts along, and is also labeled according to the total angle it rotates the bulk magnetisation by. By convention, the direction of the rotation is anticlockwise, and so a pulse acting along the x-axis tilts the bulk magnetisation down through the $-y$ direction, onto $-z$, eventually completing the full 360° rotation and arriving back at $+z$. Such a pulse is labeled 360_x (or $2\pi_x$). With this simplified model, it is easy to predict what effect the RF pules have in complicated NMR experiments, and it is also used to in Chapter 5 to illustrate the interaction schemes in the pulse sequences used.

3.5 Investigating motion with solid-state NMR

Although solids are usually thought of as being rigid, this is never completely true and often there are components of solid systems that can be very mobile. Long-range techniques that are commonly used to investigate solids, such as X-ray diffraction, can often be uninformative in these regimes, where molecular dynamics serves to introduce disorder in the long range structure of the compound. However, NMR is well suited to study dynamics in the solid state, because it probes the local environment and properties of each state present. It is extremely sensitive to motion on a wide range of timescales, from seconds to nanoseconds. Two methods by which dynamic processes can be probed by NMR are discussed here: the effect of dynamic averaging on anisotropic interactions, and the impact of dynamics on relaxation rates.

3.5.1 Effects of motional averaging

Although the anisotropy of the chemical shift and the dipolar and quadrupolar couplings can significantly complicate solid-state NMR spectra and make it difficult to extract structural characteristics in the same way as has made solution-state NMR indispensable to chemists, they can provide rich information about molecular dynamics in the sample. In particular, each of these interactions is sensitive to motion that occurs on a similar rate to the size of the interaction itself: for the chemical shifts and dipolar couplings this is of the order of kHz, and for quadrupole couplings, rates that are a lot faster: of the order of MHz.

In a powder sample each different spin orientation contributes a sharp resonance peak, with the sum of all of these individual lines contributing to the overall powder pattern. When there is motion and it changes the orientation of the spin with respect to the field, it interchanges different spin environments and thus resonance frequencies. When the motion is fast enough - of the order of the difference in exchanged resonance frequencies, only the average frequency is observed. The effect is that the overall powder lineshape is also averaged. The exact nature of the averaging depends on the rate of the motion, k, and its reorientational behaviour.

The effect of the rate can be split into three different regimes depending on whether

it is much faster than the frequency of the interaction, $k \gg \omega$, of approximately the same order, $k \approx \omega$, or much slower than it, $k \ll \omega$. When the rate is much slower, there is no motional narrowing in the spectrum, although there can be some line broadening at intermediate rates. In the regime where $k \approx \omega$, fits can be used to extract both the rate and orientation dependence of the motion. In the limit of fast motion, where $k \gg \omega$, changes in the motional rate do not produce any further line narrowing, and the interaction tensor takes a value that is simply the weighted average of the values it assumes for all the different sites it moves between. If the motion is isotropic, as in the case of liquids, the mean value is zero and the anisotropic terms disappear. However, for fast, anisotropic motion, the anisotropic components survive, and the lineshape can still be analysed to give information on the orientational changes resulting from the motion.

The orientational dependence is encoded in the time-averaged Wigner rotation matrix that relates the exchanging positions of the PAS with the crystal frame and ultimately to the lab frame(see Equation 3.17). The dependence on the rate of the motional process compared to the size of the anisotropic interaction is included in calculations of the evolution of the magnetisation, which is discussed more fully in ref. [45]. These calculations can be used, together with a model for the orientational motion (which would normally be a simplified model in terms of jumps between distinct PAS orientations), to predict the expected powder pattern. The predicted powder patterns can then be compared and fitted to empirical measurements to give information about both the rate and the orientational behaviour of the motion. This method is used extensively for looking at the effects of motion on the CSA and dipolar coupling because the lineshapes can be accurately measured. This is not so for lineshapes from quadrupole couplings, where the spectra are so broad that it can be difficult to record them accurately enough for the fitting process. The exception is deuterium, which is a quadrupolar spin-1 nucleus, but with a relatively low quadrupole coupling strength of 140–220 kHz.

Liquid crystal systems provide a special case in which there is fast anisotropic motion. In a simple, uniaxial nematic liquid crystal, the molecules are, on average, oriented so that their long axes are parallel with each other, along a direction defined

as the *director*, $\hat{\boldsymbol{n}}$. The liquid crystal molecules are still free to rotate, however, and do so on a fast timescale about an axis that is, on average, parallel to the director. Typical interactions that could be observed in NMR are heteronuclear dipolar couplings between bonded C-H atoms in the liquid crystal molecules. In this case, the direction of the PAS of the interaction tensor is directed with its z-axis parallel to the bond and if the molecule is approximated to be rigid then the PAS is also fixed with respect to the molecular frame.

In this highly symmetric case, rather than reverting to the more general case of the irreducible spherical tensor form of the interaction and using Wigner rotation matrices to relate the different frames, the scaling of the interaction can be expressed as a function of the angles, θ_{xn},θ_{yn},θ_{zn} between the director, $\hat{\boldsymbol{n}}$, and the components of the PAS, which is fixed within the molecule frame. The Wigner rotation matrices can be substituted by the *Saupe order parameters*[46];

$$S_{\alpha\beta} = \langle \frac{1}{2}(3\cos\theta_{\alpha n}\cos\theta_{\beta n} - \delta_{\alpha\beta})\rangle, \tag{3.32}$$

where the α and β subscripts refer to the x, y, z components of the interaction tensor and $\delta = 1$ if $\alpha = \beta$ and zero otherwise. The transformations of the elements of the coupling tensor, $\boldsymbol{R}$, from the molecular frame to the director frame are then given by,

$$R^{d}_{\alpha\beta} = S_{\alpha\beta}R^{mol}_{\alpha\beta}, \tag{3.33}$$

and the full transformation to the lab frame (L) is,

$$R^{L}_{\alpha\beta} = \frac{1}{2}(3\cos^2\beta_{dL} - 1)S_{\alpha\beta}R^{mol}_{\alpha\beta}, \tag{3.34}$$

where β_{dL} is the angle between the director and the external magnetic field (often in liquid crystal systems, the molecules align with the field, meaning that $\beta_{dL} = 0$).

This shows that measurements of the strengths of anisotropic NMR interactions can lead to a direct measurement of the $S_{\alpha\beta}$ order parameters, which in turn give information about the orientation of the liquid crystal molecules with respect to the director. This is an interesting example of a system in which NMR measurements can

be directly related to molecular information. These liquid crystal systems also have strong parallels with the solid inclusion compounds discussed in Chapter 4, where the confinement of mobile molecules in one dimensional tunnels restricts their motion to rotational diffusional about one axis.

3.5.2 Relaxation

At thermal equilibrium the bulk magnetisation vector points along the laboratory z-axis. RF pulses perturb the system away from this equilibrium state, but in time the system relaxes back to it. There are two types of relaxation: spin-lattice relaxation, in which the magnetisation is exchanged with the surrounding 'lattice' of a given spin (and so is lost from the spin system), and spin-spin relaxation, in which *dephasing* of the magnetisation occurs between different spins. In the vector model, longitudinal spin-lattice relaxation accounts for the recovery of the z-component of the bulk magnetisation (with time constant T_1), while spin-spin relaxation is the mechanism for the dephasing of the magnetisation in the xy plane (with time constant T_2). The recovery of the transverse magnetisation to equilibrium due to spin-lattice relaxation (which is much slower than spin-spin relaxation in the solid state) can also be measured. It is called spin-lattice relaxation in the rotating frame, because it requires a lock pulse to restrict the T_2 dephasing, and has a time constant, $T_{1\rho}$.

Relaxation is caused by fluctuations in the local magnetic field experienced by a given nuclear spin. The fluctuations are a consequence of molecular motion which causes the spin interactions to be modulated and time dependent. The dipolar and quadrupolar coupling and the chemical shift anisotropy are the main mechanisms by which the magnetisation relaxes.

The motion of the spins (or the magnetic interactions) is characterised by the *autocorrelation function* (cf. MD),

$$C(t) = \langle \boldsymbol{a}(0) \cdot \boldsymbol{a}(t) \rangle, \tag{3.35}$$

where $\boldsymbol{a}$ is the orientation vector of a given interaction, and the angled brackets represent an ensemble average. The vectors are normalised so that the quantity *C(t)* is

restricted to take values between 0 and 1. This is a sort of memory function, that describes how quickly the vector $\boldsymbol{a}$ loses the information about its initial orientation. In general, for simple processes like isotropic motion or a symmetric two site jump, $C(t)$ takes the form of an exponential decay,

$$C(t) = \exp(-\frac{t}{\tau_c}), \tag{3.36}$$

with a characteristic time constant, τ_c, that is indicative of the underlying process.

The influence that a given motional process has on a particular relaxation mechanism is governed by the spectral density, $J(\nu)$, which is a function of the frequency that the relaxation occurs on, ν, as well as the time constant of the motion. $J(\nu)$ can be derived directly as the Fourier transform of the relevant time correlation function,

$$J(\nu) = \int_{-\infty}^{\infty} C(t) \exp(-i2\pi\nu t) dt. \tag{3.37}$$

This function takes a maximum value when the $2\pi\nu\tau_c = 1$, that is, when the rate of the motion matches the angular frequency of the relaxation mechanism. It is at this value that the relaxation is driven most efficiently.

For a process that can be described using a single correlation time, $J(\nu)$ can be written more simply as,

$$J(\nu) = \frac{\tau_c}{1 + (2\pi\nu\tau_c)^2}. \tag{3.38}$$

The expression for the rate of a particular relaxation rate will contain linear combinations of spectral densities, with the exact form depending on the interaction which is the source of the relaxation mechanism. In the case of a spin half system whose relaxation is driven by homonuclear dipolar coupling the rates of relaxation for T_1 and $T_{1\rho}$ can be obtained explicitly as,

$$R(T_1) = \frac{1}{T_1} = K[J(\nu_0) + 4J(2\nu_0)], \tag{3.39}$$

$$R(T_{1\rho}) = \frac{1}{T_{1\rho}} = K[\frac{3}{2}J(\nu_{\mathrm{RF}}) + \frac{5}{2}J(\nu_0) + J(2\nu_0)] \approx \frac{3}{2}K[J(\nu_{\mathrm{RF}})], \tag{3.40}$$

where v_0 is the Larmor frequency of the nucleus, ν_{RF} is the RF nutation frequency

used to lock the magnetisation for the measurement of $T_{1\rho}$, and K is a constant that depends on the strength of the dipolar coupling. The spectral densities that depend on the Larmor frequency are neglected in Equation 3.40 because in the regime where the molecular motion strongly interferes with $T_{1\rho}$ (rates of the order of tens of kHz), the contributions from $J(\nu_0)$ (timescale of hundreds of MHz) are minimal.

The relaxation time constants can be measured by relatively simple NMR experiments, some of which are described in Chapter 5. However, there are many free parameters in the models that cannot all be fit to a single value of the time constant. To obtain detailed information about the underlying molecular processes a range of $J(\nu)$ values must be sampled. This can be done by simply changing the temperature under which the experiment is done, which causes variation in the rate of the molecular process and hence the value of τ_c. In relaxometry the field strength can also be varied, allowing the functional form of $J(\nu)$ to be fully explored without changing the temperature, avoiding any temperature-induced changes in the sample. However, it is difficult to achieve variable magnetic fields that are of a similar strength to those used in modern NMR equipment.

Chapter 4

Structural properties of carboxylic acid dimers confined within the urea tunnel structure

4.1 Introduction

Urea inclusion compounds (UICs) are a family of self assembling crystalline organic solids [47–52]. They are composed of an extended lattice of hydrogen bonded urea molecules that form hexagonal, parallel tunnels along one crystal direction (see Figure 4.1) [53, 54]. In the ambient temperature phase, the tunnels are helical, and can be either right handed (in the $P6_122$ space group) or left handed (in the $P6_522$ space group), although all of the tunnels in a given single crystal will adopt the same chirality. In contrast to some other solid inclusion compounds, such as zeolites, the structure is only stable if the tunnels contain a dense packing of guest molecules. However, the narrow diameter of the tunnels (between *ca.* 5.5 Å and 5.8 Å along their length [55]) is only sufficient to accommodate *n*-alkane chains and their close derivatives, leading to an application of the materials as molecular sieves that could also possibly be enantiomerically selective due to the inherent chirality of the tunnels [56, 57]. A considerable amount of work has been done to try and understand the behaviour and interactions of both the host and guest molecules in these systems.

While single crystal X-ray diffraction measurements can give insight into the struc-

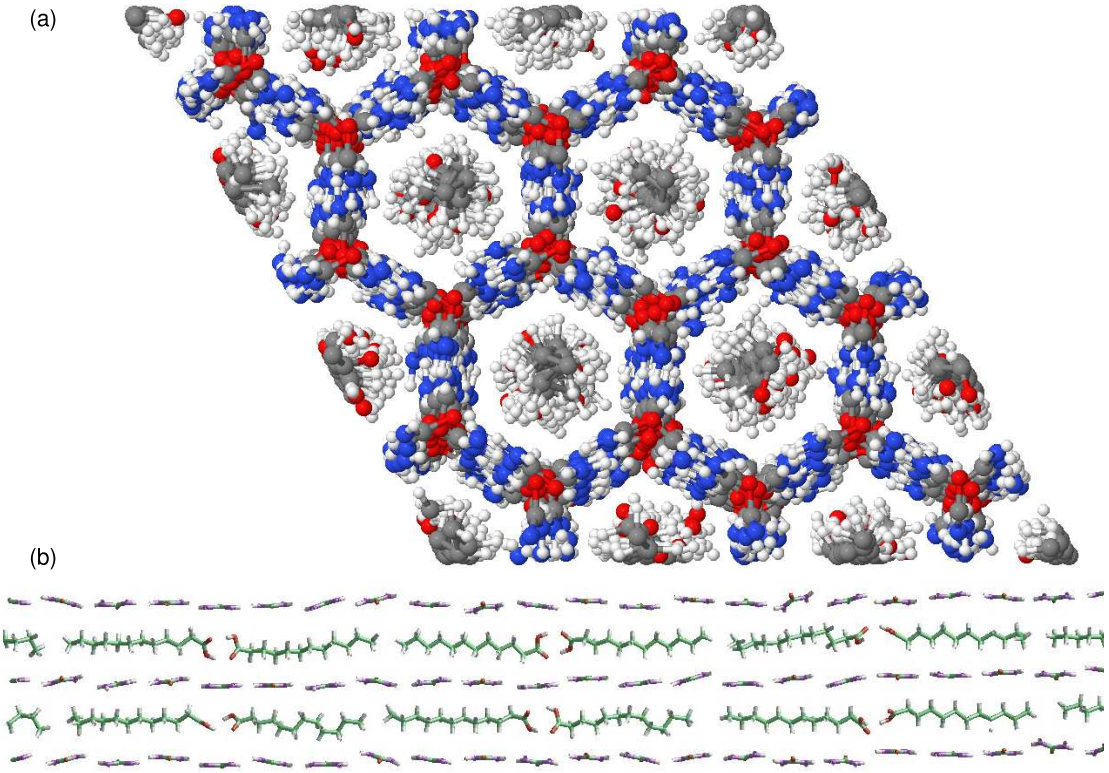

Figure 4.1: Snapshots of the structure in the MD simulation of dodecanoic acid/urea. (a) Viewed along the z-axis of the simulation cell with the periodic boundary conditions in the x and y dimensions apparent. (b) Viewed perpendicular to the tunnel axis after an arbitrary number of timesteps, showing only a single plane of molecules across two tunnels.

ture of the urea host lattice, showing that most UICs have the same structure at ambient temperature [53], the guest molecules are highly dynamic and cannot be resolved directly. However, scattering from X-rays incident perpendicular to the tunnel direction can give information about the *relative* positions of the guests, specifically their periodicity along the tunnels, c_{g}, and the average distances between the centres of mass of molecules in neighbouring tunnels, Δ_{g} [54, 58]. The guest periodicity has been found for a wide variety of guest molecules [59], often with the aim of ascertaining whether the packing is commensurate with the periodicity of the host structure, c_{h}. This relationship is said to be commensurate if there are sufficiently small integers m and n that satisfy the relationship, $mc_{\mathrm{g}} = nc_{\mathrm{h}}$. In this regard, the trends in the behaviour of different families of guest molecules have been explored [59, 60].

A variety of different experimental techniques have been employed in an attempt to characterise the behaviour of the guest molecules, including solid-state NMR [61–71], EPR [72, 73], neutron scattering [74], and IR [67, 71, 75] and Raman spectroscopy [67, 71, 75, 76]. The most widely discussed properties have been the internal conformations of the guest molecules and their orientation and rotational behaviour relative to the urea tunnels (at ambient temperature; at low temperatures the motion of the guest molecules is frozen out and the structure undergoes a phase transition, which has also been studied extensively elsewhere [66, 77–82], but is outside the scope of this work). Each of these experimental methods infer the presence of dynamics and disorder in the guest molecules, but both the quantitative and qualitative descriptions of the underlying molecular behaviour can vary quite significantly. For instance, the estimation of the number of defects in the guest chain backbone dihedral angles remained controversial for some time, with estimates for the fraction of gauche defects ranging from none at all [71] (an all-trans configuration of the guest molecules was the accepted view for some time) to up to about 25 % [63], depending on the precise guest molecule studied. The problem is that the experiments require models to link their results back to the underlying molecular behaviour, but those models do not account for the high degree of correlation between the different degrees of freedom of the molecules, and they often reduce the complication to a level that neglects key interactions. Fundamentally, the motion is too complicated and the information content of the experiments is too low.

MD simulation permits the system to be built from the atoms up, and for experimental data to be calculated from the underlying atomic and molecular behaviour. There have been numerous atomistic MD studies of UICs used to try and understand the underlying motion of the guest molecules, for systems containing various guest molecules: alkanes [62, 74, 83–85], carboxylic acids [62, 86], and other types of guest [57, 86, 87]. With the exception of the studies of nonadecane/urea by Souaille et al. [74, 83, 84], all the MD simulations reported previously were subject to limitations imposed by one or more of the following: a rigid urea tunnel structure, a single tunnel of the host structure, or a single guest molecule within the tunnel. All of these restrictions impact on the guest behaviour, as is shown in this work, and also by Souaille et al. [83], who compared several simulations each limited by a different one of the factors mentioned above. They were able to show that fixing the urea positions or varying c_g/c_h from the value observed experimentally results in simulations that poorly reproduce IQNS (incoherent, quasi-elastic neutron scattering) structure factors, and hence do not reproduce the correct diffusional and rotational behaviour of the guests.

The two previous MD simulation studies for urea inclusion compounds containing alkanoic acid guests [62, 86] were both subject to the limitation of a fixed urea tunnel structure. The simulation in one case [86] probed only a single tunnel containing just one hydrogen-bonded alkanoic acid dimer as the guest. In the other case [62], although the simulation cell comprised nine tunnels, the host/guest ratio employed ($c_g/c_h = 4$ for dodecanoic acid guests) differs significantly from the value obtained from the X-ray diffraction studies reported here. This fact may account for the discrepancy observed in ref. [62] between the simulation results and experiment.

Here, results from a new MD simulation of dodecanoic acid/UIC are presented. Great care has been taken to set up the simulation as accurately as possible, firstly by using a ratio of the host and guest periodicities that matches the (incommensurate) ratio determined experimentally within an accuracy of better than 0.4 %. Secondly, elements of the force field have been fitted to *ab initio* energy profiles to ensure it faithfully reproduces the molecular interactions. A fully flexible host structure was also used, containing nine tunnels with periodic boundary conditions in each dimension. The simulations reveal many subtle aspects of the molecular behaviour and the

consequences of the guest molecules' confinement that, in many cases, are not accessible experimentally. Order parameters were also calculated directly from the simulation trajectories and could be compared to experimental results from the literature.

4.2 MD simulation

MD simulations were performed on the urea inclusion compound containing dodecanoic acid (DDA) guest molecules. As a consequence of the incommensurate relationship between the host and guest substructures in these materials, the size of the simulation cell (specifically, the length of the host tunnel in particular) requires careful consideration in order to ensure that the ratio of the host and guest periodicities along the tunnel direction is a sufficiently close approximation to its experimental value. To explore in more detail how this ratio affects the results, three further MD simulations were also carried out for DDA/urea using different values of the average periodic repeat distance of the guest molecules (see Table 4.1). To compare the behaviours of different guest molecules, a simulation of UIC with dodecane (DD) guest molecules was also analysed. The DD/urea simulation was set up and run by Dr. Sebastian Palucha.

The urea tunnel structure was taken from the crystal structure reported previously [54], corresponding to the $P6_122$ form of the tunnel. In the main simulation carried out for DDA/urea (top row of Table 4.1), the hexagonal simulation cell comprised 171 unit cells of the host structure (1026 urea molecules) representing nine tunnels. Along the tunnel direction, the simulation cell comprised 19 unit cell repeats of the urea host structure and six pairs of DDA guest molecules. Thus, the ratio c_g/c_h implicit in the simulation was $19/6 = 3.17$. For comparison, the repeat distance estimated from single-crystal X-ray diffraction data at ambient temperature is 35.0 ± 0.2 Å[1], giving a ratio of $c_g/c_h = (35.0\text{ Å})/(11.01\text{ Å}) = 3.18$. The 12 molecules of DDA were placed in the tunnels as six hydrogen-bonded dimers in a head-to-head/tail-to-tail arrangement, with the carboxylic acid head-groups adjacent to each other to allow the formation of hydrogen-bonded dimers. Both EPR [72] and solid-state NMR [67] measurements have been used in the literature to show that only the head-to-head/tail-to-tail arrangement

[1] XRD measurements provided by Andrei Batsanov

Guest type	No. of tunnels	Total no. of urea molecules	No. of host unit cells along tunnel	Total no. of guest molecules	No. of guest molecules per tunnel	c_g/c_h	Total simulation time / ns
DDA	9	1026	19	108	12	3.17	20
DDA	9	1404	26	144	16	3.25	5
DDA	9	1458	27	144	16	3.38	5
DDA	9	1512	28	144	16	3.50	5
DD	9	432	8	45	5	1.60	10

Table 4.1: Details of the MD simulations.

is observed for alkanoic acid/urea inclusion compounds; no signals due to head-to-tail arrangements were detected within the observability limit of $< 1\%$ for ^{13}C solid-state NMR, in contrast to the random arrangement of, for example, fluoroalkane guests observed elsewhere by NMR [88]. Three further MD simulations were carried out for DDA/urea employing different values of the periodic repeat distance of the guest molecules, and were run for a shorter time than the main simulation. Details are given in Table 4.1.

For the MD simulation of DD/urea (Table 4.1), the simulation cell comprised nine tunnels, with eight unit cell repeats (c_h) of the urea host structure and five DD guest molecules per tunnel, corresponding to an average ratio $c_g/c_h = 8/5 = 1.6$. The corresponding experimental value for DD/urea at ambient temperature [89] is c_g/c_h = (17.6 Å)/(11.01 Å) = 1.60.

The MD simulations were carried out using the DLPOLY code [90] and the OPLS all-atom force field [32]. However, it was found that the force field parameters were not recreating the correct dihedral angle distributions in the carboxylic acid head group. The parameters were therefore fitted to the *ab initio* energy profiles of the dihedral angles spanning the carboxyl group and the full acid head group (C10-C11-C12-OC and OC-C12-OH-HO respectively, following the label scheme in Figure 4.2(a)). The *ab initio* profiles were constructed using an angle scan over the respective dihedral angles using Gaussian 03 [91] with the B3LYP functional [92] and 6-311g** basis set [93]. The torsional energy profiles were also calculated from the MD force field using an identical angle scan, and the least squares difference compared to the *ab initio* profiles were used to tune the dihedral angle force field parameters. It was found that to recreate all of

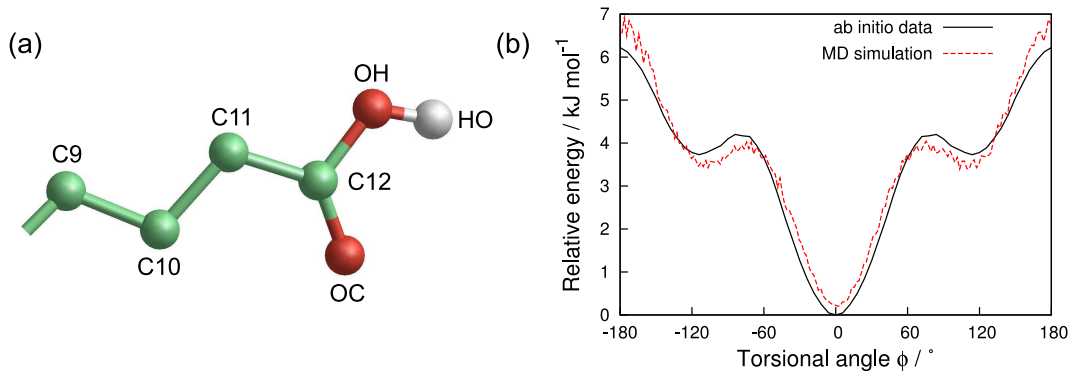

Figure 4.2: (a) The atom labeling scheme for the carboxylic acid group. Alkyl hydrogens are left out for clarity. (b) Comparison between the Gaussian *ab initio* energy profile of the carboxyl dihedral angle (C10-C11-C12-OC) and that obtained from Boltzmann inverting the relative populations during a 200 ns MD simulation at 300 K.

the energy distributions accurately, an improper dihedral angle had to be introduced across atoms C11, C12, OC and OH, restricting their out of plane motion. The final parameter set that were used is given in Appendix A. An MD run using DLPOLY was also undertaken on a single molecule using the final parameters to ensure that the energy profiles matched. The results are shown in Figure 4.2(b). Although the energy profile is not an exact match to that from the *ab initio* calculation, the important barriers for the jumps into and out of the gauche positions are accurately reproduced.

For each MD simulation, an initial equilibration period of 1 ns was followed by full production runs as specified in Table 4.1. The time-step in each case was 2 fs and the simulations were run at $T = 300$ K with a fully flexible urea structure. Volume fluctuations over the course of each simulation were found to be less than 1.5 %. The Nosé-Hoover algorithm [28] was used to run at constant pressure and a temperature of 300 K, with a 1 ps relaxation time.

The Ewald sum method was used to calculate the electrostatic interactions. The α and k values were tuned to ensure that the total electrostatic energy of the system and its contribution to the virial were equal but opposite in sign, and hence that the Ewald sum was converging and optimised for the system. A 7.5 nm cutoff was used for the long range interactions as its length is limited to being just less than half the shortest cell dimension. It should be noted that the 'charged group' scheme used by DLPOLY for calculating electrostatic interactions means that all of the atoms in a neighbouring

neutrally charged molecule are included in the electrostatic force calculation if any of its atoms fall within the cutoff distance. This leads to a much longer effective cutoff distance in the system, especially between guest molecules in adjacent tunnels.

In order to assess the effects of confinement within the urea tunnel structure on the structural properties of the carboxylic acid dimer, a separate MD simulation was also run for a system comprising one double-hydrogen-bonded dimer of DDA in an argon gas. The DDA dimer used as the starting configuration for this simulation was selected at random from the MD simulation for DDA/urea after equilibration, and the simulation was run until dissociation of the dimer (after approximately 5 ns).

4.3 Results

The confinement of the guest molecules acts to introduce a strong correlation between the different degrees of freedom of both the host and guest molecules. The intra- and inter-molecular interactions are coupled, with contributing effects from the molecular conformations of the guests and their interactions with their neighbours in the same and adjacent tunnels, as well the underpinning effect of the host structure which also displays restricted dynamic behaviour. To completely describe the system, each different aspect of the system is investigated and its influence on the overall structure and dynamics of both the host and guest molecules evaluated.

4.3.1 Guest dynamics

As known from previous MD simulations [83, 85] and experimental studies [49, 68, 72, 75, 83, 94–98], the guest molecules in conventional urea inclusion compounds are highly dynamic at ambient temperature, undergoing rapid reorientation about the tunnel axis and restricted translation along the tunnel. Here, diffusion coefficients were calculated from the MD simulations using the Einstein relation for diffusion in one dimension [99],

$$2tD =< |\boldsymbol{r}_i(t) - \boldsymbol{r}_i(0)|^2 >, \tag{4.1}$$

where $\boldsymbol{r}_i(t)$ was taken as the position vector of the centre of mass of molecule i (or dimer, in the case of the DDA) at time t. Ensemble averages were taken over all of the molecules in the simulation (accounting for the periodic boundary conditions) and from multiple time origins.

The results indicate that the motion is faster in the case of DD guest molecules, with diffusion coefficients along the tunnels (at 300 K) of 0.091 ± 0.031 Å^2 ps^{-1} for DD/urea compared to 0.0063 ± 0.0013 Å^2 ps^{-1} for DDA/urea. These values compare well with experimental measurements on alkane/urea inclusion compounds from IQNS [83] and NMR [64]. The order of magnitude difference between the diffusion coefficients for the guest molecules in DDA/urea and DD/urea is noteworthy, and is much greater than the variation due to different chain lengths of the guest molecules [64]. As discussed further in the following sections, the nature of the functional groups on the guest molecules clearly has a significant influence on the dynamics of the guest, as the potential energy landscape relating to translational and reorientational motions of the guest molecules is altered by their presence. This arises because of changes in the nature of the host-guest and guest-guest interactions, with both steric and electrostatic components playing important roles.

The experimental studies mentioned above also obtained estimates of the rotational diffusion rates of the guest molecules. The significance of this quantity is highly questionable however, because the guest molecules are not rigid, but show a highly dynamic conformational disorder.

4.3.2 Structural characteristics of confined alkyl chains

The intra-molecular structural properties of the guest molecules, and the structural relationships between the two molecules in the hydrogen-bonded DDA dimers, are now considered. The conformational properties of the alkyl chains may be summarised in terms of the local trans/gauche conformations of the dihedral angles along the chain. Figure 4.3(a) shows the relative populations of these conformations as a function of position within the alkyl chain. For both DD/urea and DDA/urea, the MD simulations confirm that the alkyl chains exist predominantly in the all-trans conformation, as has also been established experimentally (by Raman spectroscopy [69, 76] and NMR

[62, 67, 69]), and observed in previous simulation work [55, 83].

The simulation results here show that the distribution of torsion angles exhibits a slight 'zig-zag' fluctuation on moving along the chain (Figure 4.3(a)), with adjacent torsion angles alternating in their preference for the trans conformation. This pattern signifies that the conformations of different sites along the alkyl chains of the guest molecules become correlated as a result of their confinement. The fact that this behaviour is much more pronounced for DDA guest molecules, which have a larger cross-sectional area than the alkane molecules because of their bulky acid groups, would suggest that the correlation is a mechanism by which the guest molecules adapt in order to be accommodated within the tunnels and minimise their interactions with the host structure. Previous work has assumed that the all-trans configuration corresponds to the minimum energy configuration, but it could be the case that the introduction of defects near the chain ends makes the 'zig-zag' behaviour observed here lower in energy. Only guest molecules with an even chain length were investigated here, but it would be interesting to compare these results with those from a UIC system with odd chain length guests, as the 'zig-zag' behaviour would necessarily be disrupted.

It is also interesting to consider the effect of changing the periodic repeat distance of the guest molecules, as shown by the additional MD simulations carried out for different values of the ratio c_g/c_h for DDA/urea (Table 4.1). Figure 4.3(b) shows that the value of c_g/c_h has a significant effect on the conformation of the guest molecules. In particular, as c_g/c_h decreases, corresponding to a denser packing of guest molecules within the tunnel, a greater proportion of defects is introduced in the backbone torsion angles. The resultant molecular conformation is less straight than the all-trans conformation, and the overall length taken up by each guest molecule along the tunnel direction is decreased. Around the value of $c_g/c_h = 3.18$ that was observed experimentally for DDA/urea, the conformation of the DDA molecules is very sensitive to small changes in packing density.

In particular, a change in c_g/c_h of less than 3 % results in a change by more than 15 % in the population of trans torsion angles at the methyl end of the chain. This illustrates the importance of setting up the MD simulations to reproduces the experimental value of c_g/c_h as closely as possible, although clearly incommensurate systems

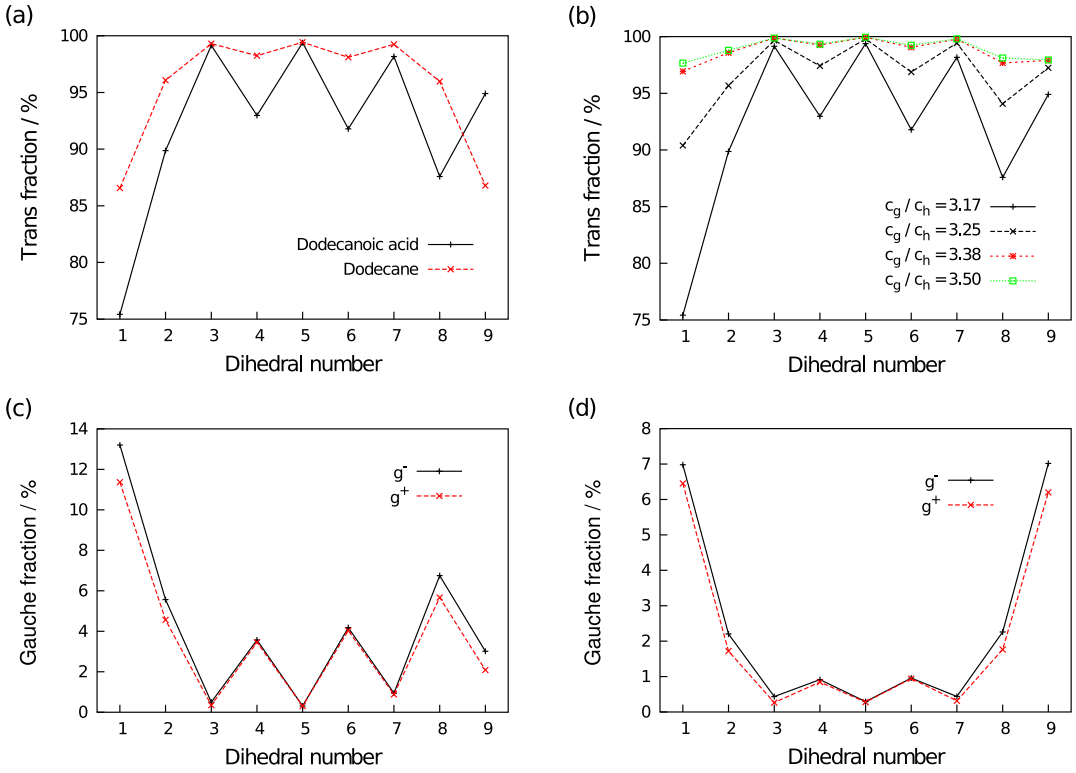

Figure 4.3: Fractional populations of different CH_2-CH_2 dihedral angles in the alkyl chains of the guest molecules, with the angles numbered sequentially from 1 at the methyl end of the chain. Trans fractions are shown for (a) DD/urea and the main DDA/urea simulation, and (b) simulations for DDA/urea with different c_g/c_h ratios. The fractional populations of gauche torsion angles are shown for (c) DDA/urea and (d) DD/urea. In each case, ensemble averages were taken over all guest molecules and over the entire duration of the MD simulation. Lines are drawn to guide the eye. Errors calculated from block averages were found to lie within the size of the data points.

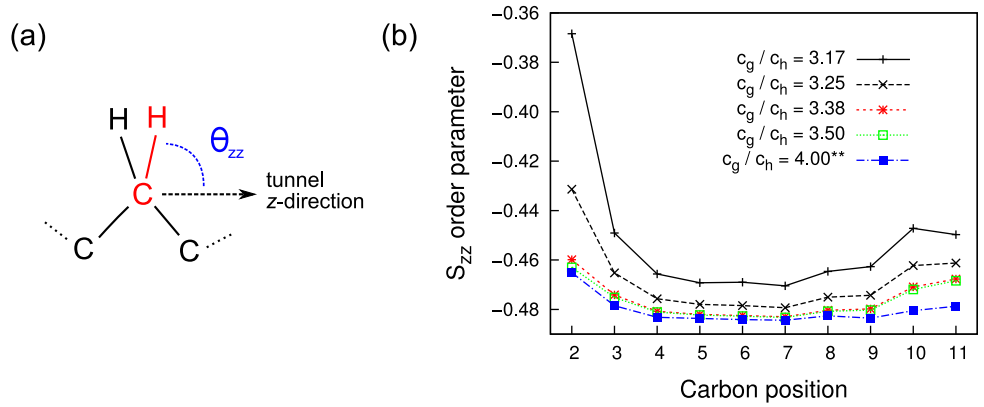

Figure 4.4: (a) The definition of the angle, θ_{zz}, between the C-H bond and the tunnel axis. (b) S_{zz} order parameters for different DDA/urea systems. The sets of results for $c_g/c_h \leq 3.50$ were calculated from the MD simulations in this work, using the θ_{zz} as defined in (a), where each value plotted is the average of both C-H bonds for each position. Ensemble averages were taken over all of the guest molecules and the full simulation time. The results for $c_g/c_h = 4$ are taken from ref. [62], and so correspond to simulations with an entirely different force field (the CHARMM program and force field were used[34]) and set up. Carbon positions are defined such that position 12 is the acid carbon.

can never be simulated with complete accuracy. The sensitivity of the conformational properties of the guest molecules to the specific value of c_g/c_h used in the MD simulation could well explain why the results of previous MD simulations of urea inclusion compounds reported in different papers have led to markedly different estimates of the proportion of conformational defects in the alkyl chains [67, 85, 94].

The interaction of the guest molecules with the host tunnel structure leads to another interesting observation concerning the distribution of torsion angles within the alkyl chain. Figure 4.3(c) and (d) show that there is a significant asymmetry in the preference between gauche plus and gauche minus conformations for the guest molecules in DDA/urea, indicating that the achiral guest molecules exhibit chiral conformational features as a consequence of their interaction with the chiral urea tunnel structure. Calculating the molecular chirality index defined by Neal *et al.* [100] for the DD and DDA guests shows that right-handed conformations are adopted in each case, which matches the right-handed helix of the $P6_122$ urea tunnel. Induced chirality effects have also been noted in previous simulation studies [85, 86] and in experimental EPR measurements [72].

Experimental observations must normally be linked to the underlying molecular motion using models that often need to simplify the behaviour into a limited number of parameters to allow them to be fit to the data. In UIC systems the simplifications normally involve treating the molecule as being rigid and in the all-trans configuration, or with some small defects in the conformations towards the end of the chain. Sufficiently long and accurate MD simulations, however, can be used to calculate experimentally observable properties of the system directly, simultaneously testing the validity of the simulation and linking the molecular behaviour directly to the experimental results.

As described in Section 3.5.1, the guest molecules in the UIC host act like nematic liquid crystals, undergoing rapid rotation about a common axis while maintaining orientational order. The effect of the fast rotational motion on NMR spectra is to average the measured strength of the anisotropic interactions such as the dipolar and quadrupolar couplings. As Section 3.5.1 details, the extent of the averaging in this highly symmetrical case can be described by the Saupe order parameters. In the case of the dipolar and quadrupolar couplings, that are axially symmetric interactions, only the zz order parameter is required, given by,

$$S_{\mathrm{zz}} = \frac{1}{2}(3\cos^2\theta_{\mathrm{zz}} - 1), \tag{4.2}$$

where θ_{zz} is the angle between the z-axis of the interaction tensor (the bond) and the z-axis of the crystal frame (the z-direction of the tunnels, which is parallel to the axis of rotation of the molecules), as shown in Figure 4.4(a). The S_{zz} order parameter contains information about the time-averaged orientations of the interaction tensors. However, it is clear that the orientation of individual C-D bonds can change as a result of many different molecular processes; conformational changes, small angle bending motions, or slight reorientations of the whole molecule, and yet the behaviour of a single parameter cannot be fit to all of the degrees of freedom implicit in these motions. But to gain any insight into the molecular behaviour from experimentally obtained order parameters, simplified models must be used and assumptions made about the important motional forms present.

However, MD simulation can be used to calculate time-averaged values of S_{zz} di-

rectly, as has been done here, with the results for each of the DDA/UIC simulations shown in Figure 4.4. Results from ref. [62] are also included in the same plot for comparison. It is interesting to note that although the results for $c_g/c_h = 4$ are simulated under entirely different conditions, they follow the same trend as the rest of the results; as the repeat distance of the guest molecules increases, the molecules can extend more fully and the ordering of the C-H bonds increases (the angle θ_{zz} is closer to 90°). This observation is also reflected in the relative population of trans dihedral angles in Figure 4.3(b). It would seem that this behaviour depends almost exclusively on the guest packing, and not on the exact force field parameterisation.

In the work of Vold et al. [62], experimental quadrupole measurements were obtained for a deuterated DDA/urea system. They were able to resolve quadrupole coupling constants for the deuterons on the first three carbon positions (numbered 1–3 in the labeling scheme used here). The values they obtained were 25.8±0.1 kHz, 69.5±0.3 kHz and 75.9±0.2 kHz for carbon positions 1, 2 and 3 respectively. They developed a model that links these measured values back to the percentage of defects in the backbone torsions at the chain end, but the fitted quantities were unrealistic, with the final torsion having a lower percentage of gauche defects than the penultimate torsion. They attributed this failing to the presence of correlations between the torsions, which the results here do confirm, but fundamentally this failing demonstrates the inherent difficult of modeling complex motional processes.

An alternative approach is to compare the experimental values directly to those calculated from MD simulation. If the comparison is favourable, the MD simulations can be used to describe the types of molecular processes directly. The difficulty of doing that in this case is that there is insufficient data from the quadrupole coupling measurements to sufficiently compare to the trends in the MD data. However, dipolar coupling measurements can be taken on these systems under conditions in which more of the different sites can be resolved, so they would provide a more useful comparison, and could be used to tune the exact value of c_g/c_h for different types of guest molecules (if a wide range of c_g/c_h ratios can be simulated). This is envisaged as future work.

4.3.3 Structural characteristics of the confined carboxylic acid head-group

The chiral characteristics imposed on the guest molecules by the urea host structure seen in the unequal populations of the two gauche forms, are also evident in the torsion angle describing the orientation of the carboxylic acid head-group. In Figure 4.5, the energy profile for this torsion angle in an isolated DDA molecule in the gas phase is compared with that of a DDA guest molecule confined in the urea host structure. The three minima in the distribution occur at the same positions, but the relative populations are altered significantly by confinement within the urea tunnel structure. In particular, one gauche conformation is preferred strongly over the other gauche conformation, corresponding to an overall distribution which is chiral. The effects of confinement are much more pronounced for this specific torsion angle than for any of the other torsion angles along the alkyl chain, presumably because of its proximity to the carboxylic acid head-group. Thus, the steric constraints associated with accommodating the hydrogen-bonded carboxylic acid head-groups within the urea tunnel structure are influenced significantly by the chirality of the tunnel.

Considering the relationship between neighbouring acid head-groups, there is a strong preference for the classic double hydrogen-bonded dimer arrangement (comprising two O–H...O hydrogen bonds). Over the full ensemble average, 77% of pairs of adjacent DDA molecules have two OH...O distances less than 2.5 Å, and 98.5% of pairs have at least one OH...O distance less than 2.5 Å. Due to the dense packing of guest molecules, pairs of adjacent guest molecules cannot move far enough apart to completely dissociate these hydrogen-bonding interactions, and they exist in dynamic equilibrium between single and double hydrogen-bonded dimers. Comparing these results with those for an isolated DDA dimer in an argon gas, the average intermolecular OH...O distance is slightly longer in DDA/urea (2.12 Å) than in the gas phase (2.07 Å), presumably because the interaction is more strained due to the limited cross sectional area available inside the urea tunnels.

Other structural properties of the DDA dimer are also different in the gas phase and in the urea inclusion compound. Figure 4.6 shows the distributions of three angles

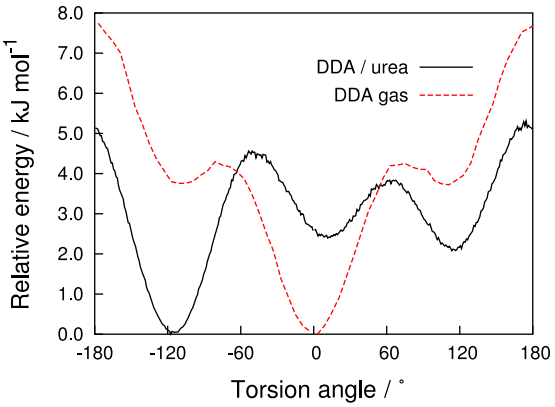

Figure 4.5: Torsional energy distributions for the acid (C–C–C=O) head group in a free gas dimer of DDA and in DDA/urea.

defining the conformation of the dimer: (i) a torsion angle ϕ representing the "twist" of the two carboxylic acid groups with respect to each other, (ii) an angle θ representing the O–H...O angles, and (iii) a torsion angle α describing the relative orientations of the two OH groups. In the gas phase, there is a stronger preference for the oxygen atoms to remain in the same plane (i.e. ϕ close to 180°) and for the hydrogen bonds to be more linear (i.e. θ close to 180°). The most significant difference between the DDA/urea inclusion compound and the gas phase system involves the angle α, for which the DDA dimer in the gas phase has a uni-modal distribution with maximum centred at 180°, whereas the DDA dimers in the urea inclusion compound have a bi-modal distribution with maxima at ca. $(180 \pm 60)°$. Figure 4.7 shows representative structures of DDA dimers illustrating these differences, with (c) and (d) showing cases (for the urea inclusion compound and gas phase respectively) with $\alpha \approx 180°$, and (a) and (b) showing cases (both for the urea inclusion compound) with $\alpha \approx (180 \pm 60)°$. It is probable that the formation of DDA dimer structures with $\alpha \approx (180 \pm 60)°$ provides a means of combining the favourable characteristics of both a double hydrogen-bonded interaction between the carboxylic acid head-groups and a comparatively linear overall conformation of the DDA dimer, which is required in order for them to be accommodated by the tunnel structure.

To investigate the structural relationship between the two molecules in each carboxylic acid dimer, dihedral angles involving corresponding atoms from the two DDA

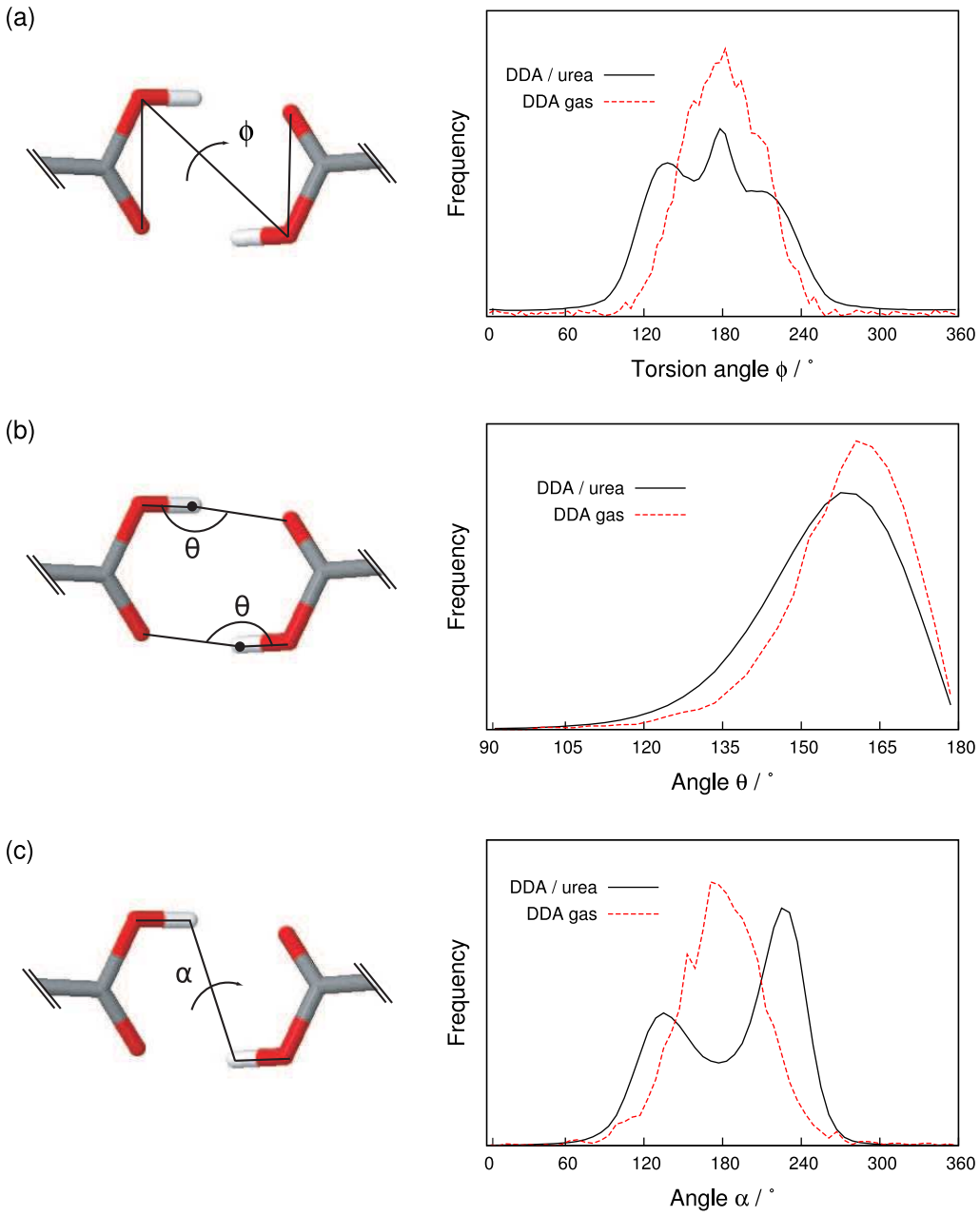

Figure 4.6: Illustrations of three different angles used to describe the conformation of the acid dimer, and the associated distributions from the MD simulations for DDA/urea and the single DDA dimer in argon. (a) The angle ϕ describing the planarity of the oxygen atoms, (b) the angle θ between the O–H bond vector and the carbonyl oxygen, and (c) the angle α between the O–H bond vectors.

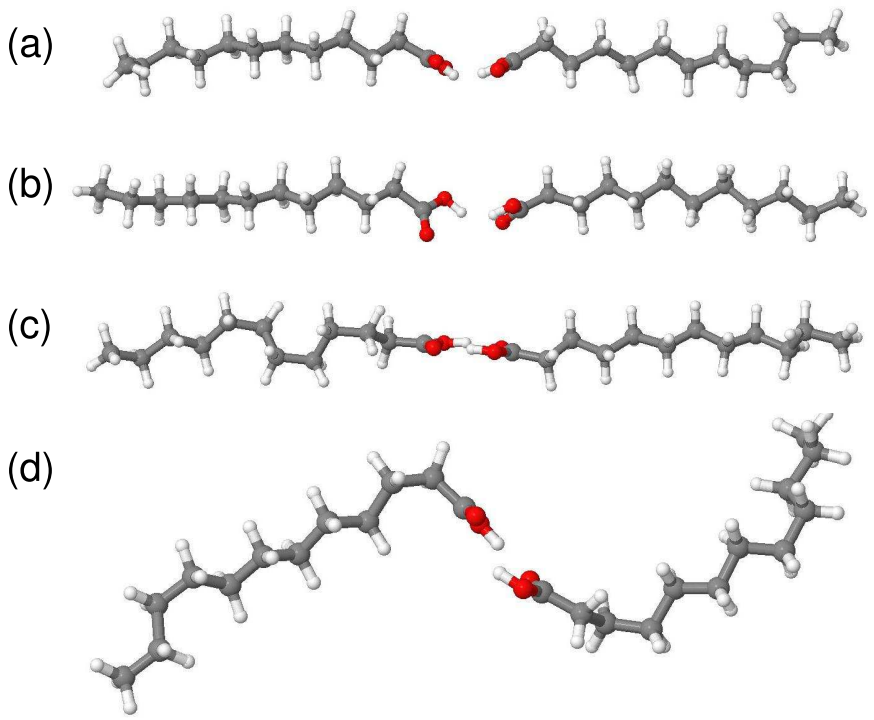

Figure 4.7: Snapshots taken from the MD simulations showing different conformations of the DDA dimer in DDA/urea (a–c) and in an argon gas (d). (a) Predominantly all-trans DDA molecules forming a strained dimer in which the OH groups are forced out of the planar conformation ($\alpha \approx 120°$). (b) As (a) but with only one of the carbonyl oxygens involved in hydrogen bonding. (c) The head groups form a more standard hydrogen bonding, planar arrangement ($\alpha, \phi \approx 180°$) but the torsion angles along the carbon backbone are more strained, with multiple gauche conformations. (d) A snapshot of the DDA dimer in the gas phase showing the conformational freedom of different sections of the molecules to be decoupled.

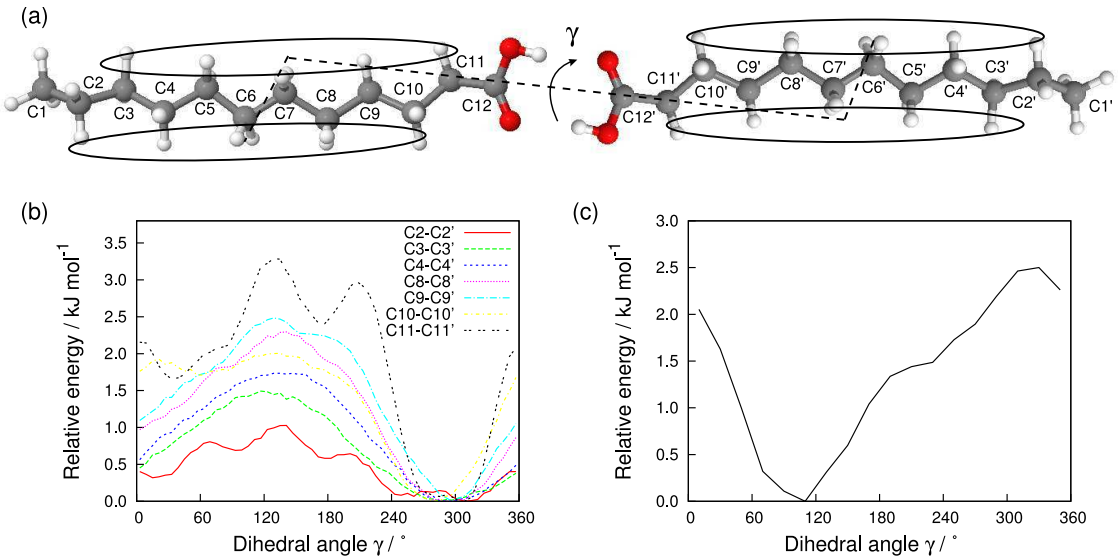

Figure 4.8: (a) The description of the angles and labeling scheme used to calculate distributions of inter-molecular dihedral angles in the DDA dimers for (b) sets of H–C–C–H atoms (using the average hydrogen position on each carbon), and (c), the average planes of the two molecules (using the average of the hydrogen positions in each ellipse in (a) to define the 4 points of a dihedral angle).

molecules in the dimer were calculated, with the labeling scheme shown in Figure 4.8(a). The results in Figure 4.8(b) show that there is a degree of ordering in the inter-molecule dihedral angles, and that it is strongest in the vicinity of the carboxylic acid head-groups (i.e. C12), and gets progressively weaker on moving along the alkyl chains towards the methyl end-group (i.e. C2). The corresponding results for the DDA dimer in the gas phase indicate a minor degree of ordering in the first inter-molecule dihedral angles (C11-C11), but no ordering in the other dihedral angles along the alkyl chain.

The relative orientations of the molecular planes within each DDA dimer have also been calculated. As shown in Figure 4.8, the average position of all hydrogen atoms on the odd-numbered methylene groups and the average position of all hydrogen atoms on the even-numbered methylene groups were calculated separately for each of the two molecules in the dimer, representing the four points needed to define a dihedral angle. Results from the ensemble average of this dihedral angle, shown in Figure 4.8(c), reveal that the molecules in the dimer have a preference for a relative orientation in which their planes are rotated by ca. 100–120° with respect to each other. This chiral, relative orientation corresponds to the gauche minus configuration. Thus, in addition to the fact, discussed above, that the intra-molecular conformation of individual DDA guest

molecules within the urea tunnel structure are chiral (also favouring the gauche minus conformation as in Figure 4.3(c) and (d)), the relative orientations of the two molecules within the DDA dimers also lead them to have an overall chirality.

4.3.4 Positional ordering of the guest molecules

The relatively large sizes of the MD simulation cell and overall duration allow the possibility of considering the evidence for positional correlations between guest molecules in adjacent tunnels. The analysis of such correlations must be interpreted with some caution, as the simulation cell comprised only nine tunnels (i.e. each tunnel is adjacent to 75 % of the other tunnels in the system). As shown in Figure 4.9, the simulations do suggest a significant degree of correlation between the positions of the guest molecules in adjacent tunnels for both DD/urea and DDA/urea. The observed correlations are unlikely to be an artefact of the starting configurations used, because, as shown in Figure 4.10, the guest molecules diffuse by a greater distance along the tunnels during the simulation than the distance over which these inter-tunnel correlations appear to act. The energy surfaces are periodic with a repeat distance corresponding to the value of c_{g} for the specific system, implying that the inter-tunnel positional ordering is controlled by guest...guest interactions rather than host...guest interactions.

Weak correlations in the positions of guest molecules in adjacent tunnels are evident from X-ray diffraction studies of many conventional urea inclusion compounds, as they show a distinguishable diffraction pattern due solely to the ordering of the guest molecules. Sheets of diffuse scattering perpendicular to the tunnel direction are a result of one dimensional order of the guest molecules along the tunnels, while in some urea compounds there are also discrete diffraction maxima in the guest's diffraction pattern, indicating that there is also three dimensional ordering of the guest molecules in these cases [58]. This three-dimensional ordering corresponds to weak correlations in the positions of guest molecules in adjacent tunnels, and is defined in terms of the parameter, Δ_{g} [101], which specifies the average offset along the tunnel axis between guest molecules in neighbouring tunnels. It is known that in UIC systems containing alkanes, the guest molecules in neighbouring tunnels tend to align with one another, so in this case $\Delta_{\mathrm{g}} = 0$. Other families of guest molecules, however, have different charac-

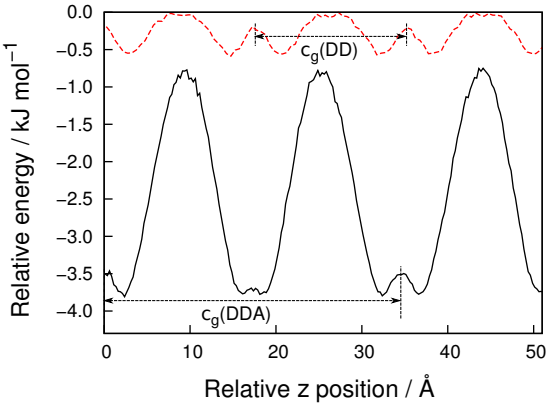

Figure 4.9: Histograms illustrating the energies of the relative positions of the guest molecules in neighboring tunnels for the DDA/urea and the DD/urea systems. Statistics were compiled by picking a single reference molecule in each tunnel and finding the relative distance along the z-axis to all the molecules in the 6 neighboring tunnels. In the DD/urea system the centre of mass of each molecule was used as the reference and in DDA/urea the centre of mass of each dimer was used. Energies are given relative to the maximum energy state in each system, with the plot for DDA/urea shifted vertically for clarity.

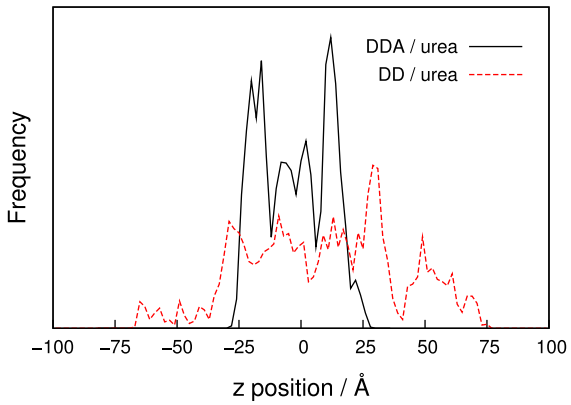

Figure 4.10: The diffusion of a single guest molecule over the course of the full simulation.

teristic modes of inter-tunnel ordering corresponding to other values of Δ_g [101, 102]. The behaviour for urea inclusion compounds containing carboxylic acid guest molecules has not been reported in the literature and the diffraction studies on DDA/urea that were provided for this work did not show any discrete diffraction maxima.

The energies involved in the plots shown in Figure 4.9 are low compared to the thermal energy of the system (approximately 2.5 kJ mol^{-1} at 300 K) and thus the molecules are highly mobile and explore a considerable range of Δ_g values. However, there are well-defined minima about $\Delta_g \approx 0$, corresponding to a preference for molecules in neighbouring tunnels to occupy the same set of z-coordinates along the host tunnel. This is compatible with the value of $\Delta_g = 0$ (for DD/urea) observed by X-ray diffraction. In the case of DDA/urea, there are equally strong minima associated with $\Delta_g \approx c_g/2$, corresponding to the acid head-group of the DDA molecules in one tunnel having the same set of z–coordinates as the methyl-end-groups. The significantly stronger correlations in DDA/urea must correspond to an increase in the strength of the interactions between guest molecules in neighboring tunnels, presumably due to the more polar nature of the acid head groups compared to the alkane chains. Indeed, the presence of two distinct minima strongly suggests that more than one factor determines the preferred Δ_g values. This is likely to involve a combination of steric and polar factors e.g. favourable electrostatic interactions between acid head groups at the $\Delta_g \approx 0$ minimum and favourable sterics at $\Delta_g \approx c_g/2$ when the bulky acid head groups in one tunnel are closest to the "gap" between the methyl-end-groups in the neighboring tunnel.

Both energy profiles in Figure 4.9 show two weaker minima, an amount $\delta \approx$2–3 Å either side of the principal inter-tunnel correlations at $\Delta_g \approx 0$ (and at $\Delta_g \approx c_g/2$ for DDA/urea, although the effect is much less pronounced). Not only is the size of the 'splitting' itself approximately equal for both systems, but the energy barrier it introduces is of the same magnitude, ca. 0.3 kJ mol^{-1}. Figure 4.11 shows one possible explanation for this splitting; if a slight offset is introduced at configurations where $\Delta_g \approx 0$, the conformationally disordered, dynamic chain-ends of adjacent molecules no longer overlap, but instead occupy positions in the tunnel adjacent to the free spaces between their neighbours (as in Figure 4.11(a) and (c) where the centre of the space is

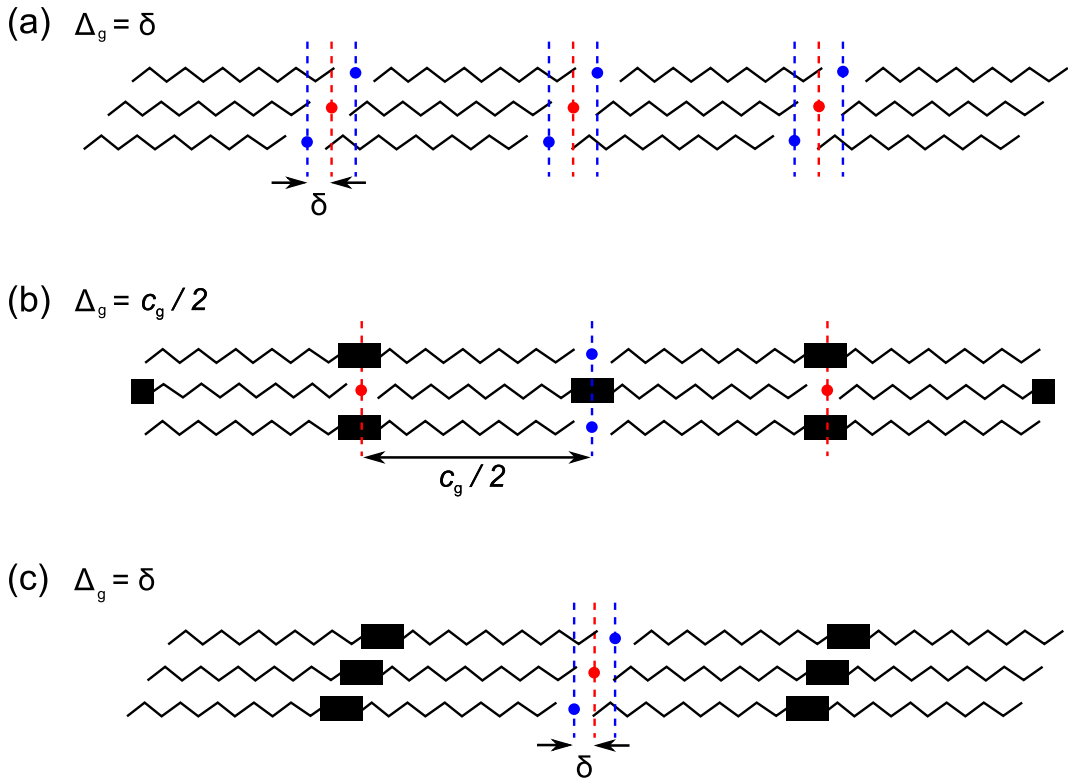

Figure 4.11: Representations of the molecular positions corresponding to one possible explanation of the minimum energy configurations in Figure 4.9 for (a) DD/urea, and (b) and (c) DDA/urea. To illustrate the origins of the splitting (δ) of the energy minima, the centre of the spaces between the guest molecules (or dimers) are used to define their relative positions (marked as filled circles), rather than using their centres of mass. The offsets are given relative to the central row of molecules, whose positions are marked in red, while markings for both of the outer rows of molecules are in blue.

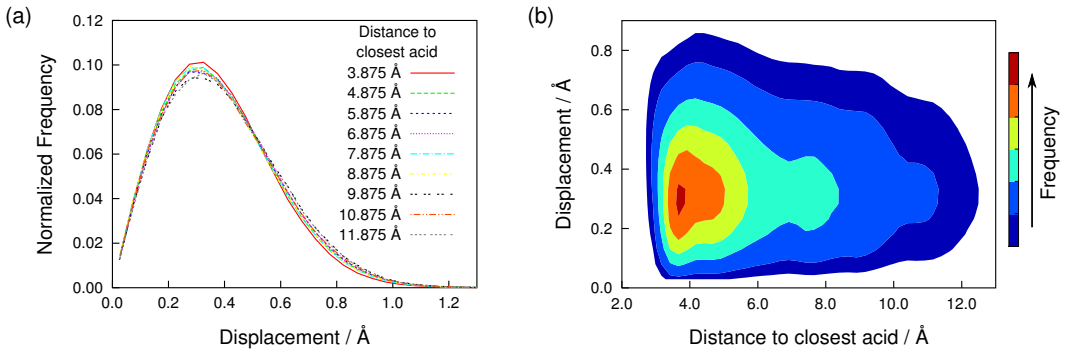

Figure 4.12: Assessment of whether the urea tunnel structure is distorted locally by the acid head-groups in DDA/urea. The displacement of the central carbon of each urea molecule was measured from its starting position along an axis perpendicular to the tunnel direction. The distance to the closest acid head-group was taken as the distance of this central carbon to the nearest oxygen atom on a DDA molecule. (a) Shows normalized frequency distributions for the displacements of the urea molecules at distinct values for the distance to the closest acid head-group and (b) shows the full surface describing the correlation between the urea displacement and the acid distance.

marked by a coloured circle). The splitting itself is due to the fact that the molecules in neighbouring tunnels can diffuse by an equivalent amount $\pm\delta$ to achieve their preferred configuration. In this scheme, the reason why the splitting is less evident for the case in the DDA/urea where $\Delta_g \approx c_g/2$ (Figure 4.11(b)) is that the bulky dimer head groups already occupy the region neighbouring the available free space. Observing this behaviour using XRD would be extremely difficult and perhaps not possible because the effect is only very slight, and would be averaged by the rapid dynamics of the guest molecules on the timescale of the experiment.

4.3.5 Host-guest interactions

The mechanism for the inter-tunnel correlations of the guest molecules discussed above is unclear; are the interactions mediated by the host molecules or entirely due to non-bonded interactions between the guest molecules themselves? If they are mediated by the host molecules, then the host structure would be expected to distort in the region of the guest molecules, particularly in the DDA/urea system, as the acid head groups are far bulkier than the alkyl chain of the DD guest.

Figure 4.12 shows the relation between the displacement of each urea molecule

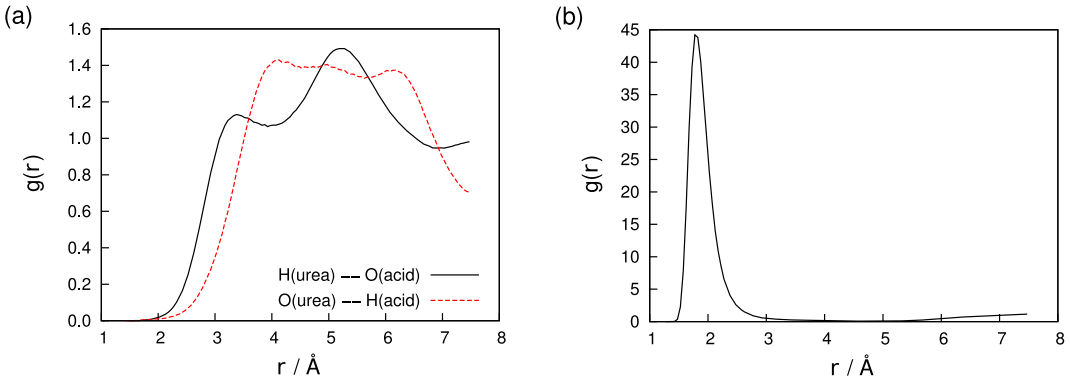

Figure 4.13: Radial distribution functions for (a) the distances between the carbonyl oxygen atom of DDA and the urea hydrogen atom, and between the urea oxygen atom and the hydrogen atom of the carboxylic acid group in DDA, and (b) the distance between the carbonyl oxygen atom of one carboxylic acid group and the hydrogen atom of the neighboring carboxylic acid group. Only the latter shows clear hydrogen bonding behaviour.

from its initial position (in the structure determined from X-ray diffraction) and the proximity of the urea molecule to a carboxylic acid group of the guest (assessed from the distance between the centre of the urea molecule and the nearest oxygen atom of a DDA guest molecule). The results in Figure 4.12 show that there is significant displacement of the host structure, but indicate that the distribution of urea displacements is essentially independent of the urea...carboxylic acid distance, suggesting that the displacements of the urea molecules are uncorrelated with their proximity to the carboxylic acid groups. A similar analysis of the orientational distributions of the urea molecules suggested that the orientational characteristics of the urea molecules are also uncorrelated to their proximity to the carboxylic acid groups of the DDA guest molecules. It is possible that the overall motion of the urea molecules could mask very subtle correlations but this would seem unlikely, leaving only the possibility that the inter-tunnel correlations are the result of non-bonded forces acting between guest molecules in adjacent tunnels.

It has been demonstrated that host-guest hydrogen bonding can exist in systems with commensurate di-ketone guests [103], where the distance between the ketone groups matches the urea host structure in such a way as to allow the creation of a hydrogen-bonded superstructure. However, host-guest hydrogen bonding is not ob-

served in diffraction studies of incommensurate urea inclusion compounds, leaving only the possibility of temporary interactions such as those proposed by Menziani et al. in their work on the (hypothetical) case of a single carboxylic acid dimer included within a urea tunnel structure [86]. Their simulation was highly unphysical however, with semi-constrained urea molecules forming just one channel. To investigate the possible formation of host-guest hydrogen bonding in the case of DDA/urea, radial distribution functions were constructed from the results of our MD simulation. The results (shown in Figure 4.13) suggest that there is no significant urea...DDA hydrogen bonding.

4.4 Conclusion

Carefully performed molecular dynamics simulations of urea inclusion compounds containing carboxylic acid and alkane guests have been used to investigate the properties of these systems in great detail, leading to insights into subtle aspects of the structure and dynamics of the host and guest structures. The simulations are larger and were run for longer than any reported in the literature. A comparison of results between systems set up containing slightly different densities of acid guest molecules has shown how sensitive their internal conformations are to their packing and thus the importance of using the correct value in simulations, which is not the case in many previous studies.

The simulations show that the confinement of the guest molecules within the urea tunnels affects their internal conformations considerably. Firstly, by imposing the inherent chirality of the host tunnels onto the guest molecules. Secondly, the backbone dihedral angles in the guest, which occupy mostly trans positions inside the tunnels, become correlated over long distances (even across the different molecules in the acid dimer guests) so that if disorder in one part of the molecule leads to an increased interaction with the tunnel walls, it is compensated for by defects in other parts of the chain. Correlations such as these, and those acting between the positions of guest molecules in adjacent tunnels, are difficult to study by experimental methods but are readily accessible to MD simulation.

Not only are urea inclusion compounds an interesting example of a system in which highly dynamic processes occur within solid structures, they are also an example of a

system which has proved difficult to understand using experiment alone. This is because the interpretation of experimental results always relies on models of the underlying molecular behaviour that are fraught with approximations that can lead to important considerations being ignored. Molecular dynamics simulations can provide a direct link between experiment and the underlying molecular motion, validating both the simulation and the molecular model, and also providing a platform through which the system can be investigated in much more detail.

Acknowledgements

Dr. Sebastian Palucha set up and ran the dodecane/UIC system. Dr. Andrei Batsanov performed single crystal XRD on the dodecanoic acid/UIC compound to provide the $c_{\mathrm{g}}/c_{\mathrm{h}}$ ratio and look for evidence of inter-tunnel correlations and the associated Δ_{g} value.

Chapter 5

Elucidation of structure and dynamics in solid octafluoronaphthalene from combined NMR and molecular dynamics studies

5.1 Introduction

Octafluoronaphthalene (OFN), $C_{10}F_8$, is a simple molecular solid at room temperature. Its structure, described in more detail below, consists of alternating stacks of the molecules in a flattened herringbone configuration [104]. The pure form of the compound has limited commercial applications, although it has frequently been used as a model system for ^{19}F solid-state NMR [105–107]. However, the octafluoronaphthalene molecule has been proposed as a "supramolecular synthon" [104] (a basic building block for crystal engineering) because it interacts in a predictable way with other aromatic molecules.

For such an apparently simple system, it is surprising that the precise structure of OFN, as well as a good understanding of its phase behaviour, remained enigmatic for some time. Early single crystal work at ambient temperature (corresponding to the form labeled as I-OFN) obtained a structure with an unsatisfactory R factor of 35% [108], with refinements also yielding unphysical bond lengths and molecular ge-

ometries. The origin of the difficulty in the refinement is in the high level of thermal diffuse scattering and the rapid fall off of the Bragg intensities with increasing Bragg angle [108, 109]. These properties are an indication that there is disorder present in the system, but a structure accounting for this disorder was not refined against the diffraction data until recently [25, 110]. Figure 5.1(a) illustrates the refined structure from [25], with the unit cell (indicated by the rectangle) containing two molecules, in the $P2_1/c$ space group. The molecular disorder was fitted as two alternative orientations of the molecule, both centered at the same crystallographic inversion centre, co-planar within 1° but differing by a ca. 38° rotation around the molecular C_2 axis, as shown in Figure 5.1(d). The relative occupancy of these two orientations was included in the refinement, converging at 54.2(7) and 45.8(7)%. This refinement yielded a much improved R factor of 3.1% which is extremely favourable compared to the ordered refinements, and is also a notable improvement on the R factor reported by Cozzi et al. [110] of 11.6% using a model that also differentiated between two molecular orientations.

The phase behaviour of OFN has also been complicated to study. On cooling, I-OFN has been shown to transform into one of two different low temperature structures (II-OFN or III-OFN) at a common transition temperature of approximately 266.5 K [25, 111–113]. Unusually, there is no change of space group upon the transitions and all three structures adopt the $P2_1/c$ space group. The transition into II-OFN involves a doubling of the unit cell in the $\bar{a}$ direction and has been observed to be accompanied by the shattering of the crystallites, meaning that studies have been done either on powder samples [112] or any of the larger constituent single crystals that remain [111]. There is also a hysteresis in the transition temperature, with the transition on heating occurring at 281.8 K. Both this, and the destruction of the crystal, indicate that the transformation from I-OFN to II-OFN is a first order phase transition involving a relatively large rearrangement in structure. Meanwhile, the transformation from I-OFN to III-OFN would appear to require very little rearrangement of the structure, as single crystals can survive the transition, allowing high quality structures to be resolved [25, 113]. The unit cell of III-OFN, shown in Figure 5.1(b), has reduced symmetry compared to the structure of the high temperature phase (Figure 5.1(a)). However,

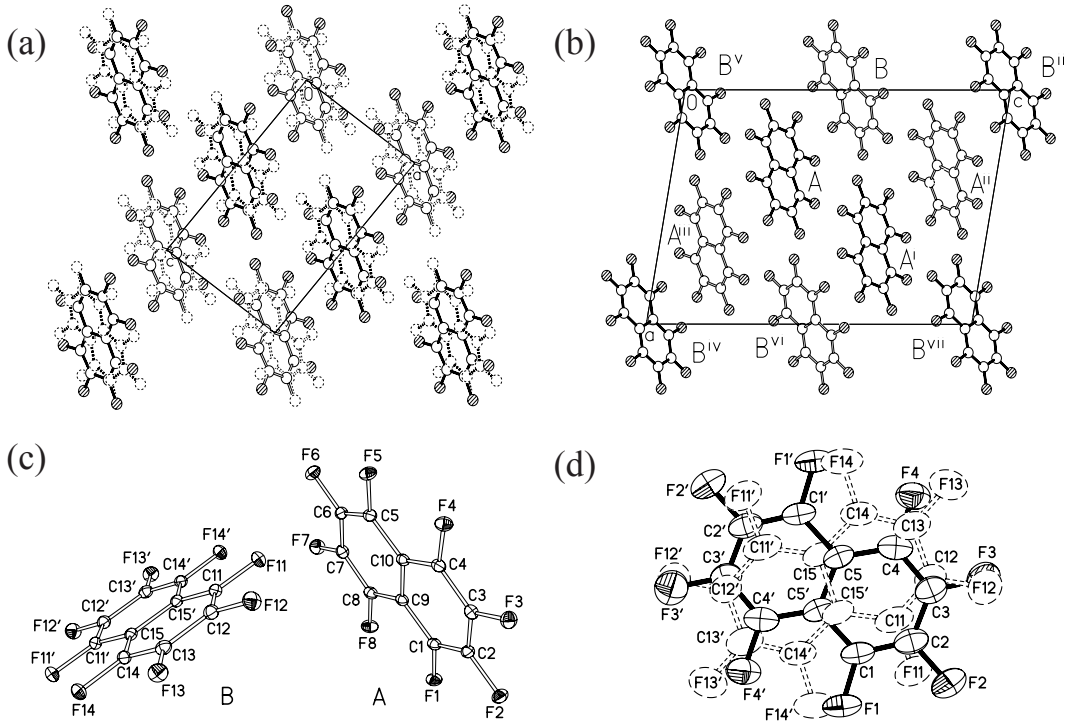

Figure 5.1: Crystal packing of (a) I-OFN and (b) III-OFN; (c) the two independent molecules, A and B, of III-OFN, (d) illustration of the molecular disorder in I-OFN. Thermal ellipsoids are drawn at the 50% probability level. Primed atoms are those generated by inversion centres.

the structures are very similar, the disordered molecular orientations in I-OFN being the main difference between the two [25].

The early NMR work actually linked the dynamics with the (as yet unknown) phase transition in the material [105]. Their measurements of the ^{19}F spectrum of OFN showed a considerable drop in width as the temperature was increased through the region of the phase transition between ca. 230 and 285 K, indicating the presence of dynamics. The line narrowing was not observed to be accompanied by any changes in the chemical shift anisotropy, however, meaning that the motional process they were observing left the molecule unchanged. They concluded, by analogy to similar behaviour observed in hexafluorobenzene, that the molecules undergo a 180° in-plane rotation about the C_2 axis perpendicular to the molecular plane. This in-plane rotation is a similar process to the model used to fit the XRD, but the 40° jump inferred there is too small to explain the observed drop in the NMR linewidth. The onset of the dynamics in the temperature range associated with the phase transition is also interesting and provides a clue as to the nature of the transition itself.

Although there is an abundance of evidence describing the behaviour of octafluoronaphthalene on both the molecular and macromolecular level, what is lacking is a model that encompasses it all. In this work, ^{19}F NMR relaxation measurements have been used together with the results from detailed molecular dynamics (MD) simulations to construct and develop such a model. The relaxation time measurements yield quantitative estimates of the rates of dynamic processes in the system on two distinct timescales but cannot determine the types of molecular motions that those processes actually correspond to. The MD can, however, and provides a model for the underlying molecular behaviour that can be linked quantitatively with the relaxation measurements, as well as qualitatively with the structural observations from the diffraction measurements, proving that the observed disorder is dynamic in nature. This detailed knowledge of behaviour of the system at a molecular level also leads to a deeper understanding of the phase transitions.

5.2 Experimental

5.2.1 NMR

Initial experiments were performed using a Varian InfinityPlus, spectrometer with an 11.7 T magnet and an operating frequency for ^{19}F of 470.4 MHz. After problems were encountered with the consistency of the variable temperature measurements (which was later understood in terms of the unpredictable phase behaviour of the compound), the reproducibility of the results was checked at a lower field, on a Varian UnityPlus spectrometer operating at a frequency of 282.2 MHz for ^{19}F. This lower field gave the benefit of reducing the line broadening effects of the chemical shift anisotropy, which is proportional to the field strength (see Equation 3.19). These results were found to be consistent, and they account for all of the measurements of the ^{19}F T_1 and $T_{1\rho}$ time constants presented here. Octafluoronaphthalene (97 %) was purchased from Alfa Aesar and samples were packed into 4 mm o.d. magic-angle spinning (MAS) rotors. Although commercial samples typically contain small quantities of chlorinated source materials, these are at too low a level to influence the NMR measurements (this was confirmed by test measurements on high purity samples obtained by vacuum sublimation). Two different types of relaxation were measured:

The **spin-lattice relaxation, T_1**, was measured using the saturation recovery pulse sequence [114]. The pulse sequence and vector model representation of what happens to the bulk magnetisation during the sequence are shown in Figures 5.2(a) and (b) respectively. The cycled $\frac{\pi}{2}$-pulse and associated delay at the beginning of the sequence act to saturate the bulk magnetisation (a delay of 10 μs and a total of 50 cycles were found to adequately saturate the signal). The magnetisation is then left to recover for an array of different times, τ, before a final read pulse tips the bulk magnetisation back into the xy plane and the signal is acquired. The integrated intensity of the central peak was then plotted as a function of τ to yield an exponential increase in the magnetisation that could be fitted to obtain a value for T_1. This sequence was chosen over possible others because it does not require the system to fully relax in between acquisitions, allowing a much shorter recycle delay to be used (2 s as opposed to around 30 s which would be needed for the bulk magnetisation to completely relax

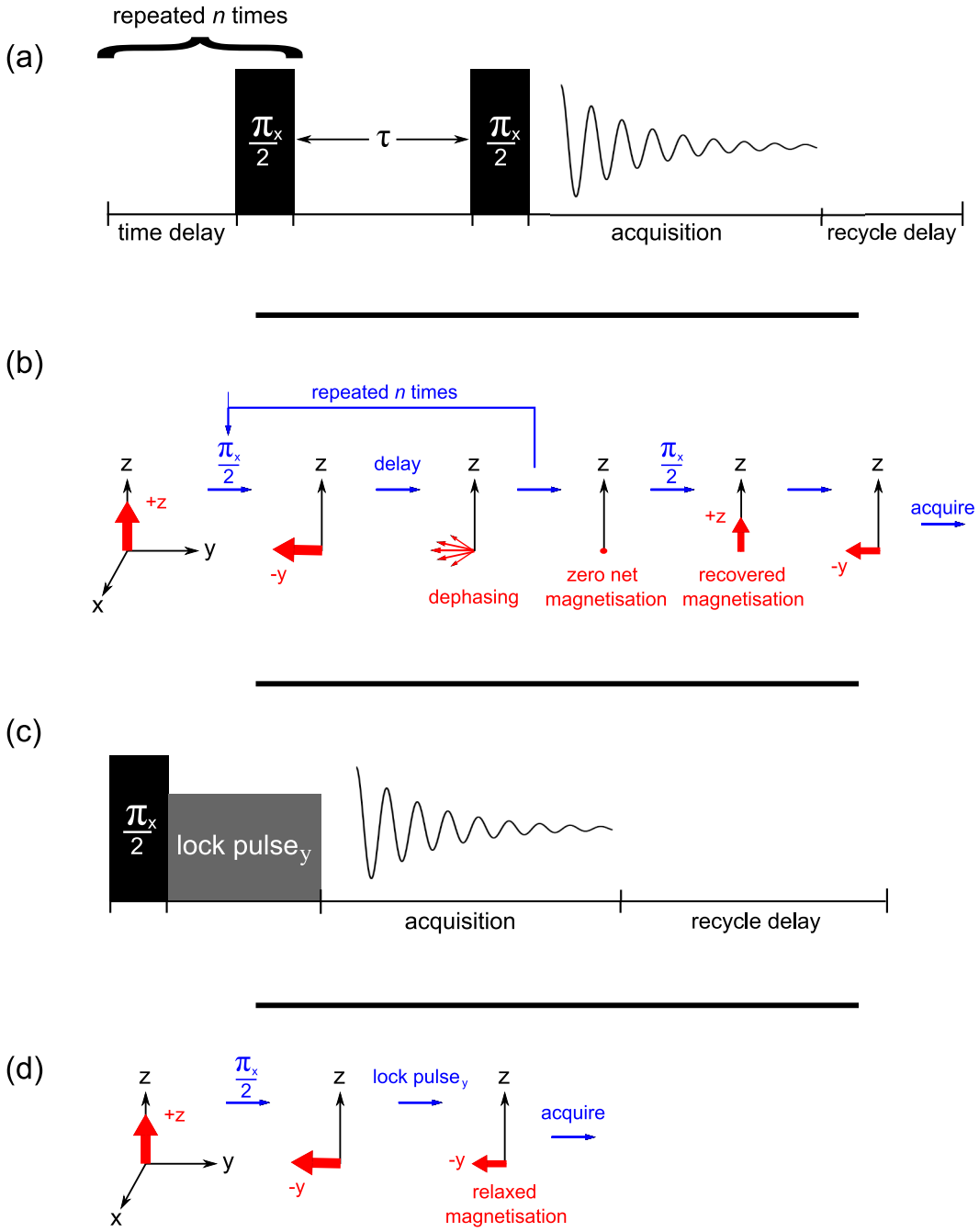

Figure 5.2: Pulse sequences and their descriptions using the standard vector model for the saturation recovery experiment used to measure T_1 spin-lattice relaxation, (a) and (b), and the spin-lock experiment used to measure $T_{1\rho}$ spin-lattice relaxation in the rotating frame, (c) and (d). In (a) and (c) the time axis is not drawn to scale.

in octafluoronaphthalene). It is only appropriate for systems where $T_2 \ll T_1$ (i.e. when the *xy* dephasing is a lot quicker than the recovery of the *z*-magnetisation back to equilibrium), which is common in solids. Data sets were acquired under magic-angle spinning using a MAS rate of 8 kHz and on static samples.

The **spin-lattice relaxation in the rotating frame, $T_{1\rho}$**, was measured from the decay of spin-locked ^{19}F magnetisation, using the pulse sequence shown in Figure 5.2(c). The effect of the pulses on the bulk magnetisation is illustrated in Figure 5.2(d); the magnetisation is flipped onto the -*y* axis by the initial $\frac{\pi}{2}$-pulse and it is locked there by a second pulse. The signal relaxes at a rate of $\frac{1}{T_{1\rho}}$ while the lock pulse is on and the signal intensity as a function of the lock time is fitted to extract $T_{1\rho}$. A ^{19}F RF nutation frequency of 83.3 kHz was used for the lock pulse. It was found that it was difficult to maintain an effective spin-lock over the full spectral width because of the wide ^{19}F spectrum. Because of this, experiments were carried out on a static sample and the intensity variation was studied at the spectral frequency that the transmitter was placed at.

The relaxation times were measured between –15 and 50 °C in increments of 5 °C. Below about –15 °C transformations into other forms occur (as discussed below) and results in this range were poorly reproducible. Both sets of relaxation data fitted well to single exponential curves, and fractional errors estimated from the fitting residuals were typically < 0.5 %.

5.2.2 Differential scanning calorimetry

The NMR results from the temperature regions below and around the phase transition in OFN were observed to be erratic and irreproducible. The problem was investigating using differential scanning calorimetry (DSC). Heating and cooling cycles were run between 303 K and 183 K with temperature ramps of 0.5 K / minute. The results presented here were obtained using a Thermal Advantage DSC Q1000, although the experiments were also repeated on two other instruments to ensure that the unusual spikelet behaviour (see Figure 5.10) was reproducible, which it was.

5.3 MD simulations

Analysis was performed on atomistic molecular dynamics simulations that were set up and run by Dr. S. Palucha. Each of these simulations consisted of 144 octafluoronaphthalene molecules using periodic boundary conditions in each dimension. The first system corresponded to the high temperature phase (I-OFN), with the initial atomic positions taken from the atomic coordinates given by the recent XRD study [25]. The repetition of the crystallographic unit cell to create the simulation block corresponds to an initial configuration with ordered "stacks" of molecules, in which half the stacks adopted one of the two "orientations" and half the alternate orientation. However, as discussed below, the orientations of the molecules quickly randomise during the simulation, which was carried out at 290 K. The second simulation system corresponded to III-OFN, with the starting configuration again taken from the XRD studies, and was run at two temperatures, 100 K (at which the phase is stable), but also at 290 K (where it is not stable).

The force field used had been fitted to optimise its accuracy for OFN (specifically, to match experimentally determined densities and *ab initio* interaction profiles). Details of the fitting procedure are given in the supplementary information of [25], along with the optimised parameters. The simulations were run using DLPOLY 2.18 [90]. Long range electrostatics were calculated using the Ewald sum method using a short-range cutoff of 1.2 nm. The system was equilibrated for 0.5 ns to the correct temperature, followed by a further 1.0 ns equilibration with unconstrained bond lengths. The bond lengths were then constrained using the SHAKE algorithm [115]. The simulations used the Nose Hoover algorithm [28] to run at constant pressure and temperature, using a 2 fs timestep. Atomic trajectories were sampled every 2 ps over 100 ns in the case of the high temperature phase. A shorter production run of 8 ns was used for the low temperature simulation.

5.4 Analysis

5.4.1 NMR

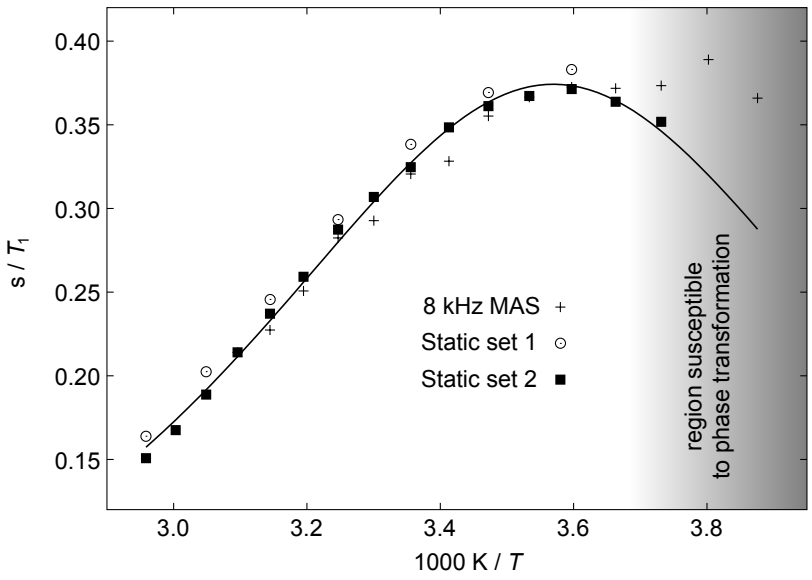

Figure 5.3: Compiled results from three sets of variable temperature T_1 measurements on octafluoronaphthalene. Error bars on the individual data points from the exponential fitting are of the order of the size of the symbols. The curve is a fit of the filled square data points to Equation. 5.2.

Figure 5.3 shows the variation of the ^{19}F spin-lattice relaxation time constant with temperature. Above the onset of the phase transition (about –15 °C or $1000\,\mathrm{K}/T \approx 3.8$) the results are highly reproducible and show the classic behaviour which is associated with the functional form of the spectral density function, as described in Section 3.5.2: there is a maximum when the relaxation is driven most efficiently by the molecular motion, which is when the rate of the motional process is of a similar order to the ^{19}F NMR frequency ν_0 (here 282 MHz). At temperatures either side of this maximum, which occurs at about $1000\,\mathrm{K}/T \approx 3.6$ here, the relaxation is less efficient and hence the relaxation times increase.

Although the results should, strictly speaking, be fit against a linear combination of spectral densities, as in Equation 3.39, the contributions from the terms at slightly

different frequencies cannot be distinguished. Therefore, the results are simply fit to a single spectral density term at $J(\nu_0)$, so that the rate of relaxation $(1/T_1)$ is proportional to $J(\nu_0)$.

To describe the temperature dependence of the rate of the motional process, it is assumed to be thermally activated and following Arrhenius-type behaviour. Here, the time constant at a given temperature can be written solely in terms of the activation barrier, E_a, for the process and its rate constant at 0 K, τ_0,

$$\tau = \tau_0 \exp(E_a/RT). \tag{5.1}$$

This can then be substituted into Equation 3.38 to obtain an expression for the variation in the relaxation time as a function of temperature,

$$\frac{1}{T_1} \propto \frac{\tau_0 \exp\left(\frac{E_a}{RT}\right)}{1 + (2\pi\tau_0\nu_0)^2 \exp\left(\frac{2E_a}{RT}\right)}. \tag{5.2}$$

It was possible to fit the full form of Equation 5.2 (to both sets of relaxation measurements obtained here) because sufficient data were obtained on each side of the maximum. The fit shown in Figure 5.3 gave an E_a of 20.6 ± 0.4 kJ mol^{-1}, and a τ_0 of $8 \pm 1 \times 10^{-14}$ s.

Figure 5.4 shows the corresponding plot for the measurements of $T_{1\rho}$. The data points are again fit to Equation 5.2 but for $T_{1\rho}$ it is the relation between the rate of motion and the frequency of the RF used for the lock pulse (here, $\nu_1 = 83.3$ kHz) that governs the position of the maximum. This fundamental difference, coupled with the fact that the maximum lies in a similar temperature range to that from the T_1 measurements, proves that the motional processes observed in each experiment must be distinct. Accordingly, the fitted parameters are significantly different to those obtained for the T_1 results, with an activation barrier of 55.1 ± 1.3 kJ mol^{-1} and time constant, τ_0 of $4 \pm 2 \times 10^{-16}$ s.

Unfortunately, from these results alone it is not possible to prove anything about the nature of the molecular motion other than the fact that the molecules are mobile and there are processes on two distinct timescales. However, it seems physically reasonable that the faster motion that drives the T_1 relaxation corresponds to the molecules

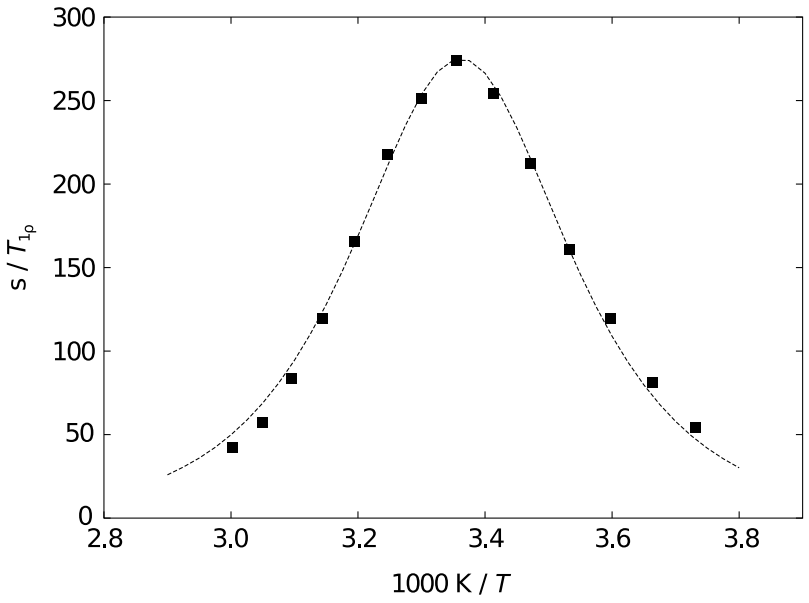

Figure 5.4: Results from variable temperature $T_{1\rho}$ measurements, together with the fit used to extract the kinetic parameters. Error bars on the individual data points are of the order of the size of the symbols used.

jumping between the two orientations seen in the X-Ray studies [25], suggesting that the disorder observed there is dynamic in nature. Likewise, it is possible that the slower process corresponds to the full rotation of the molecule inferred by the previous NMR results [105]. However, this assignment is less convincing, firstly because the motion itself does not seem physically realistic; the NMR results compared the case of OFN with fluorobenzene, a very different molecule in which the full (C_6) rotation requires much less free volume. Secondly, the existence of two molecular orientations precludes a simple mechanism by which the molecule can rotate between symmetrically equivalent sites, therefore the form of the dynamics must be more subtle than a 180° jump.

5.4.2 Molecular dynamics

5.4.2.1 Molecular motion

The rigid nature of the octafluoronaphthalene molecules and their confinement within a well-defined crystalline structure mean that the key degrees of freedom are those describing the molecular orientation. Although the evidence from the XRD and previous NMR suggested that the most significant motion should be the in-plane rotation, it was clear from initial investigations of the MD trajectory that the molecules can also tilt out of the plane. Therefore, defining a single molecular axis and taking the dot product with itself at each time step was not sufficient to specify the change in the orientation uniquely (the angle would incorporate the tilt and the rotation). Instead, it was necessary to define a molecular frame so that polar angles could be used and the orientations defined uniquely.

Figure 5.5(a) illustrates the form that the molecular frame took, with the $\vec{x}$ and $\vec{y}$ axes first determined by the vectors pointing between specific carbon atoms around the ring, with the $\vec{z}$-axis then taken as the cross product of $\vec{x}$ and $\vec{y}$. This frame was calculated for each molecule at the first step of the simulation (after the equilibration period) and the average taken to define a single, common reference frame ($\vec{x}_0$, $\vec{y}_0$, $\vec{z}_0$), allowing the data from all of the molecules to be combined. This approach is justified because, when the effect of the orientational disorder has been included, all of the lattice sites are symmetry-related (although this is complicated by the correlations, as discussed later).

The orientation of a given molecule at a particular timestep was specified by the rotation of its molecular frame with respect to the reference frame. To decouple the in-plane rotation, ϕ, from the out of plane 'tilt' motion, θ, of the molecules, projections of the $\vec{y}$ and $\vec{z}$ vectors onto the $\vec{x}_0\vec{y}_0$ and $\vec{y}_0\vec{z}_0$ planes,

$$\vec{y}_{\mathrm{p}} = \vec{z}_0 \times (\vec{y} \times \vec{z}_0), \tag{5.3}$$

$$\vec{z}_{\mathrm{p}} = \vec{x}_0 \times (\vec{z} \times \vec{x}_0), \tag{5.4}$$

were used to calculate the relative orientations, which are simply the polar angles

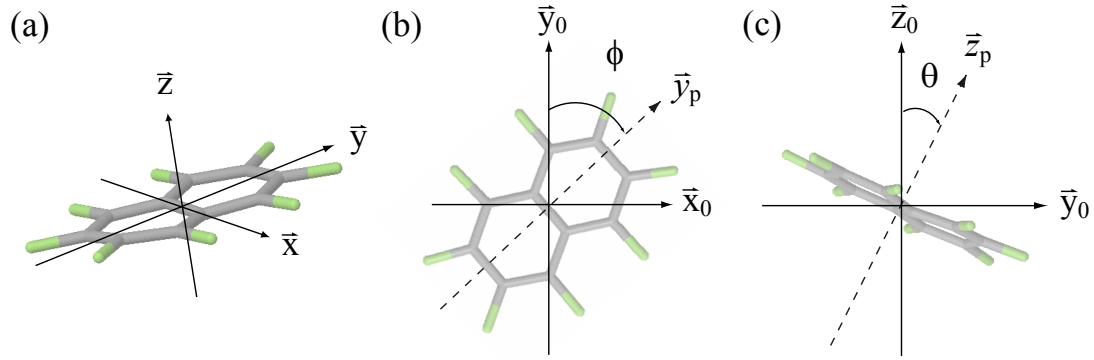

Figure 5.5: Illustration of the molecular frame used to define the orientation of each octafluoronaphthalene molecule in the simulation. (a) The three orthogonal axes are defined in terms of the atomic positions in the molecule, and the orientation of the molecule at a given instant defined using the orientation of this frame relative to the average starting positions ($\vec{x}_0$, $\vec{y}_0$, $\vec{z}_0$) of all the molecules in the simulation (b and c).

calculated with respect to the starting frame,

$$\phi = \arccos(\vec{y}_0 \cdot \vec{y}_\mathrm{p}), \tag{5.5}$$

$$\theta = \arccos(\vec{z}_0 \cdot \vec{z}_\mathrm{p}), \tag{5.6}$$

where each of the vectors is normalised. This scheme is illustrated in Figures 5.5(b) and (c).

These angle definitions were used to study the dynamical behaviour of the molecules in the I-OFN simulation run at 290 K, the same temperature that the single crystal XRD measurements were taken at. Figure 5.6 shows the evolution of the ϕ polar angle during the course of the simulation for one selected octafluoronaphthalene molecule. The molecule is seen to jump between four distinct orientations, each separated by approximately 40°. The two positions most commonly occupied, at $\phi \approx 20°$ and $-20°$, correspond exactly to the positions used to model the X-ray diffraction data, and the fast hopping between them proves that the disorder is dynamic in nature. The two further positions are much more rarely occupied (in fact the molecule selected was the only one that sampled both of these extreme positions during the course of the 100 ns of simulation) but still correspond to energy minima in the phase space spanning ϕ. These orientations are illustrated in Figure 5.7(b), but are so rarely occupied that they

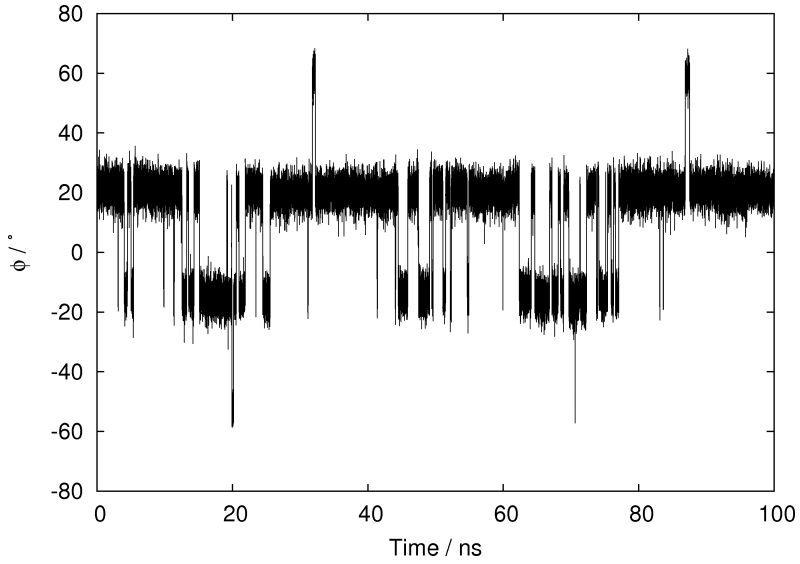

Figure 5.6: Time evolution of the ϕ polar angle for a selected octafluoronaphthalene molecule during the course of the 290 K simulation, showing jumps between four distinct orientations.

would have negligible effect on the Bragg scattering and would not be detected in the XRD studies.

Statistics for the orientations of all of the molecules during the course of the simulation were collected into a histogram, $N(\phi, \theta)$. The relative energy of the different orientations at this temperature could then be calculated as the Boltzmann inversion of this histogram,

$$E(\phi, \theta) = -RT \ln[N(\phi, \theta)], \tag{5.7}$$

and is shown in Figure 5.7(a). It is clear from the energy landscape that the dynamics of the molecules is characterised mainly by the in-plane rotation, ϕ, although the molecule does tilt slightly out of the plane, and the minimum energy pathway through all four positions, marked by a dotted line on Figure 5.7(a) and recreated in Figure 5.7(b), does involve a tilt of the molecule as well as a rotation. The region of Figure 5.7(b) around the two lowest energy orientations, labeled B and C, is well sampled, giving the activation barrier for the jump between the two sites as $\approx$14 kJ mol^{-1} with a rate, k, at 290 K of approximately 0.56 ns^{-1}. This corresponds to a correlation time

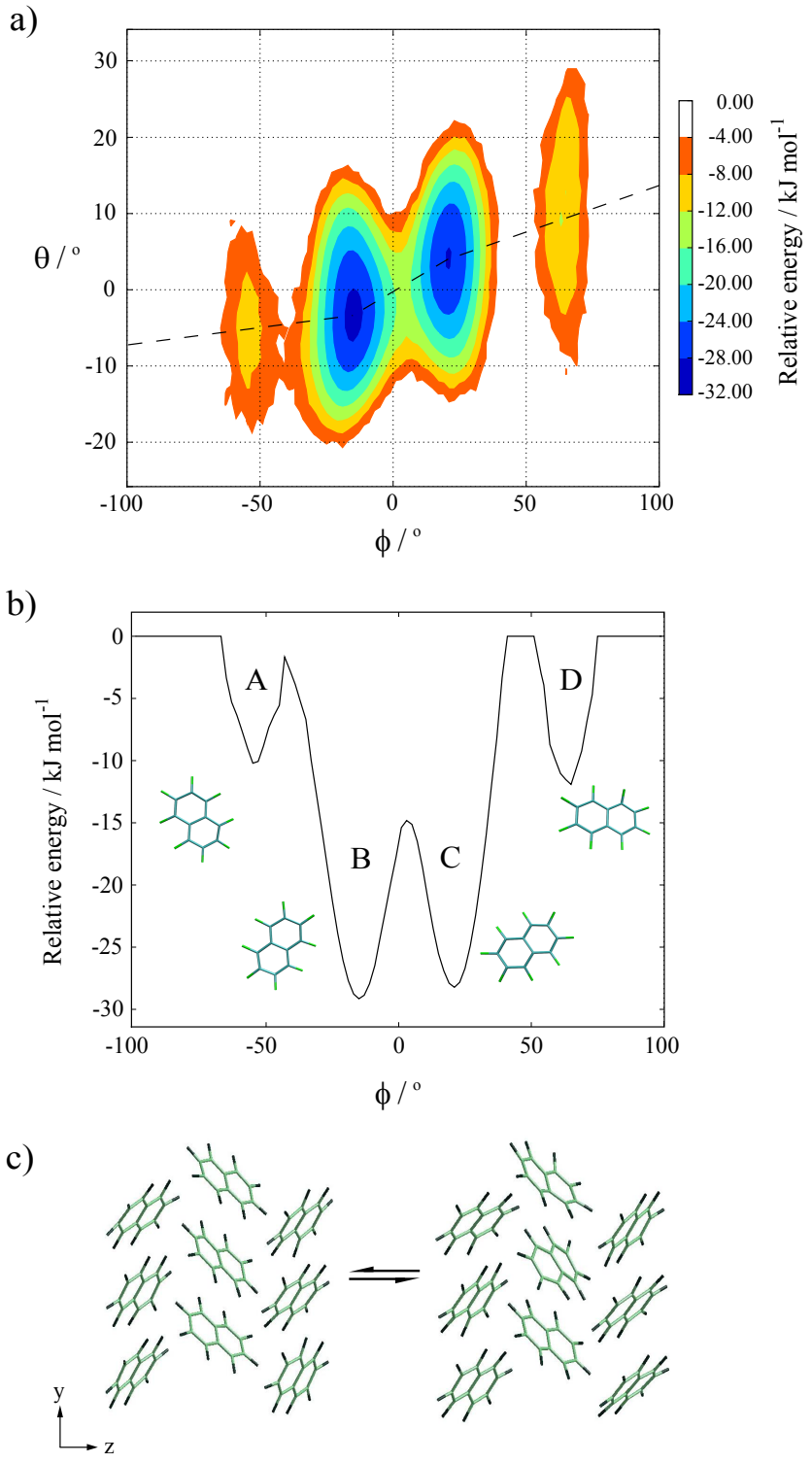

Figure 5.7: (a) Potential energy surface of octafluoronaphthalene as a function of molecular orientation, defined in terms of the polar angles ϕ and θ. The relative energies are calculated from the Boltzmann distributions of the different states combined over all the time steps and all the molecules in the simulation (with histogram bin widths of 2°). (b) Slice through the lowest energy pathway between the four stable positions, indicated by the dashed line. (c) An example of a molecule reorienting within its local crystal structure; the molecule at the centre of the figure is seen to rotate by approximately 40°.

$\tau = 1/2k = 0.89$ ns, which compares well with a value of 0.4 ns at 290 K predicted from the Arrhenius parameters derived from the NMR study.

It is worth noting that the MD results show the barriers for the jumps between B and C to be asymmetric, with the barrier height on going from B→C slightly larger, by approximately 1.5 kJ mol^{-1}, compared to that for the jump in the opposite direction. Accordingly, the relative populations of the two sites are slightly skewed, the system showing a slight preference for orientation B. This agrees well with the fitting used in the XRD, where the populations of the two orientations were weighted by a ratio of 55:45. The energy difference seen by the MD is small, and yet significant because of the extent of the sampling in this region. It represents the average behaviour of the system, which is why it is appropriate to compare it to the XRD results, but it does not describe the behaviour of individual molecules, which are affected by correlations with their neighbours, as discussed below.

The high energy orientations are sampled less well, only allowing us to deduce a lower limit for the barriers from B→A and C→D, of about 27 kJ mol^{-1}. The energy barriers for the jumps back out of these sites are much lower, around 8–12 kJ mol^{-1}, which partly explains why the states are so poorly sampled; if the trajectory of a molecule does jump into one of these positions, it jumps back out again a lot more quickly, as is seen in Figure 5.6, leading to a poor sampling of the phase space in those regions. This is also a signal that the simulations are simply not long enough to probe such high energy processes. This is the case even after taking averages over all of the molecules in the simulation (taking advantage of the fact that they are crystallographically equivalent as the crystal structure has half a molecule in the asymmetric unit cell), for the full 100 ns simulation time, effectively allowing dynamics of a single molecule to be observed for just over 14.4 μs. This is a good illustration of the fundamental limitation in the ability of MD simulation to study high energy processes; the problem of sampling scales exponentially with the energy of the state that is to be sampled and yet the standard solution of increasing the system size or simulating for longer time periods only produces a linear gain.

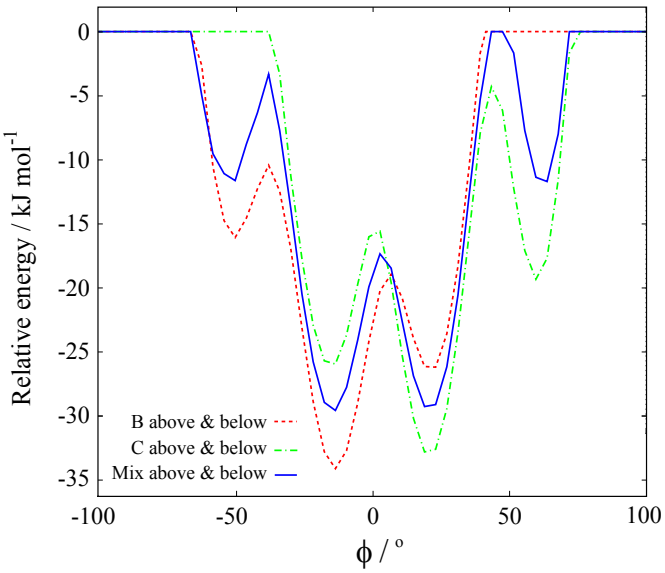

Figure 5.8: Pseudo-potential for octafluoronaphthalene orientation as Figure 5.7, but determined from statistics collected separately for different combinations of neighboring group orientation.

5.4.2.2 Correlated motion

The MD simulation can be used to investigate features of a system that would be very difficult to access experimentally. One such feature that is of interest here is the existence of correlations between the orientations of neighbouring molecules. To investigate this, statistics for the orientations of the molecules were collected into different histograms depending on the local environment of the molecule at that instant. Three separate cases were distinguished; either the immediate neighbours to the molecule were both in a site corresponding to position B, both in position C, or one in C and one in B (i.e. mixed). Only the neighbours along the direction of the stacks were considered (corresponding to the y-direction of the crystal lattice - see Figure 5.7(c)). The interactions between the molecules in this direction are caused by the overlap of the fluorine atoms with the neighbouring molecules' π-systems, making the orientations of the neighbours in this crystal direction more susceptible to correlations than is in the case in the other directions.

The results, shown in Figure 5.8, indicate that the motion of the molecules is cor-

related. Most obviously, the depth of the minima at positions B and C are modified when the neighbouring molecules change their position. The most stable states occur when the neighbours occupy the same position, and when this does happen, the energy barriers for the jumps to other orientations are increased, making the motion less likely. In fact, the increasing barrier height results in the disappearance of the well for site A when the neighbouring molecules are both in position C, and similarly the disappearance of well D when the neighbours occupy position B. These combinations of positions are not sampled at all during the simulation. This is again a consequence of insufficient sampling, as simulations at artificially high temperatures (390 K, above the sublimation point) show that all four orientations are still accessible for any given molecule, i.e. the dynamics are modified, but not fundamentally changed by the effects of correlation. It is important to bear in mind that the periodic boundary conditions may interact with the length scale/periodicity of the correlation, but since the modification to the energies even for the nearest neighbors is quite small (approximately ± 4 kJ mol^{-1}), the effects of the periodic boundary conditions are expected to be negligible.

Accessing information about these correlations experimentally would be very difficult, firstly because the effects are quite small, and secondly because the states associated with the different combinations of correlated orientations do not result in a significantly different environment for the molecules.

5.4.2.3 Phase behaviour

The simulations also clarify the relationship between the I and III phases. Figure 5.9 compares the overall radial distribution functions, $g(r)$, between all the fluorine atoms for the three simulations. This is a convenient means of comparing the different structures, particularly as the unit cells of the I and III phases are not trivially related, meaning that the atomic coordinates from the simulation boxes cannot be simply overlaid. The three functions share the same basic structure, confirming that the crystal structures are very similar. The lower symmetry, low temperature structure has, as expected, a slightly more structured distribution function, particularly at longer distance. However, on warming this phase, the $g(r)$ changes, most notably at around $r = 3.5$ Å and above 8 Å, and becomes indistinguishable from that of Form I. It is

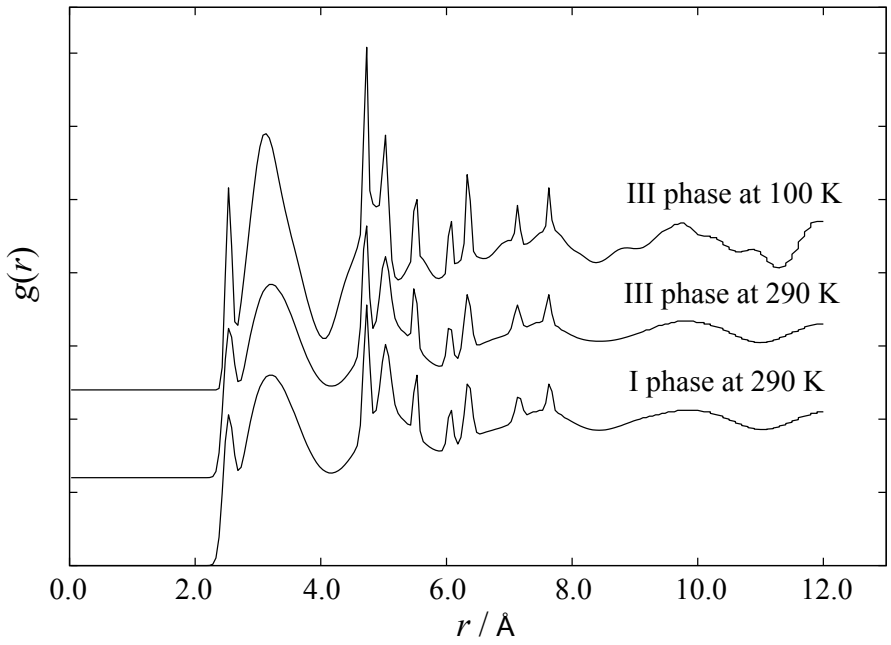

Figure 5.9: Fluorine radial distribution functions derived from simulations of I-OFN at 290 K, and III-OFN at both 100 K and 290 K. The *g(r)* for the form III simulations are vertically shifted for clarity.

reasonable to assume that this change is a consequence of the onset of dynamics in the molecules, which is also observed in the simulation.

Overall, this simple test from the MD simulations lends significant insight into the nature of this phase transition. At high temperatures the molecules are dynamic, hopping between the four wells in Figure 5.7(b), which leads to a high degree of symmetry in the resolved X-ray structure because the time averaged orientations of all the molecules become equal. As the structure is cooled, the dynamic processes slow down, and are eventually frozen out, presumably around the temperature of the phase transition at ≈266.5 K. The correlations between the molecules explains why the structure of III-OFN contains alternating stacks with molecules exclusively in orientation B *or* C; this highly ordered configuration is more favourable than one with randomly oriented, static molecules. All of this evidence suggests that the conversion from I-OFN to III-OFN is an order-disorder, second order phase transition.

5.4.3 Differential scanning calorimetry

Figure 5.10 confirms the non-trivial nature of the low temperature phase behavior. A series of sharp events are observed in the DSC thermogram on cooling between 260 K and 240 K, while the corresponding endothermic event occurs at a significantly higher temperature (almost 290 K) and is well behaved. These discontinuities are indicative of a first order phase transition, and must therefore correspond to the transition from I-OFN to II-OFN. The sharp events on cooling correspond to 'crepitation' i.e. sudden transformation of individual crystallites. Crepitation is atypical for molecular solids, as is the extremely wide temperature range over which these events occur and the large hysteresis between the heating and cooling events: to the best of our knowledge there are no examples in the literature. This behaviour was confirmed by polarizing microscopy; on cooling a sample on a cold stage, individual crystallites transformed abruptly over a range of temperatures that mirrored the DSC results. Snapshots taken during the cooling cycle are shown in Figure 5.11. The microscopy shows that the crystallites shatter as they transform on cooling, scattering the incident light so that they become opaque. This same phenomenon was also seen in DSC experiments in which a single sample was put through multiple cooling/heating cycles; whilst the

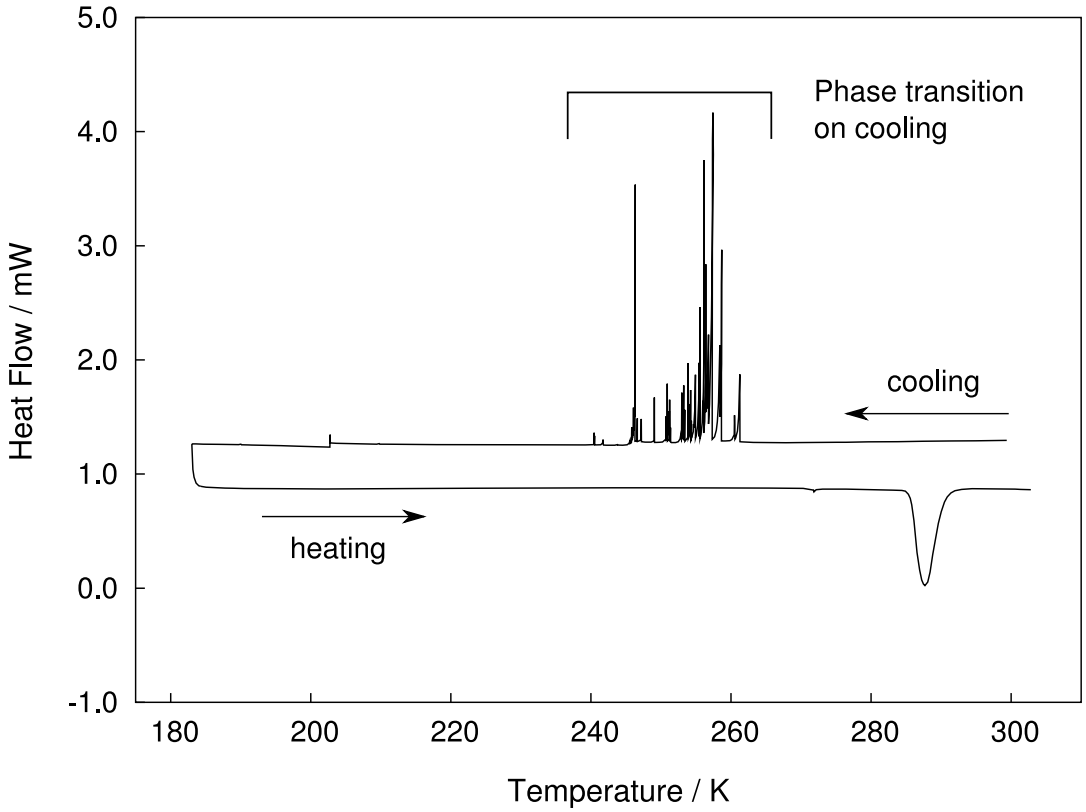

Figure 5.10: DSC results for OFN, in a cycle starting at the room temperature form and cooling through the transition before heating again. Both cooling and heating were performed at a rate of 0.5 K/min.

character of the phase transition on heating remained constant for successive heating cycles, more numerous but less intense events were observed on cooling. This was tested for a series of 5 cycles, during which the temperature range of the transitions remained wide and approximately unchanged.

The unpredictable NMR results at low temperatures can be explained entirely by the complicated phase behaviour seen by the DSC and microscopy measurements. The level of complication renders the possibility of obtaining useful NMR measurements in the region of the phase transition completely untenable. This does not have a significant impact on the relaxation measurements because a sufficient range of temperatures above that of the phase transition could be explored. It is possible that a stable, low temperature sample of the compound could be obtained by first cooling it well below the phase transition, and conducting experiments on the sample as it is heated. This would not only be difficult to do experimentally for the temperature range required, but would yield results of limited value in terms of the relaxation measurements.

5.5 Discussion

The fitting of the variable temperature T_1 relaxation data reveals that a fast dynamic process, with a time constant of approximately 0.4 ns at 290 K, drives this form of relaxation. The MD simulation shows up a process on a similar timescale, with $\tau \approx 0.9$ ns at 290 K, corresponding to a small-angle hop of each molecule between positions related by an in-plane rotation of 40°. The activation barriers measured by each technique, for what would appear to be the same process, also compare favourably, with an E_a of 20.6 ± 0.4 kJ mol^{-1} from the NMR and the Gibbs free energy of activation for the process of $\Delta G^{\ddagger} \approx 14$ kJ mol^{-1} from the MD. An exact match of these quantities is not expected, firstly because the precise value from the MD will depend on the exact force field parameterisation, and secondly because the two quantities are subtly different; the activation barrier from the MD is specific to the temperature of the simulation so incorporates both the entropy and enthalpy components, whereas the barrier from the NMR is really just an empirical quantity. The molecular orientations that the MD sees the molecule jumping between for this process are identical to the two disordered

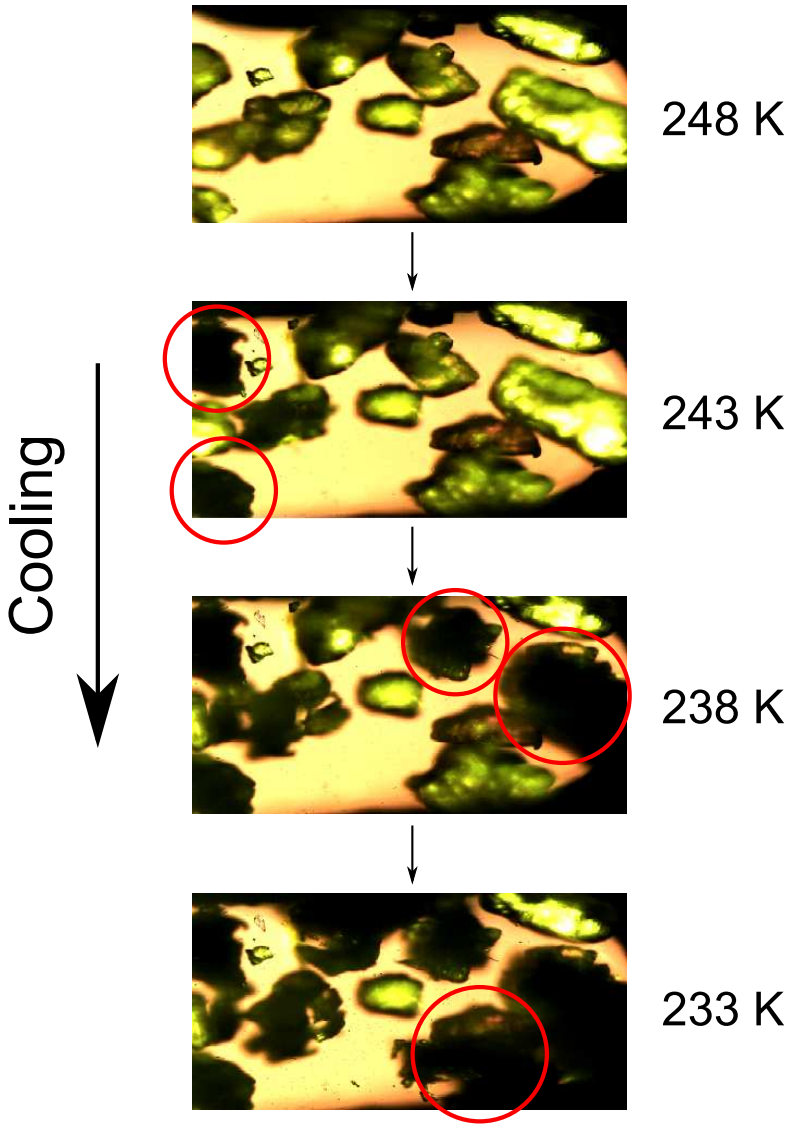

Figure 5.11: Images taken from an optical microscope observing OFN on cooling with a polarised light source. The crystallites circled in red have undergone the phase transition, which is accompanied by the crystal shattering, and thus becoming opaque. The transitions occur over a temperature range of approximately 15 K, similar to that seen in the DSC.

orientations of the molecules proposed in the X-ray work, validating the MD results, and proving almost unequivocally that the disorder they saw is dynamic in nature.

At first it seems that, as in the case of the T_1 results, the MD presents a good candidate process for the motion affecting the $T_{1\rho}$ relaxation; the microsecond timescale of the jump into the rare positions (from positions B→A and C→D in Figure 5.7(b)) is of the correct order to drive the relaxation. However, the asymmetric nature of the jumps and general complication of the exchange model require a more thorough analysis if they are to be understood completely. The MD results provide an initial model on which the relaxation theory can be based, although that four site model is first simplified by assuming it is symmetric so that,

$$k_{\text{in}} = k_{\text{BA}} = k_{\text{CD}} \tag{5.8}$$

$$k_{\text{out}} = k_{\text{AB}} = k_{\text{DC}} \tag{5.9}$$

$$k_{\text{f}} = k_{\text{BC}} = k_{\text{CB}}, \tag{5.10}$$

where k_{AB} signifies the rate of the jump from site A to site B. This model allows the difference in the magnitude of the rates, $k_{\text{in}} \gg k_{\text{out}}, k_{\text{f}}$ to be preserved.

An exchange matrix, $\tilde{\boldsymbol{R}}$, is constructed with the rate information for each site encoded into a single row/column (hence for an n site jump, $\tilde{\boldsymbol{R}}$ is an n x n matrix), according to the rules [116, 117],

$$R_{jl} = k_{lj},\ j \neq l \tag{5.11}$$

$$R_{jj} = -\sum_{l \neq j} R_{jl}. \tag{5.12}$$

For the four site jump model proposed for the motion in octafluoronaphthalene this

construction yields the following expression for the exchange matrix,

$$\tilde{\boldsymbol{R}} = \begin{pmatrix} -k_{\text{out}} & k_{\text{in}} & & \\ k_{\text{out}} & -k_{\text{in}} - k_{\text{f}} & k_f & \\ & k_f & -k_{\text{in}} - k_{\text{f}} & k_{\text{out}} \\ & & k_{\text{in}} & -k_{\text{out}} \end{pmatrix}, \tag{5.13}$$

where rows and columns 1–4 correspond to sites A–D.

The eigenvalues λ_n, and eigenvectors of $\tilde{\boldsymbol{R}}$, describe the rates and their relative importance. For an n x n matrix there are $n-1$ non-zero eigenvalues. The effective correlation function becomes [116],

$$C(t) = \sum_{n=0}^{N-1} A_n \exp(-\lambda_n t), \tag{5.14}$$

where the A_n constants incorporate information about the specific orientations of each site and their relative populations. In the current study these constants are effectively integrated into the constants used in the fitting procedure, as only trends in the activation barriers are observed.

In the 4-site model presented thus far, the three non-zero eigenvalues are $2k_{\text{f}} + \frac{k_{\text{in}}}{2}$, $k_{\text{out}} + \frac{k_{\text{in}}}{2}$ and $-k_{\text{in}} - k_{\text{out}}$. For the model to contain a rate component that can interact with $T_{1\rho}$, the corresponding time constant (given as the inverse of λ_n) for at least one of the eigenvalues *must* be on the μs timescale. However, given that $k_{\text{in}} \gg k_{\text{out}}, k_{\text{f}}$, it is clear that each of the three eigenvalues will be dominated by one or other of the faster rates, so that none can interact on the microsecond timescale. This is an interesting result, similar to the asymmetric two site exchange discussed by [116], where the NMR relaxation is only sensitive to the faster jump. However, it also means that the 4-site model proposed here cannot explain the $T_{1\rho}$ results.

As discussed in the Introduction, early NMR work [105] had suggested that the octafluoronaphthalene molecules might undergo 180° jumps about an axis perpendicular to the molecular plane. Such a rotation appears physically unrealistic, particularly when other motions, e.g., jumps about the long molecular axis, would be expected to involve lower energy barriers. The MD results, however, provide a plausible mechanism

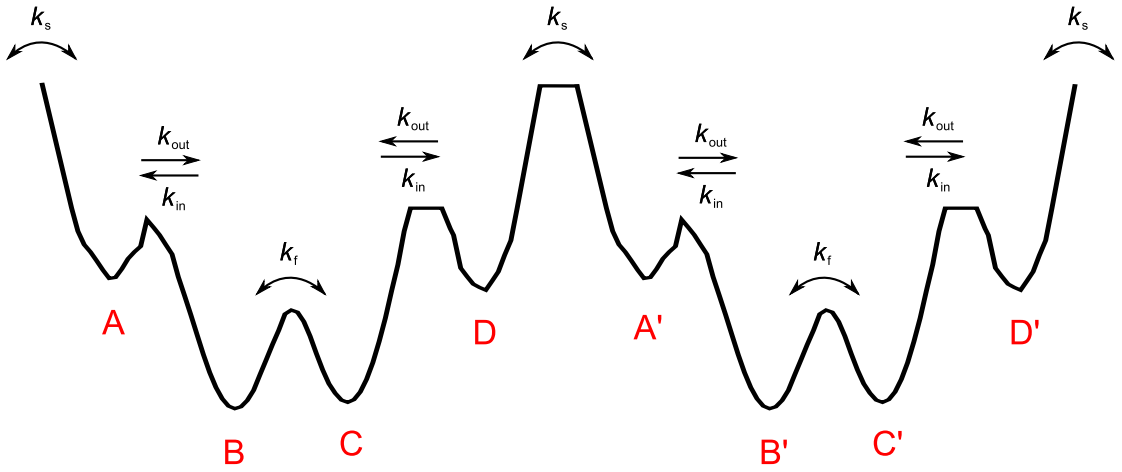

Figure 5.12: A schematic of the 8-site exchange model that includes the full rotation of the molecules (A↔D´ or A´↔D), and the rates associated with each jump process.

for such a rotation via the rarely occupied sites. Recognizing that there are corresponding sets of four orientations related by inversion symmetry (say A´–D´), then only a further rotation of 60° is required to take a molecule from one extreme orientation to another, A↔D´ or A´↔D, as illustrated in Figure 5.12. The rate for this process, labeled k_{s}, is expected to be very slow and the barrier height accordingly large, as this jump motion was not sampled by the MD simulation at all.

This model produces an 8 x 8 exchange matrix,

$$\tilde{\boldsymbol{R}} = \begin{pmatrix} -k_{\mathrm{s}} - k_{\mathrm{out}} & k_{\mathrm{in}} & & & & & & k_{\mathrm{s}} \\ k_{\mathrm{out}} & -k_{\mathrm{in}} - k_{\mathrm{f}} & k_{\mathrm{f}} & & & & & \\ & k_{\mathrm{f}} & -k_{\mathrm{in}} - k_{\mathrm{f}} & k_{\mathrm{out}} & & & & \\ & & k_{\mathrm{in}} & -k_{\mathrm{s}} - k_{\mathrm{out}} & k_{\mathrm{s}} & & & \\ & & & k_{\mathrm{s}} & -k_{\mathrm{s}} - k_{\mathrm{out}} & k_{\mathrm{in}} & & \\ & & & & k_{\mathrm{out}} & -k_{\mathrm{in}} - k_{\mathrm{f}} & k_{\mathrm{f}} & \\ & & & & & k_{\mathrm{f}} & -k_{\mathrm{in}} - k_{\mathrm{f}} & k_{\mathrm{out}} \\ k_{\mathrm{s}} & & & & & & k_{\mathrm{in}} & -k_{\mathrm{s}} - k_{\mathrm{out}} \end{pmatrix}, \tag{5.15}$$

with seven non-zero eigenvalues. These seven contain one eigenvalue consisting of only slow rate constants, at $-k_{\mathrm{s}} - k_{\mathrm{in}}/2$, and thus the model can explain the interference with the $T_{1\rho}$ relaxation. Although the full rotation was not observed in the ambient temperature MD simulation, the success of the 8-site model to fully describe both of the NMR relaxation processes provided motivation to undertake simulations at higher temperatures to improve the sampling rate and try to see the full rotation. Indeed, a simulation at 390 K (well above the sublimation point) did sample the full rotation of

a few of the octafluoronaphthalene molecules, following the multiple-jump mechanism described in the above models. However, extracting accurate rates for the individual jumps was still not possible even in the high temperature simulation, because the rotations are still not amply sampled. Even if accurate estimates could be obtained and used to calculate appropriate values for the seven eigenvalues of the exchange matrix, linking those eigenvalues to the experimental NMR results would be unfeasible because there are still too many unknown parameters in the model and insufficient experimental data to fit them to.

5.6 Conclusion

The dynamics of the constituent molecules in solid octafluoronaphthalene has been investigated using solid-state NMR and MD simulation, and the highly complementary nature of the techniques has been demonstrated. The NMR provides a direct, robust measure of the kinetic parameters describing the different molecular motions displayed by the compound, showing two distinct motional processes to be present in OFN, on the ns and μs timescales. However, these measurements do not provide information on the form of the motions themselves. For this, however, MD simulation is perfect, and it was used to straightforwardly link the fast, ns process to jumps of $\approx 40^\circ$ between two orientations of the molecules. By combining the sampling statistics for all the molecules in the simulation cell, a candidate motion was also found for the rarer process occurring on a μs timescale: some molecules in the simulation were observed to undergo a rare, further jump of 40° either side of the two main orientations. The 4-site model proposed by the MD was compared directly to the NMR results using relaxation theory. However, this analysis showed that the rates that drive the relaxation are all dominated by the faster rates in the model.

The only way to reconcile the results was to allow the full rotation of the molecules; introducing a further four sites related to the original four by a 180° rotation. The resulting 8-site jump model produced rates that could explain all of the relaxation behaviour, also supporting previous experimental evidence from both XRD, which concluded that the molecules were disordered between two orientations differing by a

rotation of ≈40°, and early NMR work, which postulated the full C_2 rotation of the molecules. Simulations at artificially high temperatures later confirmed this model, showing the extra molecular orientations to provide a stepped mechanism that enables the full rotation of the molecules.

The MD simulations were also used to investigate the existence of correlations between the orientations of neighbouring molecules, showing that such correlations do exist, meaning that neighbouring molecules prefer to align. This preference is only very slight at the temperature studied (290 K). It is postulated that as the temperature of the system drops, eventually this preference becomes stronger until entire stacks of the molecules preferentially align and the compound undergoes an order-disorder, second-order phase transition from the disordered I-OFN phase to the low temperature, ordered III-OFN phase. MD analysis of the two phases also shows that the long range structure of III-OFN matches precisely with the structure of I-OFN when it is simulated at the same temperature (above the phase transition).

The phase behaviour of OFN was also investigated further using DSC and polarized microscopy to observe the unusual temperature dependence of the transitions. The evidence suggests that the temperature of the first order transition from I-OFN to II-OFN is highly dependent on the specific crystal environment, so much so that individual crystallites can transform at very different temperatures, over a range of approximately 20 K. The reason for this behaviour is unknown.

The dynamics in this system, and the effectiveness of MD and NMR in being able to completely characterise it, are particularly interesting in light of the continued interest in the development of molecular machines [118, 119]. OFN is not itself a good candidate for such systems because the energy barriers for the jump processes are too large, while the correlation of the molecular orientations is probably too weak to be useful. However, the forms of the motion are similar to those required in molecular machines, and the full characterisation of the system described here does highlight the importance of considering even the slowest degrees of freedom, as they can lead to new phenomena that can fundamentally change the way a system behaves (cf. the small molecular jumps which provide the mechanism for the full rotation of the molecules). Understanding and characterising correlated motions, which MD simulation is almost

uniquely suited to investigating, is a critical step in the goal of creating molecular machines [21, 120].

Acknowledgements

Dr. Sebastian Palucha is thanked for setting up the MD simulations on octafluoronaphthalene. Samples purified by vacuum sublimations were provided by Dr. Jonathan C. Collings.

Chapter 6

Exploring the free energy profile of rigid body rotations using metadynamics

6.1 Introduction

The problem of sampling high energy states in Molecular Dynamics simulations is well documented, and stems from the fact that the probability of the system trajectory visiting a given point, α, in phase space, is proportional to the Boltzmann factor, $\exp(-\beta E_\alpha)$, of that state. Although high energy states make negligible contributions to the underlying partition function of the whole system, sampling them well is crucially important when investigating rare events that involve the crossing of high energy barriers. So severe is the problem, that many techniques have been introduced to enhance the sampling in MD. Metadynamics, proposed by Parrinello et al. in 2002 [42], is one such method.

Metadynamics is a close descendant of umbrella sampling (see Section 2.6.1). In umbrella sampling, a potential is added in to the system Hamiltonian that is designed to bias the system trajectory along a certain pathway so as to overcome the energy barriers along that path. In metadynamics, the potential, $V_{\mathrm{b}}(s_\alpha, t)$, doesn't have to be decided upon a priori, but is built up over time by adding small, Gaussian shaped, repulsive markers centred at positions that the trajectory of the system has already visited. As

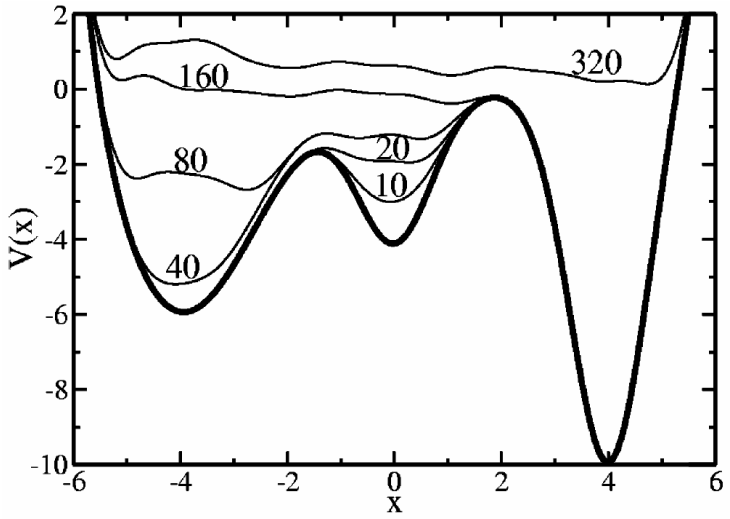

Figure 6.1: Filling a 1D model potential with hills, starting in the middle well. After 20 hills, the system escapes to the well on the left and so forth. Reproduced from ref. [42].

more markers are added, V_b compensates for the underlying potential by effectively filling up the wells and pushing the system over barriers to explore new regions of the space spanning the predefined set of collective variables (CVs), s_α, that are chosen to be characteristic of the event that is to be accelerated. That is the free energy, $F_\mathrm{G}(s_\alpha) = -V_\mathrm{b}(s_\alpha, t \to \infty) + C$, where C is a constant offset that accounts for overfilling of the wells. This ability to directly evaluate the underlying free energy surface is the reason why the method has become popular very quickly, but also because it is a very robust method, as the collective variables can take the form of any quantity that can be calculated from the system coordinates: from positions, angles and distances to coordination numbers, order parameters, and even normal modes of large biological molecules. In theory there is no limit on the number of collective variables that can be explored, although in practice, as the space becomes more complicated, obtaining an accurate reconstruction of the potential energy surface becomes more difficult.

Metadynamics has found applications in a wide range of systems, leading to insights into processes that were previously either not possible, or extremely difficult to simulate. The first implementation of metadynamics, in keeping with the original authors' backgrounds, was in the Car-Parrinello Molecular Dynamics code [31], which is an efficient *ab initio* MD method. Consequently, there have been many ap-

plications of metadynamics to systems uniquely suited to *ab initio* methods; inter- or intra-molecular reactions or conformational changes that require bonds to be made or broken. The requirement for enhanced sampling in these systems is a consequence not only of the large energy barriers that need to be overcome, but also of the fact that smaller subsets of phase space are accessible to *ab initio* methods because of the increased computational load and smaller time step that is required (approximately a factor of 10x smaller than in normal MD) to integrate the equations of motion of the electronic degrees of freedom.

Applications of the algorithm in these areas have been used to successfully recreate complicated free energy surfaces for the reactions of simple molecules [121–124]. Surface reactions have also been investigated, from studying adsorption/desorption processes [125, 126] to calculating free energy profiles for surface catalysed reactions [127]. Recently, metadynamics has also been used to explore different configurations of a gold nano cluster [128], uncovering new arrangements of conformations that would not be accessible to normal CPMD simulations. The collective variable of choice in all of these simulations has been a form of 'coordination number' between individual or groups of atoms, a quantity that essentially gives a continuous functional form to the critical interaction distances. There have also been multiple studies exploring conformational changes in many molecules [42, 129–131].

A key area where metadynamics has already, and will continue, to have a large impact is in the simulation of biomolecular systems. These have traditionally been extremely challenging to simulate not only because they are typically very large, but also because the processes of interest are very rare events, usually occurring on mesoscopic time scales of microseconds or longer [132]. This challenge is coupled with enormous reward; understanding the underlying molecular mechanisms responsible for biological processes would have considerable implications for future drug development (one can immediately see the importance of this subject area when considering the scope and ambition of projects like Folding@Home [133]). Although there have been many successful applications of the metadynamics method into bio simulation, such as in the simulation of small protein folding [134–136] and ion gating mechanisms in membrane protein channels [12, 137], one recent success stands out. This is the study by Prakash

et al. [138] in the description of the conformational changes in the dengue virus envelope protein in response to the pH of its local environment. Metadynamics was used to demonstrate a possible mechanism by which local pH destabilises certain conformations of the protein, a key interaction during the invasion of a host cell. Crucially, the mechanism involves a previously unknown intermediate state that could be targeted by a new generation of drug molecules. Crucial to the current discussion of the utility of metadynamics, the method used here is quite general, employing an initial CV space to push the protein conformation away from that of the starting structure to find the likely reaction pathway, then using a specific CV to map out the energy surface for that particular path. A similar stepwise approach that looks for general mechanisms then explores them explicitly has also been used elsewhere, although in these cases the path of interest was mapped out using umbrella sampling with the initial metadynamics estimate of the free energy as the biasing potential [122, 136]. These are promising approaches to increasing the generality of these techniques, making them more applicable to systems that are not well understood.

The versatility of the metadynamics algorithm has been demonstrated by an extremely wide range of applications, and it is thanks to the vast array of possible collective variables that can be used. For instance, structural order parameters can be used as collective variables [139–141], or even the dimensions of a simulation box [142–144] can be used to induce phase transitions between different condensed phases: a difficult problem to study using normal MD methods. Spiwok et al. also used an interesting set of collective variables to explore molecular conformations [130]; they conducted principle component analysis on a short simulation to extract the essential dynamics of a small biological molecule then exploited these degrees of freedom as CVs in metadynamics, obtaining a free energy map showing the preferred conformations.

In this Chapter, metadynamics is used to force the rotation of a rigid molecule. Octafluoronaphthalene (OFN) is studied, partly as a relatively simple test case, but also to answer outstanding questions left by the inability of normal MD simulation to fully sample the molecular orientations and their correlated motions. As discussed in Chapter 5, OFN, with its fixed crystal structure but mobile molecular units, resembles one of the many crystalline molecular machines [145, 146] that are being studied and

developed as part of the drive to mimic nature in engineering machines that work on the molecular level. Molecular components whose motions are correlated are vital in such machines, as are the abilities to characterise and understand the underlying processes.

6.2 Theory

The metadynamics algorithm introduces a time dependent bias potential, $V_{\mathrm{b}}(\boldsymbol{s}, t)$ (where the quantity $\boldsymbol{s}$ refers to the vector of collective variables, s_α), that is used to influence and accelerate the dynamics in a predefined set of collective variables that can be calculated from a subset of the particle positions, $\boldsymbol{R}(\boldsymbol{r}^N)$. This concept was first introduced using the extended Lagrangian formalism which is used to describe the electronic degrees of freedom in the Carr-Parrinello *ab initio* MD method [42],

$$\mathcal{L}_{\mathrm{sys}} = \mathcal{L}_{\mathrm{MD}} + \frac{1}{2}\sum_\alpha m_\alpha \dot{s}_\alpha^2 - \frac{1}{2}\sum_\alpha k_\alpha (s_\alpha - S_\alpha(\boldsymbol{R}))^2 + V_{\mathrm{b}}(\boldsymbol{s}, t), \tag{6.1}$$

where the biasing potential is included in the Lagrangian of the system, and the collective variables are treated as fictitious particles of mass m_α, with positions s_α, tethered to their instantaneous positions, $S_\alpha(\boldsymbol{R})$, by a spring with force constant k_α. The other two new terms in Equation 6.1 represent the kinetic and potential energies of the particles, which roll around in the minima of the free energy landscape spanning the collective variable space and are slowly pushed into new areas as the minima are filled by the biasing potential.

The separation between the fictitious particles mentioned above and the positions of the collective variables themselves is not strictly required [147, 148]. In this case $m_\alpha \to 0$, $k_\alpha \to \infty$ and hence $s_\alpha \to S_\alpha(\boldsymbol{R})$, so that the biasing potential acts directly on the atomic coordinates, leading to only a slight modification to the force acting on the system,

$$\begin{aligned} \boldsymbol{f}(\boldsymbol{R}) &= -\frac{d}{d\boldsymbol{R}}(V_{\mathrm{MD}}(\boldsymbol{R}) + V_{\mathrm{b}}(\boldsymbol{s}, t)), & (6.2)\\ &= \boldsymbol{f}_{\mathrm{MD}} - \frac{dV_{\mathrm{b}}(\boldsymbol{s}, t)}{dS(\boldsymbol{R})}\frac{dS(\boldsymbol{R})}{d\boldsymbol{R}}, & (6.3) \end{aligned}$$

$V_{\mathrm{b}}(\boldsymbol{s},t)$ takes on the form of a sum of Gaussian markers, with width δs and height w, centred at the values of the collective variable that have already been visited by the trajectory of the system and deposited at a time interval τ_{G};

$$V_{\mathrm{b}}(\boldsymbol{s},t) = w \sum_{t=\tau_{\mathrm{G}},2\tau_{\mathrm{G}}..} \exp\left(-\frac{|\boldsymbol{s}-\boldsymbol{s}(t)|^2}{2\delta s^2}\right). \tag{6.4}$$

As mentioned previously, this potential serves to fill up the wells in the potential energy surface of the CVs. As the underlying potential is compensated for, the system escapes from local minima and can fully sample the energy surface. Once all of the states have been explored and all the wells filled, the biasing potential becomes a good estimate for the underlying free energy surface, $F_{\mathrm{G}}(\boldsymbol{s}) = -V_{\mathrm{b}}(\boldsymbol{s}, t \to \infty)$.

The only modification to the normal equations of motion comes in the form of the second term on the right hand side of Equation 6.3. Firstly, the derivative of the biasing potential is needed, but is relatively facile in terms of programming because it is just a sum of the derivatives of the Gaussian markers that have already been added:

$$\frac{dV_{\mathrm{b}}(\boldsymbol{s},t)}{d\boldsymbol{s}} = -\frac{w}{\delta s^2} \sum_{\tau_{\mathrm{G}},2\tau_{\mathrm{G}}..} (\boldsymbol{s}-\boldsymbol{s}(t)) \exp\left(-\frac{|\boldsymbol{s}-\boldsymbol{s}(t)|^2}{2\delta s^2}\right), \tag{6.5}$$

and the second derivative required is that of the definition of the collective variable, done with respect to the system coordinates. This term is specific to the collective variable used and gives the direction of the force; the form of this calculation used in the current implementation is given below. The derivative of the Gaussian hills scales the magnitude of the force applied.

6.2.1 Error

Clearly if metadynamics is to be useful in determining unknown free energy profiles, an appreciable approximation of the associated error must also be known. Laio et al. [148] sought to achieve this goal by conducting numerical analysis on a Langevin model including a time-dependent metadynamics term with a variety of different shaped potentials that would be filled. Importantly they proved that the relationship they obtained was appropriate to describe the error in real systems, and, in general, that

it is independent of the shape of the underlying potential. It depends not only on the metadynamics parameters w, δs and τ_{G}, but also on some properties specific to the system:

$$\epsilon = C(d)\sqrt{\frac{S\delta s}{D\tau_{\mathrm{G}}}\frac{w}{\beta}}, \tag{6.6}$$

where S is the size of the CV space, D is the diffusion coefficient of the system in that space, $\frac{1}{\beta} = k_{\mathrm{B}}T$, is a measure of the temperature of the simulation, and $C(d)$ is a dimensionless constant that depends upon the number of CVs used. This error represents the average deviation between the calculated value of the free energy, $F_{\mathrm{G}}(\boldsymbol{s})$, and the correct value of $F(\boldsymbol{s})$.

The dependency on $\sqrt{\frac{w\delta s}{\tau_{\mathrm{G}}}}$ is really on the rate at which the biasing potential is built up to fill the energy minima; the slower this is done the more accurate the results. This relationship is what is intuitively expected, as in the slowest possible limit there is no biasing potential. If the approximate volume of the potential surface that needs to be compensated for is known, the values of w, δs and τ_{G} can be optimised for a given total simulation time to achieve the most accurate results. The other key element in Equation 6.6 is the $\sqrt{\frac{1}{D}}$ dependence, which states that the most accurate results are obtained when the system diffuses quickly through the CV space. This necessitates that good choices are made for the CVs.

The origin of the error discussed above is that the assertion $F_{\mathrm{G}}(\boldsymbol{s}) = -V_{\mathrm{b}}(\boldsymbol{s}, t \to \infty)$ is not quite correct. Once the biasing potential completely compensates for $F(\boldsymbol{s})$, the addition of further Gaussian markers serves to introduce error, so that $-V_{\mathrm{b}}(\boldsymbol{s}, t)$ fluctuates around the correct value of $F(\boldsymbol{s})$. Clearly, the magnitude of the fluctuations depends on the size of the markers added, which explains the presence of w, δs and τ_{G} in Equation 6.6. A few different studies have attempted to control this fluctuation either by making w time dependent [147] or using other methods [136, 149, 150]. However, the most promising attempt was published recently by Barducci et al. [151]. They define a new 'well-tempered', 'smoothly converging' form of metadynamics in which the height of the Gaussian markers added are modified according to the relationship

$$w = \omega e^{-[V_{\mathrm{b}}(\boldsymbol{s},t)/\Delta T]}\tau_{\mathrm{G}}, \tag{6.7}$$

where ω is the bias deposition rate with units of energy per unit time, $V_{\mathrm{b}}(\boldsymbol{s}, t)$ is the estimate of the free energy at the current CV positions and the current time step, and ΔT is a tunable temperature-like parameter that controls how quickly w reduces as the wells are filled. In practice, ΔT also introduces a 'ceiling' to the height of $V_{\mathrm{b}}(\boldsymbol{s}, t)$, which can restrict the trajectory of the CVs to lower energy regions of their phase space. In this scheme, the final value of the biasing potential is a scaled approximation to $F(\boldsymbol{s})$:

$$F(\boldsymbol{s}) = -\frac{T + \Delta T}{\Delta T} V_{\mathrm{b}}(\boldsymbol{s}, t \to \infty). \tag{6.8}$$

At the beginning of a metadynamics run using this methodology, the biasing potential is zero and so $w = \omega$, which can be quite a large value, allowing the wells to be filled quickly, leading to a rapid exploration of phase space. As the wells begin to fill up, w is scaled and progressively smaller perturbations are made to V_{b}, allowing it to smoothly converge to an accurate approximation of $F(\boldsymbol{s})$. The values of ω and ΔT can be chosen to achieve the best efficiency.

6.3 Application: rotating a molecule

The CV explored here is the orientation of a single OFN molecule. To define this, a reference frame was fixed onto the molecule, as per the illustration in Figure 6.2 and the associated caption.

Because the molecule is free to roll and tilt in directions perpendicular to the direction of the in-plane rotation, the projection of the $\boldsymbol{y}$-axis of the molecular frame onto the $\boldsymbol{x}_0\boldsymbol{y}_0$ plane, $\boldsymbol{y}_{\mathrm{p}}$, was used to define the angle of rotation,

$$\boldsymbol{y}_{\mathrm{p}} = \boldsymbol{z}_0 \times (\boldsymbol{y}_{\mathrm{t}} \times \boldsymbol{z}_0), \tag{6.9}$$

so that the effect of these other degrees of freedom could be averaged out. This is the same definition that was used when interpreting the results from the conventional MD simulations (see Chapter 5).

The collective variable is the angle ϕ between $\hat{\boldsymbol{y}}_{\mathrm{p}}$ (where the circumflex denotes a unit vector) at time t and its value at $t = 0$, which is equivalent to the starting vector

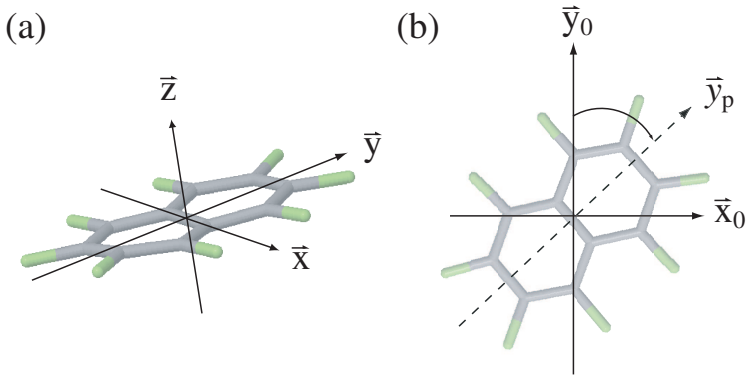

Figure 6.2: The molecular frame used to describe the orientation of the octafluoronaphthalene molecules. (a) The molecular axis, with the origin at the centre of mass of the molecule. Vectors $\boldsymbol{x}$ and $\boldsymbol{y}$ are defined relative to collections of atoms in the molecule and $\boldsymbol{z}$ is their cross product. (b) The definition of the collective variable used, shown as the polar angle ϕ. $\boldsymbol{x}_0$ and $\boldsymbol{y}_0$ refer to the axes at time $t = 0$.

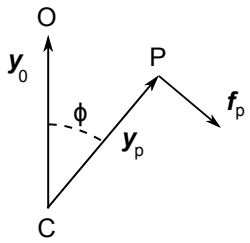

Figure 6.3: Schematic diagram showing the calculated force, $\boldsymbol{f}_{\mathrm{p}}$.

$\hat{\boldsymbol{y}}_0$. The definition of ϕ is thus,

$$\begin{aligned} \cos\phi &= \hat{\boldsymbol{y}}_{\mathrm{p}} \cdot \hat{\boldsymbol{y}}_0 \\ \phi &= \arccos\left(\hat{\boldsymbol{y}}_{\mathrm{p}} \cdot \hat{\boldsymbol{y}}_0\right). \end{aligned} \tag{6.10}$$

This is the same angle definition as a standard valence angle with the vectors $\hat{\boldsymbol{y}}_{\mathrm{p}}$ and $\hat{\boldsymbol{y}}_0$ replacing the usual $\boldsymbol{r}_{\mathrm{ab}}$ and $\boldsymbol{r}_{\mathrm{bc}}$ bond vectors. Figure 6.3 illustrates these similarities and shows the labeling scheme used here.

The force direction is obtained from $-\frac{d\phi}{dr_{\mathrm{l}}^{\alpha}}$, where r_l^{α} is the α component of the vector pointing to atom l. The points C, O and P in Figure 6.3 do not correspond to atomic positions, but are average positions summed across different atomic positions to

define the vectors $\hat{\boldsymbol{y}}_{\mathrm{p}}$ and $\hat{\boldsymbol{y}}_0$. The force due to the metadynamics potential must only rotate the molecule, giving a net force of zero so that there is no component acting on the centre of mass of the molecule. The point O is the starting position and so there can be no force acting on that either and therefore only the force acting on point P is required. Shifting the reference frame to have its origin at the centre of mass of the molecule we get,

$$f_{\mathrm{p}}^{\alpha} = -\frac{d\phi}{d\boldsymbol{y}_{\mathrm{p}}^{\alpha}}. \tag{6.11}$$

The resultant force has its direction perpendicular to the vector $\hat{\boldsymbol{y}}_{\mathrm{p}}$and lies in the plane shared by points O, C and P. So the direction of the force on the atom is given by

$$\begin{aligned} \hat{\boldsymbol{f}}_{\mathrm{p}} &= |\hat{\boldsymbol{y}}_{\mathrm{p}} \times (\hat{\boldsymbol{y}}_{\mathrm{p}} \times \hat{\boldsymbol{y}}_0)| \\ &= |\hat{\boldsymbol{y}}_{\mathrm{p}} \times \hat{\boldsymbol{z}}_0|, \end{aligned} \tag{6.12}$$

using $\boldsymbol{z}_0 = \boldsymbol{y}_{\mathrm{p}} \times \boldsymbol{y}_0$ which is apparent from Figure 6.2. This force produces a torque on the molecule whose direction is along $\boldsymbol{z}_0$,

$$\hat{\boldsymbol{\tau}}_{\boldsymbol{z}_0} = \hat{\boldsymbol{y}}_{\mathrm{p}} \times \hat{\boldsymbol{f}}_{\mathrm{p}}. \tag{6.13}$$

The torque acts on the molecule as a whole, and from it the forces on individual atoms can be calculated. Remembering that as per the metadynamics algorithm, the magnitude of the force comes from the derivative of the biasing potential, $\frac{dV_{\mathrm{b}}}{ds}$, the total force on an atom, k, in the molecule is given by

$$\boldsymbol{f}_{\mathrm{k}} = \frac{1}{\sum k}\frac{dV_{\mathrm{b}}}{ds}\frac{1}{|\boldsymbol{y}_{\mathrm{k}}|}(\boldsymbol{y}_{\mathrm{k}} \times \boldsymbol{z}_0), \tag{6.14}$$

where $\boldsymbol{y}_{\mathrm{k}}$ is the vector pointing from the centre of mass of the molecule to atom k but projected onto the $\boldsymbol{x}_0\boldsymbol{y}_0$ plane.

6.4 Computational method

The metadynamics algorithm was added into the DLPOLY 2.20 [90] MD code. DLPOLY is a modular program, making the addition of the new metadynamics module straight

forward. This module (contained within the file, metadynamics.f) contains all of the metadynamics subroutines, so that only minimal additions were needed to be made to the existing DLPOLY code. These additions are shown in Figure 6.4 in the context of the full MD algorithm. The full code for these subroutines is given in Appendix B.

The implementation reads the metadynamics options from the CONTROL file that is used as input for the rest of the DLPOLY options. The form of the calculation (the normal implementation or smoothly converging form of the algorithm) and the type of collective variable used, as well as the number of dimensions it acts over (limited to 1–3 depending on the type of CV), can all be changed directly in the CONTROL file. The parameters w, δs and τ_{G}, as well as ΔT, are also specified there.

Two methods of storing the metadynamics positions were implemented. The first is the conventional method, where the positions of the Gaussians in CV space (and their height if it is variable, as in the smoothly converging method) are stored in a list. Each time the derivative of the metadynamics potential is calculated, which takes place at every time step, this list is iterated over and the contributions summed from each (see Equation 6.5). In the second method a histogram is used to store the positions of the added Gaussians, so that when a new one is added its height is simply added to the correct bin in the histogram. The force calculation is therefore limited to a fixed number of calculations (each bin in the histogram), and so has a benefit in speed over the list method for longer simulations (i.e. when the list is longer than the number of bins in the histogram). This histogram method comes at the cost of accuracy because of the error introduced when the Gaussian positions are assigned to a histogram bin. A command in the CONTROL file allows either of these techniques to be chosen if there is a one-dimensional CV space, while only the list method is implemented for higher order spaces. For all of the results presented here the list option was used to avoid introducing unnecessary error, and to allow the results for the one and three dimensional CV space to remain as comparable as possible.

The metadynamics module was also designed to make it easy to add in new types of calculations. So, to incorporate a new type of collective variable, all that is needed are two new subroutines: one that can calculate the position of the meta variable at a particular timestep, and a second that can apply the correct forces onto the appropriate

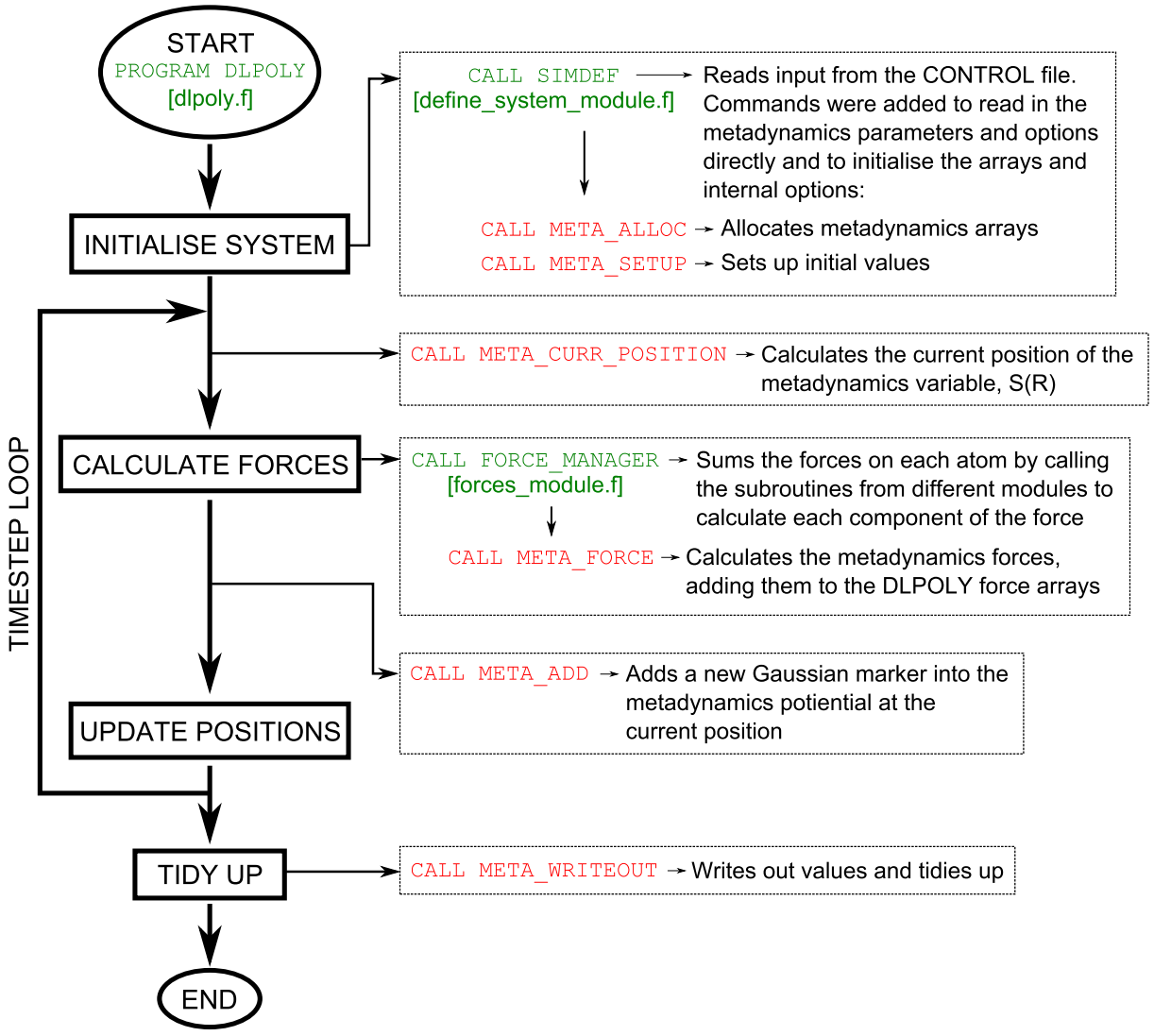

Figure 6.4: A simplified version of the MD algorithm (left) showing the modifications made in order to implement metadynamics (right). Only the subroutines that were modified are mentioned explicitly, labeled green along with the file that contains them and an explanation of what they do. The subroutines labeled in red are contained in the metadynamics.f file and are what directs the metadynamics calculation.

atoms. Then, only slight changes to the meta_force and meta_curr_position routines (which simply point to the correct force and position routines) are needed and a new option introduced in the sim_def routine so that a new direction can be read from the CONTROL file.

6.5 Simulation details

To simplify the metadynamics calculations and ensure that the forces applied acted to rotate the molecules and not to distort them, simulations were run with rigid OFN molecules. The results were compared against the 100 ns MD run that was used for the previous work (see Chapter 5), which had flexible OFN molecules. Aside from the rigid nature of the molecules and the much shorter simulation length (5 ns), every other aspect of the simulation set up was identical to that described in Section 5, with the same force-field, long-range interactions and thermostat. The same starting structure was also used, containing 144 OFN molecules with periodic boundary conditions in each direction. The cell was constructed with 4 x 6 x 6 molecules in the x, y and z directions respectively.

All of the simulations using rigid bodies were run at 290 K using DL_POLY 2.20 [90] and a 1 fs time step. For the long, unbiased simulation, 500 ps of equilibration was followed by 5 ns of production run, using trajectory snapshots from every 0.5 ps for use in the analysis. Metadynamics runs biased the orientation of one molecule (and its closest neighbours) that was picked to be near the centre of the simulation cell so that there were no problems with it jumping across periodic boundary conditions. Periodic boundary conditions were also used in the description of the collective variable, with forces from the biasing potential contributing from the nearest 180° in each direction of CV space. Runs used a variety of metadynamics parameters, which are quoted alongside the appropriate results in the following sections, and both the standard metadynamics algorithm and the smoothly converging form described above (labeled MT and SC respectively).

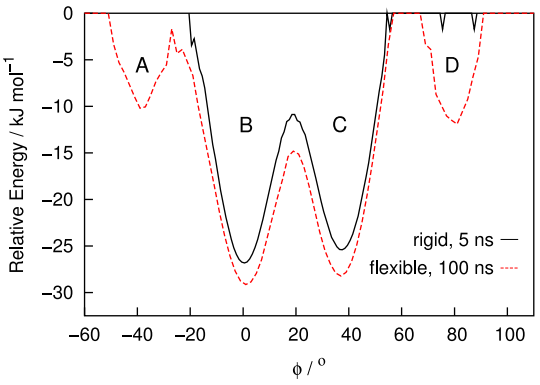

Figure 6.5: Comparison between the orientational energy profiles of the rigid and flexible unbiased simulations at 290 K. Averages were taken across all of 144 molecules in the simulation, giving effective sampling times of 77 ns and 14.4 μs for the rigid and flexible simulations respectively.

6.6 Results and discussion

To make certain that the use of rigid OFN molecules did not affect their orientational behaviour, a comparison is first made between the unbiased simulation of the rigid molecules and the long simulation of the flexible molecules that was used previously. The results, displayed in Figure 6.5, confirm that the shape of the energy profile and the size of the barriers appear to remain unchanged by the move to rigid bodies. The results also emphasize the poor sampling that is achieved by unbiased MD simulations at this temperature; neither simulation manages to completely explore these four wells, let alone climb over the barrier to undergo the complete rotation. It should be noted that the full rotation of the molecules *was* observed in higher temperature simulations, with a few of the 144 molecules overcoming the barrier in simulations at the (unphysical) temperature of 390 K.

The metadynamics results are now discussed: first, the algorithm is used to fully explore the rotational energy profile of a single OFN molecule, and secondly, the method is expanded into a multidimensional CV space and used to study the effect of correlated motion between neighbouring OFN molecules.

6.6.1 Metadynamics in one dimension: rotating a molecule

With the initial challenge being to fully explore the energy profile for the rotation of octafluoronaphthalene in its ambient temperature, solid form, metadynamics was performed using the orientation of one molecule as the only collective variable. Both the standard and well tempered forms of metadynamics were employed for the purpose of comparison and to help gain an understanding of the benefits and downfalls of each method. Although prior knowledge was available for the size and shape of the energy profile that was to be reconstructed (at least around the main wells), none was assumed. However, the symmetry of the OFN molecules about their C_2 rotation, means that the potential energy surfaces should also be symmetric around the point of the full rotation. This fact was used to define a point at which the simulations could be stopped (see Equation 6.15). The four main wells are labeled A–D as per Figure 6.5, while the positions related to these wells by the C_2 rotation are denoted with a prime.

Many preliminary simulations were done to investigate appropriate ranges for the metadynamics parameters. For all the simulations, the width of the Gaussian markers was restricted to between $\delta s = 5°$–$10°$ because this is approximately the width of the energy wells to be filled. The addition of wider Gaussian markers would smooth out the detail of the energy wells.

In the standard metadynamics simulations, there is a strong trade off between increasing the height of the Gaussian markers added, w, and losing accuracy in the final energy reconstruction, although using large values can lead to an extremely fast but coarse filling of the wells, which can be useful in an initial exploration of the CV space in unknown systems. Obtaining optimum parameters for this form of the algorithm required a lot of trial and error, as the response to changes in the variables was not that predictable. Optimum values were found to be in quite a specific region of the parameter space, with 0.010–0.025 kJ mol^{-1} for w and $\tau_G = 250$ ps. Only a single set of results using the standard metadynamics method are presented here, with $\tau_G = 250$ ps, $w = 0.010$ kJ mol^{-1} and $\delta s = 5°$ (labeled MT-250), because the smoothly converging scheme was found to be more efficient and accurate.

The smoothly converging form of the algorithm was found to be a lot easier to optimise, and reliable results were obtained from a wide range of parameters with a

predictable response on moving between different values. In the optimum conditions, ω (see Equation 6.7) was set to 1 kJ mol^{-1} ps^{-1} with a time interval between depositions of τ_G =100–500 ps. This led to an initial w for markers entered into unfilled wells of 0.1–0.5 kJ mol^{-1}, an order of magnitude higher than what could be used in the standard metadynamics simulations. ΔT values of between 300–2500 K were tested. The best results were found for values with $\Delta T = 900$ K and they are presented here as the results SC-100, SC-250 and SC-500, labeled according to the τ_G value used, with $\omega = 1$ kJ mol^{-1} ps^{-1} and $\delta s = 8°$.

As mentioned above, the inherent symmetry of the potential energy surface in this case provides an accurate way of deciding the best point to stop the simulation. Each time a new Gaussian was added a quantity χ was calculated, representing the absolute difference between the symmetry-related positions,

$$\chi = \sum_{\phi=-180}^{0} |F(\phi) - F(\phi + 180°)|, \tag{6.15}$$

with the endpoint of the simulation taken as the point where χ was a minimum (after the initial buildup). Figure 6.6 shows how this parameter varies with time as the wells are filled: there is an initial climb as wells A–D are filled, then once the molecule is pushed over the barrier to undergo the full rotation, wells A'–D' are filled and the value of χ reduces. There is a marked difference in how the MT and SC schemes behave. The MT scheme, in which the Gaussian volume is fixed, initially shows a linear dependence of χ on time as each set of wells is filled. For that simulation, the most symmetrical distribution is obtained as soon as both wells are filled (the lowest value of χ on each curve is circled), indicating that the optimum point to halt the algorithm is when the system undergoes a recrossing event back into a region that has already been visited and filled. Each of the SC simulations actually takes longer to reach a similarly symmetrical state, and they tend to overfill wells A–D (by an amount which is inversely proportional to τ_G) before undergoing the full rotation and exploring the other wells. Although they take longer, the SC simulations have the distinct advantage of converging towards the correct (symmetrical) answer, whereas the MT simulation fluctuates around it.

Figure 6.7 compares the different free energy profiles with that from the unbiased,

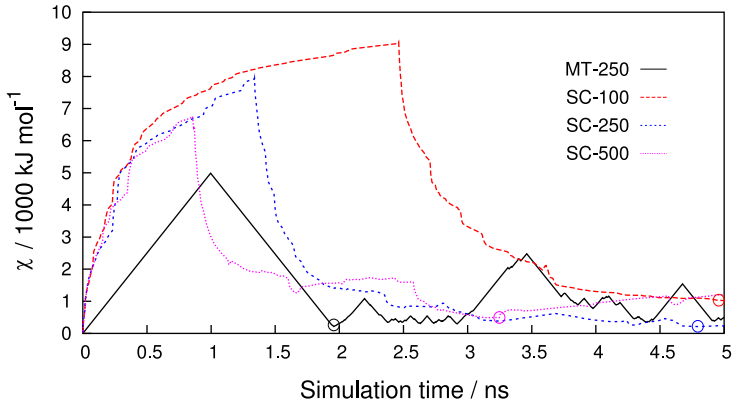

Figure 6.6: The evolution of the parameter ε (see Equation 6.15) with simulation time. The circled points on each curve are the points at which ϵ is a minimum and hence when the energy surface was most symmetrical. These were the points at which each simulation was stopped.

flexible, 100 ns simulation. The first point to note is that the simulations are accelerated considerably by the use of metadynamics. The unbiased simulation (with 100 ns of total simulation time and ensemble averages taken over an effective total of 14.4 μs sampling time) could only accurately deduce the barriers between positions B and C and although the two larger barriers into positions A and D were crossed, they were not sampled well enough to extract accurate barrier heights. The full rotation, not observed at all in the unbiased simulation with an effective sampling time of 14.4 μs, is seen in a metadynamics run of less than 2 ns. In fact, using coarser metadynamics parameters, the full rotation could be seen in less than 100 ps of simulation. This represents a speed-up of over 5 orders of magnitude in the total sampling time required, and 3 orders of magnitude in terms of raw simulation time.

Although the results look very different from each other in absolute magnitude, the various barriers, some of which are shown explicitly in Figure 6.8, do tend towards the same values and resemble the barriers obtained from the unbiased simulation. The underlying energy profile being explored in this case is quite complicated, with 8 wells to explore and a variety of different barriers of various heights. This is a more complicated energy surface than has been explored by most of the applications of metadynamics in the literature (where the energy profiles usually have just a few minima), but the accuracy with which it has been reproduced proves the method to be robust.

Another reason for the slight differences between the energy profiles is the existence

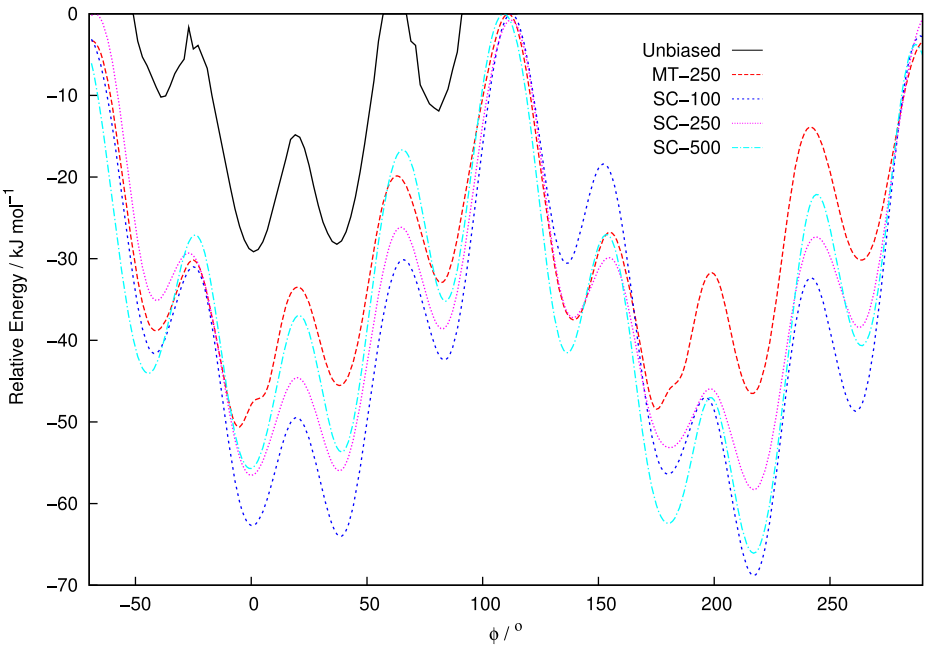

Figure 6.7: The 1D energy profiles resulting from the metadynamics simulations, compared with that calculated from 100 ns of unbiased simulation. Data were collected into histograms with a bin width of 1°.

of slower degrees of freedom that are not included in the CV. The free energy profile from the flexible simulation was actually a slice taken through the lowest energy pathway for the rotation in the 2D energy surface spanning the orientation ϕ, and the tilt of the molecule, θ. The orientation of the starting frame in the metadynamics definition of ϕ ensures that the molecules rotate along this lowest energy pathway, but if the molecule does tilt during the simulation then the energy barriers it experiences will vary. The extent of the variation should be limited because the bottlenecks along the pathway are quite wide, especially compared to the relatively narrow range of motion in θ. The fact that the barriers in Figure 6.8 are not too dissimilar to the unbiased results is also evidence for this.

There is also a second slow motion that is not accounted for in this one dimensional CV space, and that is the effect of correlations between neighbouring molecules, as discussed briefly in Chapter 5. These correlations serve to modify the energy barriers by a small amount (estimated previously to be in the region of ≈ 4 kJ mol^{-1}) depending on the relative orientations of the neighbours. In the results from those simulations

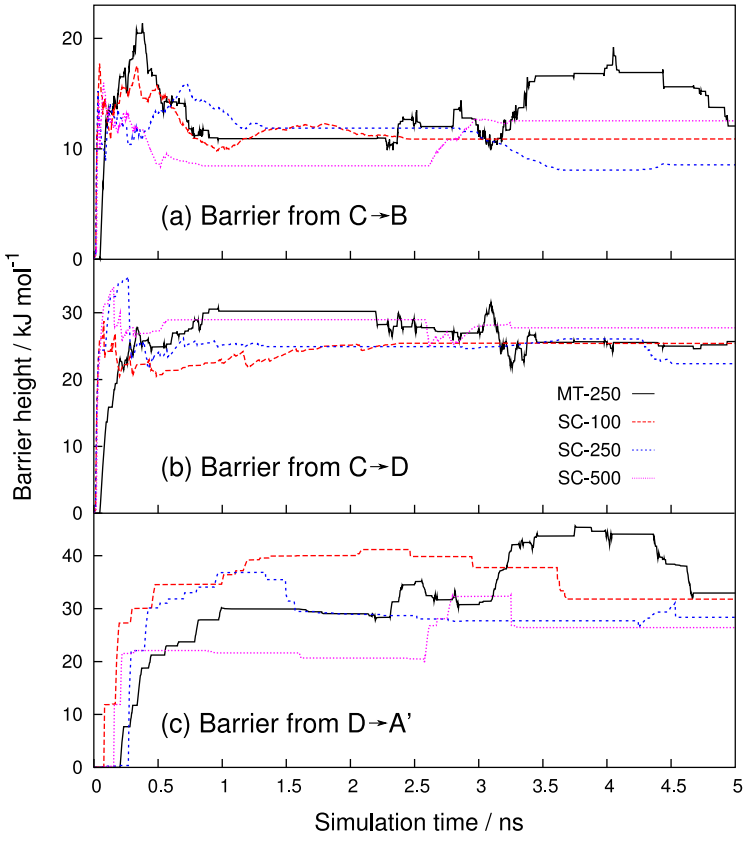

Figure 6.8: The variation of three of the rotational energy barriers as a function of the simulation time.

that have been presented here, the average was taken over all of the molecules in the system and so the effect of the correlations on the barrier heights will also be averaged out. In the metadynamics simulations a single molecule is rotated, so if its neighbours change orientation during the course of the simulation then the potential energy curve being explored will change, again introducing error.

Overall, the 1D results have shown how efficient the metadynamics algorithm is in accelerating rare events, but the absence of key degrees of freedom from the calculations prevents the results from being very accurate. This is due mostly to the fact that the system being studied displays complicated behaviour. However, one of the most appealing aspects of metadynamics is that it can, at least theoretically, be extended into an unlimited number of dimensions in the CV space, and thus investigate very complicated processes. In the following section metadynamics is used in three dimensions to study the correlated motion of neighbouring OFN molecules.

6.6.2 Metadynamics in three dimensions: studying correlated motions

Although techniques that efficiently explore free energy profiles are most frequently used to force rare events by pushing the system over high energy barriers, they can also be useful in exploring more subtle aspects of a system. To explore such phenomena an extensive exploration of phase space is required in order to resolve the differences between states that are similar in free energy. Here, metadynamics is used to investigate the effect of correlations between neighbouring OFN molecules in a vertical stack. The previous results from the unbiased MD simulations suggest that correlations do exist, serving to modify the barriers to rotation so that configurations where neighbouring molecules share the same orientation are preferred. However, collecting sufficient statistics in the unbiased MD simulation to explain the phenomenon proved to be extremely difficult, as it required the full set of orientational data to be split into poorly sampled subsets corresponding to different combinations of orientations. Here, this sampling problem is tackled using metadynamics, and is in itself a strong test of the algorithm given that the free energy surface is complicated and a high level of accuracy is needed.

In order to attempt to solve the problem directly, the CV space was expanded to include the orientation of three neighbouring molecules, with the definition of the orientations, ϕ, identical to that described previously, but all given with respect to the starting position of the middle molecule. Figure 6.9 shows the geometry of the system and the labels used. Gaussian markers were deposited in the space spanned by all three CVs.

Taking into account the full rotation of the molecule, eight wells would be expected in the orientational energy profiles of each molecule, making the 3D surface extremely complicated (with 8^3 wells in total). To minimise the complication, the calculations were modified to treat molecular orientations 180° apart from one another as being identical. The CV space could then be treated as being only 180° wide, but with periodic boundary conditions in the CV so that when a molecule rotated out of the bounds of the upper limit, it's image returns immediately within the lower bound. This

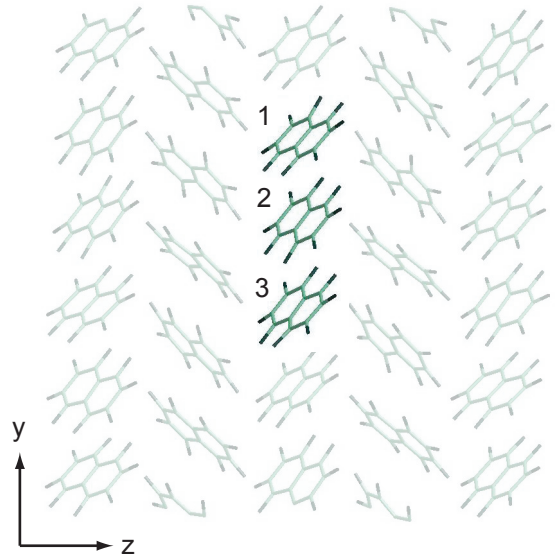

Figure 6.9: A schematic of the three molecules used in the metadynamics calculations. The orientation of each molecule is included as a separate collective variable.

is equivalent to filling up both sides of the potential at the same time, leaving only 4 energy wells in each dimension (64 in total).

The simulations were run with a variety of different parameters: simulations using the SC scheme were run with $\omega = 1$ kJ mol^{-1} ps^{-1} and $\delta s = 8°$ with ΔT values of 900, 1200 and 1500 K with τ_G =100 and 250 ps, whereas MT simulations were run with τ_{G} =250 ps, $w = 0.025$ kJ mol^{-1} for $\delta s = 5°$ and 8°. However, with no way to check the accuracy of the different simulations, picking the single "best" result out of the set was not possible. Instead, the average of all the energy surfaces was calculated. This was then compared to each of the individual simulations by evaluating the mean square difference between them. Simulations that differed most significantly from the mean were discarded and the rest were used to calculate a new mean energy surface, which was used in the analysis. The simulations that were furthest away from the average, and thus those that were not included in the final average, were both of the simulations running the MT scheme. The reason why these showed the largest deviation is most likely due to the much reduced Gaussian height that is required to get accurate estimates from the MT scheme, as it will considerably restrict the speed at which the CV space is sampled.

Figure 6.10 is a representation of the results obtained, showing slices through the

energy surface corresponding to the positions when molecule 2 (the middle molecule of the three) is sitting in the wells corresponding to positions A, B, C and D (see Figure 6.5 and the associated caption for the well labeling scheme). The most obvious observation in comparing these surfaces is that they are all different and therefore the orientation of a given molecule's neighbours *does* affect that molecule's preferred orientation. More subtly, it can be seen that the lowest energies correlate to instances when the neighbours are in similar positions to each other: the regions of lowest energy shift to higher ϕ_1 and ϕ_3 as ϕ_2 does (on moving from A$\rightarrow$D). The fact that such a subtle trend is observable suggests that a high level of sampling has been achieved. The symmetry in the surfaces and the fact that molecules 1 and 3 appear to behave almost identically, also suggest that the full surface is well sampled.

To explore the results further, slices were taken through the surfaces shown in Figure 6.10. These slices show the free energy surface of the labeled molecules when the other two molecules are in set positions (see Figure caption). The trend in Figure 6.11(a) is consistent with the idea that neighbouring molecules prefer to occupy similar positions, as discussed above, but the changes in the energy barriers are more clearly evident here. The orientation that molecule 2 assumes is seen to skew the energy profiles explored by molecules 1 and 3. This resembles a sort of switched ratchet system, where the closest neighbours to each molecule influence its preferred direction of rotation.

Determining the distance over which the correlations act is difficult, firstly because the metadynamics model used only contains three molecules, allowing complete control of the environment of the middle molecule only. The molecules at either end still interact with their neighbours that are not included in the calculations and therefore act (as in the one dimensional case) as slow degrees of freedom that can introduce error. The other limitation is that the simulation cell only contains 6 molecules along the y direction (see Figure 6.9) and so the nearest image of a given molecule from another one in the stack cannot exceed 3 positions. Nevertheless, an analysis was done to attempt to gain insight into the length of the correlations. This was to repeat the analysis displayed in Figure 6.11(a) but extract the energy profiles for one molecule when both of the other molecules were in the *same* position. The results, shown in

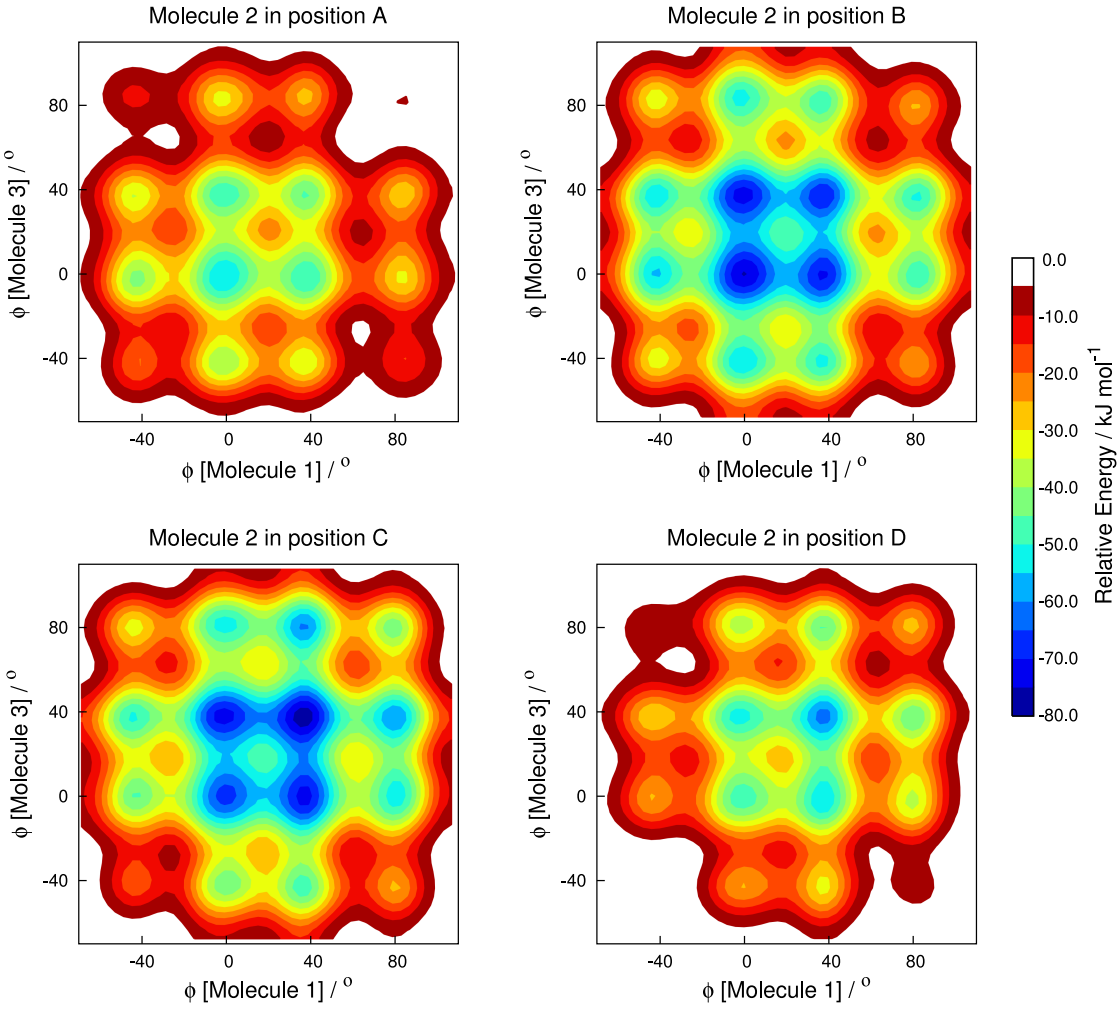

Figure 6.10: The 3D energy surface obtained directly from the metadynamics simulations was approximated using a 3D histogram with bins spanning 4° in each dimension. To visualise this data, 2D slices were taken through the energy surface, calculated from the conditional probability function $F_{\mathrm{G}}(\phi_1, \phi_3) \,|\, \phi_2 = X$, where X is given in the title of each plot, and corresponds the positions of the four wells A–D.

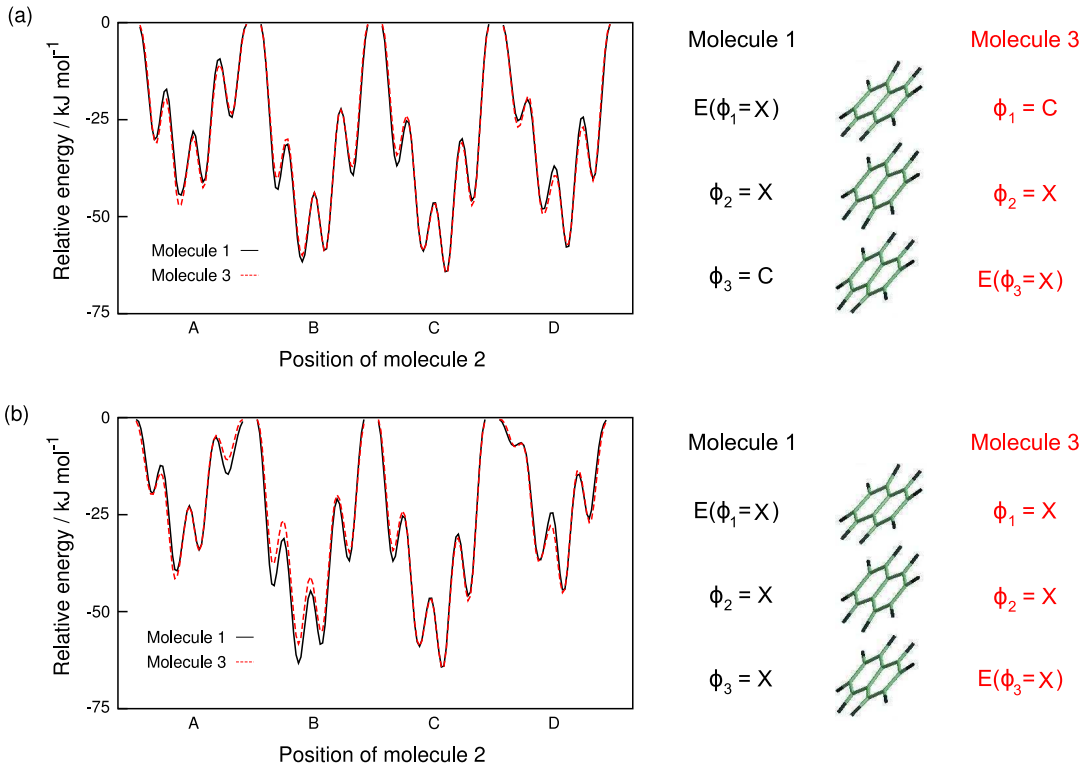

Figure 6.11: Slices taken through the average 3D potential energy surface obtained by metadynamics (all are shifted to have their maximum at 0 kJ mol^{-1}) and, alongside, illustrations of the scheme used for each diagram, with the colour-coding matching the lines in the plots. (a) The energy profiles for molecules 1 and 3 when the other of the two is in position C and molecule 2 is in the positions designated by the x-axis label (X). For molecule 1 this is equivalent to $F_{\mathrm{G}}(\phi_1)\,|\,\phi_3 = \mathrm{C}\,|\,\phi_2 = X$, and vice versa for molecule 3, where X corresponds to the positions A–D. (b) As in (a), but with both of the other molecules in the same orientation, so for molecule 1 this corresponds to $F_{\mathrm{G}}(\phi_1)\,|\,\phi_3 = \phi_1 = X$ and vice versa for molecule 3.

Figure 6.11(b), are almost identical to those from when only the immediate neighbour's orientation is varied, at least for positions B and C, indicating that the orientations of next nearest neighbours are essentially independent (but for their mutual dependence on their shared neighbour). The only changes when compared to Figure 6.11(a) are when the rare positions A and D are occupied, this could well be a sampling problem, as those positions in the free energy surface would be the most difficult to sample.

The mechanism of the correlations most probably originates in the favourable interactions between the fluorine atoms on one molecule and the pi-delocalisation of the ring system on its neighbour (mimicked by charge interactions in the MD). The geometry and the range of the forces dictate that this interaction should be limited to act between nearest neighbours and so the result above is expected. Longer range correlations are due to an orientational ordering of molecules through the crystal, requiring that the correlation is strong enough to 'communicate' the molecular orientations along the chain. Interestingly, this mechanism would seem to be the same as that which governs the second order phase transition from the ambient temperature form of OFN (the temperature at which the simulations were done) to the ordered phase III, in which there are two distinct stacks of molecules in the crystal, one containing only molecules in orientation B and the other molecules in orientation C. Presumably at the temperature of the phase transition, the energy offset caused by the correlation interaction begins to dominate and the molecules preferentially align. This shows not only that the interaction is strong enough to communicate over large distances, but also that the precise behaviour is controlled by temperature and thus that entropic contributions are key.

Although the form of the motion of individual molecules is quite simple and accessible to unbiased MD at elevated temperatures, the extent of the sampling required to fill the large, complicated, 3D space defined here rules out the use of standard MD. And yet, the use of metadynamics has allowed the energy surface to be explored fully, and accurately enough to show up subtle differences in molecular behaviour as the local environment of the molecules changes. Specifically, as its neighbour rotates into a new position, the rotational energy profile of a molecule is modified so as to favour a rotation towards the orientation of that neighbour.

6.7 Conclusion

The metadynamics algorithm has been implemented in the DLPOLY molecular dynamics code and used to force the rotation of a rigid octafluoronaphthalene molecule. In less than 5 ns of simulation, the method was able to explore the full energy profile for the rotation of the molecule; a feat that was not possible in 100 ns of unbiased simulation at the same temperature. By assigning the orientation of three neighbouring OFN molecules as separate collective variables it has also been possible to explore the effect of correlations between them and observe how the effective rotational energy profile of a given molecule changes depending on the orientations of its closest neighbours. This second case is a good example of a phenomenon which requires extensive sampling in the MD in order to be understood completely, not because of the height of the barriers that must be overcome, but because the differences in energy are very slight and so an accurate sampling of the energy surface is needed to resolve them. It has been shown that metadynamics is suitable to obtain such an accurate sampling, even in a case such as this where the energy surface has a complicated topology.

As with most molecular behaviour, the correlations observed here are statistical in nature because the slight changes in energy that are associated with the preferred states will only result in a very slight bias in their relative populations. This bias may be observable in the bulk properties of the system, but when studying a single molecule it is only apparent over a long time period. Therefore, incorporating such a process into a molecular machine results in a mechanism that is very different than those observed in conventional machines. However, this fundamental difference is a necessary one, so understanding the complete set of interactions for all the components of a given molecular machine is vital to map the most likely motional pathways. It has been shown here how suitable metadynamics is in exploring such molecular processes, and it should also be possible to extend the method to account for each degree of freedom in a given molecular machine as a separate collective variable so that the full energy surface for the machine's function can be reconstructed. The vast reduction in computational cost should also make elaborate analyses more feasible, such as variable temperature studies that would yield information on the entropic contributions to the free energy.

Chapter 7

Concluding remarks and outlook

The aim of this thesis was to demonstrate the utility of NMR and MD simulation to characterise motion in the solid state, and to show that the information each can provide is highly complementary, so that combining both techniques can lead to new insight in to the nature of dynamic processes in the solid state. The investigation of the OFN system presented in Chapter 5 demonstrates these ideas perfectly, as the final understanding of the complicated form of the motion of the molecules would not have been possible without evidence from both techniques. This system also shows the importance of the microscopic dynamical behaviour in describing the macroscopic properties of some solids, as it seems that the dynamic disorder present in the stacks of the octafluoronaphthalene molecules is intimately linked to the form of at least one of the low temperature phase transitions.

Although very slow molecular motions on the timescale of microseconds were observed by the MD simulations of OFN, even slower motions observed by the NMR were not sampled at all in the ambient temperature simulations. This limitation illustrates the utility of extended time scale MD techniques, which can reconcile the time-scales available to MD with the slower motions that can readily be accessed by NMR experiments. The OFN system provided the perfect case on which to test new methodology, and the recently introduced metadynamics algorithm was successfully implemented in the DLPOLY simulation package for this purpose, as described in Chapter 6.

The algorithm, which was developed to explore the free energy surface for the rotation of rigid (octafluoronaphthalene) molecules, shows a considerable acceleration

of up to five orders of magnitude in the speed at which the simulations sample rare events. The effect of correlations was found to influence the accuracy of rotational energy profiles found for single molecules. However, the efficiency of the method allowed these extra degrees of freedom to be accounted for explicitly, by expanding the calculation to obtain the free energy surfaces explored simultaneously by sets of neighbouring molecules. Even these extremely complicated energy surfaces can be explored efficiently by the method in a relatively short simulation time, and their estimations were accurate enough to show up systematic trends caused by the correlated motion of the molecules. The results in Chapter 6 demonstrate how robust the metadynamics algorithm is, as it can be applied to very different systems to explore widely different types of motional process. This is the first time it has been applied to the reorientation of whole molecules, an implementation that could have future use exploring the function of systems such as crystalline molecular machines.

Another aspect of this work has been to show that the comparison between NMR and MD results can also serve to validate the MD simulation, enabling it to be reliably used to study more detailed aspects of a system than could ever be accessed by experiment. Chapter 4 shows the level of detail that is available, although the methods by which the simulations can be linked to NMR results are only discussed and not used for a direct validation. Instead, confidence in the accuracy of the simulation is obtained through careful set up, comparison to XRD results, and the fitting of key interactions to *ab initio* results. This leads to a quality of simulation that is better than anything available in the literature for these classes of compounds. Analysis of the simulations shows the subtle behaviour of the structure and dynamics of both the host and guest molecules. For instance, it is shown that the confinement of the guest molecules introduces a correlation between their internal dihedral conformations. The MD even resolves extremely weak correlations between the positions of the guest molecules in neighbouring tunnels. The mechanism for this process is unclear, although extending the scope of the study to include simulations of urea hosts containing other types of guest molecule, with different charged or sterically-imposing constituent groups would be interesting and give a strong clue to the root cause of the effect.

Bibliography

[1] Paddy, M. R.; Dahlquist, F. W.; Dratz, E. A.; Deese, A. *Biochemistry* **1985**, *24*, 5988.

[2] Salmon, A.; Dodd, S. W.; Williams, G. D.; Beach, J. M.; Brown, M. F. *J. Am. Chem. Soc.* **1987**, *109*, 2600–2609.

[3] Huber, T.; Rajamoorthi, K.; Kurze, V. F.; Beyer, K.; Brown, M. F. *J. Am. Chem. Soc.* **2002**, *124*, 298–309.

[4] Shi, L.; Cembran, A.; Gao, J.; Veglia, G. *Biophys. J.* **2009**, *96*, 3648–3662.

[5] Hoff, B.; Strandberg, E.; Ulrich, A. S.; Tieleman, D. P.; Posten, C. *Biophys. J.* **2005**, *88*, 1818–1827.

[6] Sefcik, M. D.; Schaefer, J.; Stejskal, E. O.; McKayJeffrey, F.; Robert, A.; Dodd, S. W.; Brown, M. F. *Biochem. Biophys. Res. Comm.* **1983**, *114*, 1048–1055.

[7] Lindahl, E.; Edholm, O. *J. Chem. Phys.* **2001**, *115*, 4938.

[8] Pastor, R. W.; Venable, R. M.; Feller, S. E. *Acc. Chem. Res.* **2002**, *35*, 438–446.

[9] Vogel, A.; Tan, K. T.; Waldmann, H.; Feller, S. E.; Brown, M. F.; Huster, D. *Biophys. J.* **2007**, *93*, 2697–2712.

[10] Vogel, A.; Reuther, G.; Roark, M. B.; Tan, K. T.; Waldmann, H.; Feller, S. E.; Huster, D. *Biochim. Biophys. Acta* **2010**, *1798*, 275–285.

[11] Best, R. B.; Clarke, J.; Karplus, M. *J. Mol. Biol.* **2005**, *349*, 185–203.

[12] Gervasio, F. L.; Parrinello, M.; Ceccarelli, M.; Klein, M. L. *J. Mol. Biol.* **2006**, *361*, 390–398.

[13] Iwamura, H.; Mislow, K. *Acc. Chem. Res.* **1988**, *21*, 175–182.

[14] Bedard, T. C.; Moore, J. S. *J. Am. Chem. Soc.* **1995**, *117*, 10662–10671.

[15] Godinez, C. E.; Zepeda, G.; Mortko, C. J.; Dang, H.; Garcia-Garibay, M. A. *J. Org. Chem.* **2004**, *69*, 1652–1662.

[16] Feringa, B. L.; van Delden, R. A.; Koumura, N.; Geertsema, E. M. *Chem. Rev.* **2000**, *100*, 1789–1816.

[17] Kottas, G. S.; Clarke, L. I.; Horinek, D.; Michl, J. *Chem. Rev.* **2005**, *105*, 1281–1376.

[18] Karlen, S. D.; Garcia-Garibay, M. A. *Chem. Commun.* **2005**, 189–191.

[19] Albunia, A. R.; Gaeta, C.; Neri, P.; Grassi, A.; Milano, G. *J. Phys. Chem. B* **2006**, *110*, 19207–19214.

[20] Dominguez, Z.; Dang, H.; Strouse, M. J.; Garcia-Garibay, M. A. *J. Am. Chem. Soc.* **2002**, *124*, 7719–7727.

[21] Jarowski, P. D.; Houk, K. N.; Garcia-Garibay, M. A. *J. Am. Chem. Soc.* **2007**, *129*, 3110–3117.

[22] Dominguez, Z.; Khuong, T. A. V.; Dang, H.; Sanrame, C. N.; Nuñez, J. E.; Garcia-Garibay, M. A. *J. Am. Chem. Soc.* **2003**, *125*, 8827–8837.

[23] Zimmerman, H. E.; Zhu, Z. *J. Am. Chem. Soc.* **1994**, *116*, 9757–9758.

[24] Ilott, A. J.; Palucha, S.; Batsanov, A. S.; Harris, K. D. M.; Hodgkinson, P.; Wilson, M. R. *J. Phys. Chem. C* (in press).

[25] Ilott, A. J.; Palucha, S.; Batsanov, A. S.; Wilson, M. R.; Hodgkinson, P. *J. Am. Chem. Soc* **2010**, *132*, 5179–5185.

[26] Metropolis, N.; Rosenbluth, A. W.; Rosenbluth, M. N.; Teller, A. H.; Teller, E. *J. Chem. Phys.* **1953**, *21*, 1087–1092.

[27] Berendsen, H. J. C.; Postma, J. P. M.; van Gunsteren, W. F.; DiNola, A.; Haak, J. R. *J. Chem. Phys.* **1984**, *81*, 3684.

[28] Hoover, W. G. *Phys. Rev. A* **1985**, *31*, 1695–1697.

[29] Andersen, H. C. *J. Chem. Phys.* **1980**, *72*, 2384.

[30] Brown, D.; Clarke, J. H. R. *Mol. Phys.* **1984**, *51*, 1243–1252.

[31] Car, R.; Parrinello, M. *Phys. Rev. Lett.* **1985**, *55*, 2471–2474.

[32] Kaminski, G. A.; Friesner, R. A.; Tirado-Rives, J.; Jorgensen, W. L. *J. Phys. Chem. B* **2001**, *105*, 6474–6487.

[33] Weiner, S. J.; Kollman, P. A.; Nguyen, D. T.; Casse, D. A. *J. Comput. Chem.* **1986**, *7*, 230–252, The AMBER force field, as referenced by OPLS for their bond stretching and bending parameters.

[34] Brooks, B. R.; Bruccoleri, R. E.; Olafson, B. D.; States, D. J.; Swaminathan, S.; Karplus, M. *J. Comput. Chem* **1983**, *4*, 187–217.

[35] Martin, M. G.; Siepmann, J. I. *J. Phys. Chem. B* **1998**, *102*, 2569–2577.

[36] Van Gunsteren, W. F.; Berendsen, H. J. C. *Biomos, Groningen* **1987**,

[37] Halgren, T. A.; Damm, W. *Curr. Opin. Struct. Biol.* **2001**, *11*, 236–242.

[38] Torrie, G. M.; Valleau, J. P. *Chem. Phys. Lett.* **1974**, *28*, 578–581.

[39] Kirkwood, J. G. *J. Chem. Phys.* **1935**, *3*, 300.

[40] Kumar, S.; Rosenberg, J. M.; Bouzida, D.; Swendsen, R. H.; Kollman, P. A. *J. Comp. Chem.* **1992**, *13*, 1011–1021.

[41] Mezei, M. *J. Comput. Phys.* **1987**, *68*, 237–248.

[42] Laio, A.; Parrinello, M. *Proc. Natl. Acad. Sci. U. S. A.* **2002**, *99*, 12562.

[43] Apperley, D. C.; Harris, R. K.; Hodgkinson, P. *Solid-state NMR: Basic Principles and Practice*; In press, 2011; Chapter 4.

[44] Duer, M. *Solid-state NMR spectroscopy*; Wiley Online Library, 2002; Chapter 2.

[45] Duer, M. *Solid-state NMR spectroscopy*; Wiley Online Library, 2002; Chapter 6.

[46] Duer, M. *Solid-state NMR spectroscopy*; Wiley Online Library, 2002; Chapter 11.

[47] Fetterly, L. C. In *Non-Stoichiometric Compounds*; Mandelcorn, L., Ed.; Academic Press, New York, 1964; p. 491.

[48] Takemoto, K.; Sonoda, N. In *Inclusion Compounds*; Atwood, J. L., Davies, J. E. D., MacNicol, D. D., Eds.; Academic Press, New York, 1984; Vol. 2; p. 47.

[49] Harris, K. D. M. *J. Solid State Chem.* **1993**, *106*, 83–98.

[50] Harris, K. D. M. *Chem. Soc. Rev.* **1997**, *26*, 279.

[51] Guillaume, F. *J. Chim. Phys. PCB* **1999**, *96*, 1295–1315.

[52] Harris, K. D. M. *Supramol. Chem.* **2007**, *19*, 47–53.

[53] Smith, A. E. *Acta Cryst.* **1952**, *5*, 224–235.

[54] Harris, K. D. M.; Thomas, J. M. *J. Chem. Soc., Faraday Trans.* **1990**, *86*, 2985–2996.

[55] George, A. R.; Harris, K. D. M. *J. Mol. Graphics* **1995**, *13*, 138–141.

[56] Takemoto, K.; Sonoda, N. In *Inclusion Compounds*; Atwood, J. L., Davies, J. E. D., MacNicol, D. D., Eds.; Academic Press, New York, 1984; Vol. 2; p. 263.

[57] Yeo, L.; Harris, K. D. M. *J. Chem. Soc., Faraday Trans.* **1998**, *94*, 1633–1639.

[58] Harris, K. D. M. *J. Mol. Struct.* **1996**, *374*, 241–250.

[59] Rennie, A. J. O.; Harris, K. D. M. *J. Chem. Phys.* **1992**, *96*, 7117.

[60] Rennie, A. J. O.; Harris, K. D. M. *Proc. R. Soc. Lon. Ser-A* **1990**, *430*, 615–640.

[61] Aliev, A. E.; Harris, K. D. M.; Champkin, P. H. *J. Phys. Chem. B* **2005**, *109*, 23342–23350.

[62] Vold, R. L.; Hoatson, G. L.; Subramanian, R. *J. Chem. Phys.* **1998**, *108*, 7305.

[63] Imashiro, F.; Kuwahara, D.; Nakai, T.; Terao, T. *J. Chem. Phys.* **1989**, *90*, 3356–3362.

[64] Kim, S.; Kuroki, S.; Ando, I. *J. Chem. Phys.* **2006**, *323*, 545–552.

[65] Lu, J.; Mirau, P. A.; Tonelli, A. E. *Prog. Polym. Sci.* **2002**, *27*, 357–401.

[66] Odin, C.; Garcia, P. *Magn. Reson. Chem.* **2004**, *42*, 687–694.

[67] Davies, J. E. D.; Tabner, V. A. *J. Incl. Phenom. Macro.* **1998**, *31*, 99–107.

[68] El Baghdadi, A.; Dufourc, E. J.; Guillaume, F. *J. Phys. Chem* **1996**, *100*, 1746–1752.

[69] El Baghdadi, A.; Guillaume, F. *J. Raman Spectrosc.* **1995**, *26*, 155–166.

[70] Cannarozzi, G. M.; Meresi, G. H.; Vold, R. L.; Vold, R. R. *J. Phys. Chem.* **1991**, *95*, 1525–1527.

[71] Casal, H. L.; Cameron, D. G.; Kelusky, E. C. *J. Chem. Phys.* **1984**, *80*, 1407.

[72] Brustolon, M.; Maniero, A. L.; Marcomini, A.; Segre, U. *J. Mater. Chem* **1996**, *6*, 1723–1729.

[73] Brustolon, M.; Maniero, A. L.; Segre, U. *J. Chem. Soc. Perkin Trans. 2* **1997**, 2519–2524.

[74] Souaille, M.; Guillaume, F.; Smith, J. C. *J. Chem. Phys.* **1996**, *105*, 1529–1536.

[75] Casal, H. L. *J. Phys. Chem* **1990**, *96*, 2232–2234.

[76] Smart, S. P.; Baghdadi, A. E.; Guillaume, F.; Harris, K. D. M. *J. Chem. Soc., Faraday Trans.* **1994**, *90*, 1313–1322.

[77] Parsonage, N. G.; Pemberton, R. C. *Trans. Faraday Soc.* **1967**, *63*, 311–328.

[78] Chatani, Y.; Taki, Y.; Tadokoro, H. *Acta Cryst. B* **1977**, *33*, 309–311.

[79] Fukao, K. *J. Chem. Phys.* **1990**, *92*, 6867.

[80] Lynden-Bell, R. M. *Mol. Phys.* **1993**, *79*, 313–321.

[81] Yeo, L.; Kariuki, B. M.; Serrano-Gonzalez, H.; Harris, K. D. M. *J. Phys. Chem. B* **1997**, *101*, 9926–9931.

[82] Le Lann, H.; Odin, C.; Toudic, B.; Ameline, J. C.; Gallier, J.; Guillaume, F.; Breczewski, T. *Phys. Rev. B* **2000**, *62*, 5442–5451.

[83] Souaille, M.; Guillaume, F.; Smith, J. C. *J. Chem. Phys.* **1996**, *105*, 1516–1528.

[84] Souaille, M.; Smith, J. C.; Guillaume, F. *J. Phys. Chem. B* **1997**, *101*, 6753–6757.

[85] Lee, K. J.; Mattice, W. L.; Snyder, R. G. *J. Chem. Phys.* **1992**, *96*, 9138–9143.

[86] Menziani, M. C.; Benedetti, P. G.; Brustolon, M. *Mol. Phys.* **1997**, *92*, 903–912.

[87] George, A. R.; Harris, K. D. M. *J. Mater. Chem.* **1994**, *4*, 1731–1735.

[88] Antonioli, G.; McMillan, D. E.; Hodgkinson, P. *Chem. Phys. Lett.* **2001**, *344*, 68–74.

[89] Shannon, I. J.; Harris, K. D. M.; Rennie, A. J. O.; Webster, M. B. *J. Chem. Soc., Faraday Trans.* **1993**, *89*, 2023–2029.

[90] Smith, W.; Forester, T. *J. Mol. Graph.* **1996**, *14*, 136.

[91] Frisch, M. J. et al. Gaussian 03. Gaussian Inc., Wallingford, CT, 2004.

[92] Stephens, P. J.; Devlin, F. J.; Ashvar, C. S.; Chabalowski, C. F.; Frisch, M. J. *Faraday Discuss.* **1994**, *99*, 103–119.

[93] Rassolov, V. A.; Ratner, M. A.; Pople, J. A.; Redfern, P. C.; Curtiss, L. A. *J. Comput. Chem.* **2001**, *22*, 976–984.

[94] Schmider, J.; Muller, K. *J. Phys. Chem. A* **1998**, *102*, 1181–1193.

[95] Harris, K. D. M.; Jonsen, P. *Chem. Phys. Lett.* **1989**, *154*, 593–598.

[96] Guillaume, F.; Sourisseau, C.; Dianoux, A. *J. Chim. Phys.* **1991**, *88*, 1721–1739.

[97] Guillaume, F.; Smart, S. P.; Harris, K. D. M.; Dianoux, A. J. *J Phys-Condens Mat.* **1994**, *6*, 2169.

[98] Girard, P.; Aliev, A. E.; Guillaume, F.; Harris, K. D. M.; Hollingsworth, M. D.; Dianoux, A. J.; Jonsen, P. *J. Chem. Phys.* **1998**, *109*, 4078.

[99] Allen, M. P.; Tildesley, D. J. *Computer simulation of liquids*; Clarendon Press, 1989.

[100] Neal, M. P.; Solymosi, M.; Wilson, M. R.; Earl, D. J. *J. Chem. Phys.* **2003**, *119*, 3567.

[101] Harris, K. D. M.; Hollingsworth, M. D. *Proc. R. Soc. Lon. Ser-A* **1990**, *431*, 245–269.

[102] Harris, K. D. M.; Smart, S. P.; Hollingsworth, M. D. *J. Chem. Soc., Faraday Trans.* **1991**, *87*, 3423–3429.

[103] Brown, M. E.; Hollingsworth, M. D. *Nature* **1995**, *376*, 323–327.

[104] Collings, J. C.; Roscoe, K. P.; Thomas, R. L.; Batsanov, A. S.; Stimson, L. M.; Howard, J. A. K.; Marder, T. B. *New J. Chem.* **2001**, *25*, 1410–1417.

[105] Mehring, M.; Griffin, R. G.; Waugh, J. S. *J. Chem. Phys.* **1971**, *55*, 746.

[106] Harris, R. K.; Jackson, P.; Nesbitt, G. J. *J. Magn. Reson.* **1989**, *85*, 294–302.

[107] Robbins, A. J.; Ng, W. T. K.; Jochym, D.; Keal, T. W.; Clark, S. J.; Tozer, D. J.; Hodgkinson, P. *Phys. Chem. Chem. Phys.* **2007**, *9*, 2389–96.

[108] Akhmed, N. A. *Zh. Strukt. Khim.* **1973**, *14*, 573–574.

[109] Del Pra, A. *Acta Crystallogr. B* **1972**, *29*, 3433–9.

[110] Cozzi, F.; Bacchi, S.; Filippini, G.; Pilati, T.; Gavezzotti, A. *A. Chem. Eur.* **2007**, *13*, 7177–7184.

[111] Pawley, G. S.; Dietrich, O. W. *J. Phys. C* **1975**, *8*, 2549–2558.

[112] Mackenzie, G. A.; Arthur, J. W.; Pawley, G. S. *J. Phys. C* **1977**, *10*, 1133–1149.

[113] Bagryanskaya, I. Y.; Gatilov, Y. V.; Lork, E.; Mews, R.; Shakirov, M. M.; Watson, P. G.; Zibarev, A. V. *J. Fluor. Chem.* **2002**, *116*, 149–156, The most recent x-ray studies of ofn.

[114] Markley, J. L.; Horsley, W. J.; Klein, M. P. *J. Chem. Phys.* **1971**, *55*, 3604–5.

[115] Ryckaert, J. P.; Ciccotti, G.; Berendsen, H. J. C. *J. Comput. Phys.* **1977**, *23*, 327.

[116] Torchia, D.; Szabo, A. *J. Mag. Res.* **1982**, *49*, 107–121.

[117] Tycko, R. *Nuclear magnetic resonance probes of molecular dynamics*; Kluwer Academic Publishers, 1994; Chapter 2.

[118] Khoung, T. A. V.; Nunez, J. E.; Godinez, C. E.; Garcia-Garibay, M. A. *Acc. Chem. Res.* **2006**, 413–422.

[119] Kay, E. R.; Leigh, D. A.; Zerbetto, F. *Angew. Chem. Int. Ed.* **2007**, *46*, 72–191.

[120] Ikeuchi, S.; Miyazaki, Y.; Takeda, S.; Akutagawa, T.; Nishihara, S.; Nakamura, T.; Saito, K. *J. Chem. Phys.* **2005**, *123*, 044514.

[121] Stirling, A.; Iannuzzi, M.; Parrinello, M.; Molnar, F.; Bernhart, V.; Luinstra, G. A. *Organometallics* **2005**, *24*, 2533–2537.

[122] Ensing, B.; Klein, M. L. *Proc. Natl. Acad. Sci. U. S. A.* **2005**, *102*, 6755.

[123] Blumberger, J.; Ensing, B.; Klein, M. *Angew. Chem. Int. Ed.* **2006**, *45*, 2893–2897.

[124] Cucinotta, C. S.; Ruini, A.; Catellani, A.; Stirling, A. *ChemPhysChem* **2006**, *7*, 1229–1234.

[125] Rodriguez-Fortea, A.; Iannuzzi, M.; Parrinello, M. *J. Phys. Chem. B* **2006**, *110*, 3477–3484.

[126] Zipoli, F.; Bernasconi, M. *J. Phys. Chem. B* **2006**, *110*, 23403–23409.

[127] Nair, N.; Schreiner, E.; Marx, D. *J. Am. Chem. Soc.* **2006**, *128*, 13815–13826.

[128] Santarossa, G.; Vargas, A.; Iannuzzi, M.; Baiker, A. *Phys. Rev. B* **2010**, *81*, 174205.

[129] Ensing, B.; De Vivo, M.; Liu, Z.; Moore, P.; Klein, M. L. *Acc. Chem. Res* **2006**, *39*, 73–81.

[130] Spiwok, V.; Lipovová, P.; Králová, B. *J. Phys. Chem. B* **2007**, *111*, 3073–3076.

[131] Donadio, D.; Bernasconi, M. *Phys. Rev. B* **2005**, *71*, 73307.

[132] Karplus, M.; McCammon, J. A. *Nat. Struct. Biol.* **2002**, *9*, 646–652.

[133] Rhee, Y. M.; Pande, V. S. *Biophys. J.* **2003**, *84*, 775–786.

[134] Bussi, G.; Gervasio, F. L.; Laio, A.; Parrinello, M. *J. Am. Chem. Soc.* **2006**, *128*, 13435–13441.

[135] Piana, S.; Laio, A. *J. Phys. Chem. B* **2007**, *111*, 4553–4559.

[136] Babin, V.; Roland, C.; Darden, T. A.; Sagui, C. *J. Chem. Phys.* **2006**, *125*, 204909.

[137] Piccinini, E.; Ceccarelli, M.; Affinito, F.; Brunetti, R.; Jacoboni, C. *J. Chem. Theory Comput.* **2008**, *4*, 173–183.

[138] Prakash, M. K.; Barducci, A.; Parrinello, M. *Biophys. J.* **2010**, *99*, 588–594.

[139] Tribello, G. A.; Liew, C. C.; Parrinello, M. *J. Phys. Chem. B* **2009**, *113*, 7081–7085.

[140] Quigley, D.; Rodger, P. M. *J. Chem. Phys.* **2008**, *128*, 154518.

[141] Donadio, D.; Raiteri, P.; Parrinello, M. *J. Phys. Chem. B* **2005**, *109*, 5421–5424.

[142] Sun, J.; Klug, D. D.; Martovnák, R.; Montoya, J. A.; Lee, M. S.; Scandolo, S.; Tosatti, E. *Proc. Natl. Acad. Sci. U. S. A.* **2009**, *106*, 6077.

[143] Martoňák, R.; Laio, A.; Parrinello, M. *Phys. Rev. Lett.* **2003**, *90*, 75503.

[144] Pagliai, M.; Iannuzzi, M.; Cardini, G.; Parrinello, M.; Schettino, V. *ChemPhysChem* **2006**, *7*, 141–147.

[145] Khuong, T. A. V.; Nunez, J. E.; Godinez, C. E.; Garcia-Garibay, M. A. *Acc. Chem. Res.* **2006**, *39*, 413–422.

[146] Garcia-Garibay, M. A. *Proc. Natl. Acad. Sci. U.S.A.* **2005**, *102*, 10771.

[147] Min, D.; Liu, Y.; Carbone, I.; Yang, W. *J. Chem. Phys.* **2007**, *126*, 194104.

[148] Laio, A.; Rodriguez-Fortea, A.; Gervasio, F. L.; Ceccarelli, M.; Parrinello, M. *J. Phys. Chem. B* **2005**, *109*, 6714–6721.

[149] Wu, Y.; Schmitt, J. D.; Car, R. *J. Chem. Phys.* **2004**, *121*, 1193.

[150] Micheletti, C.; Laio, A.; Parrinello, M. *Phys. Rev. Lett.* **2004**, *92*, 170601.

[151] Barducci, A.; Bussi, G.; Parrinello, M. *Phys. Rev. Lett.* **2008**, *100*, 20603.

Appendix A

Modified force field parameters for the UIC simulation

The fitted parameters that were used to describe the torsion angles in the acid head group in the simulations of UIC are given in Table A.1, with the definitions of the potentials given in Equations A.0.1 and A.0.2. The atom labeling scheme is given in Figure 4.2.

$$U_{\cos 3}(\phi) = \frac{1}{2}\left[A_1(1+\cos\phi) + A_2(1-\cos 2\phi) + A_3(1+\cos 3\phi)\right] \tag{A.0.1}$$

$$U_{\text{plan}}(\phi) = A_1\left[1-\cos\phi\right] \tag{A.0.2}$$

Angle type	Atoms				A_1 / kcal mol^{-1}	A_2 / kcal mol^{-1}	A_3 / kcal mol^{-1}
cos3	C10	C11	C12	OC	-0.1540	1.7590	-0.3133
cos3	C10	C11	C12	OH	0.6555	-0.8686	-0.1856
cos3	OC	C12	OH	HO	0.0000	5.5000	0.0000
plan	OC	C12	OH	C11	500.0	-	-

Table A.1: Parameters used to describe the dihedral angles.

Appendix B

Fortran subroutines for the metadynamics algorithm

Here, the key subroutines are listed for the implementation of the metadynamics algorithm in DLPOLY.

Input

The metadynamics parameters and other control options are read in from the DLPOLY CONTROL file along with the other simulation parameters. Algorithm B.1 shows the code added into the simdef subroutine in the DLPOLY file, define_system_module.f. Below is a summary of the commands that can be read in, with the required parameters.

meta-step N_{dims} τ_{G} w

Initiate metadynamics in N_{dims} [INTEGER] dimensions. τ_{G} [INTEGER] is the number of timesteps between Gaussian additions and w [DOUBLE] is their initial height.

meta-option *option*

Sets the calculation type, where *option* [STRING] can take the following values:

- ofn1d rotate a single octafluoronaphthalene molecule ($N_{\text{dims}} = 1$)
- ofn2d rotate two octafluoronaphthalene molecules ($N_{\text{dims}} = 2$)
- ofn3d rotate three octafluoronaphthalene molecules ($N_{\text{dims}} = 3$)

meta-list *dim* δs s_{min} s_{max} *pbc*

Store the positions of the Gaussian markers in the list format. Parameters are set separately for each dimension of collective variable used, so that there should be N_{dims} meta-list directives in the CONTROL file, with the value of *dim* [INTEGER] numbered 1–N_{dims}. δs [DOUBLE] is the Gaussian width (a separate δs is taken for each dimension, but using different ones for each dimension is not currently implemented and the δs from $dim = 1$ is used for all). s_{min} [DOUBLE] and s_{max} [DOUBLE] are the lower and upper limits of the collective variable space in this *dim*. *pbc* [INTEGER] sets the behaviour of the periodic boundary conditions in this dimension and can take the following values:

0	no pbcs
1	pbcs - biasing potential is calculated from the nearest image of each Gaussian
2	as $pbc = 1$, but symmetry enabled so that states 180° apart from each other are treated identically (implemented specifically for OFN - see main text)

meta-hist *dim* δs s_{min} s_{max} N_{bins} *pbc*

Uses a histogram to store the positions of the Gaussian markers that have been added. Variables are identical to those listed above for the meta-list directive, with N_{bins} [INTEGER] extra, as the number of bins allocated for the histogram. The *dim* parameter is currently redundant because the histogram method is not implemented for $N_{\text{dims}} > 1$.

meta-smooth ΔT

Use the smoothly converging algorithm to control the Gaussian height added. ΔT [DOUBLE] corresponds to the tuning parameter as described by Equation 6.7 and the associated text.

meta_debug i

Sets debug level to value i [INTEGER].

Interface routines to DLPOLY

To allow new metadynamics calculations to be easily added, the subroutine calls that are required to be called from inside the DLPOLY routines, are as general as pos-

Algorithm B.1 Code added to the DLPOLY file define_system_module.f that reads in the metadynamics parameters from the standard CONTROL file.

```
! Include debugging options if we find it in field, default = 0
! this could be arranged better inside the metadynamics routines
! to have particular levels of output and for it to be consistent
! for different metadynamics options
elseif(findstring('meta-debug',directive,idum))then
  DEBUG_META = intstr(directive,lenrec,idum)
  write(*,*)"debug:",DEBUG_META
elseif(findstring('meta-smooth',directive,idum))then
  meta_DT = 1.0d0 / dblstr(directive,lenrec,idum)
  meta_smooth = .True.
elseif(findstring('meta-step',directive,idum))then
  proc = intstr(directive,lenrec,idum)
  meta_step = intstr(directive,lenrec,idum)
  meta_h  = dblstr(directive,lenrec,idum)
  call meta_alloc()
elseif(findstring('meta-hist',directive,idum))then
  meta_i = intstr(directive,lenrec,idum)
  meta_w(meta_i)  = dblstr(directive,lenrec,idum)
  meta_min(meta_i) = dblstr(directive,lenrec,idum)
  meta_max(meta_i) = dblstr(directive,lenrec,idum)
  meta_num = intstr(directive,lenrec,idum)
  meta_pbc(meta_i)  = intstr(directive,lenrec,idum)
  meta_hist_on = .TRUE.
elseif(findstring('meta-list',directive,idum))then
  meta_i = intstr(directive,lenrec,idum)
  meta_w(meta_i)  = dblstr(directive,lenrec,idum)
  meta_min = dblstr(directive,lenrec,idum)
  meta_max = dblstr(directive,lenrec,idum)
  meta_pbc(meta_i) = intstr(directive,lenrec,idum)
  meta_hist_on = .FALSE.
elseif(findstring('meta-option',directive,idum))then
!  go through the different metadynamics options
if(findstring('ofn1d',directive,idum))then
  meta_opt = 1
elseif(findstring('formoterol',directive,idum))then
  meta_opt = 2
elseif(findstring('ofn2d',directive,idum))then
  meta_opt = 3
elseif(findstring('ofnxz',directive,idum))then
  meta_opt = 4
elseif(findstring('ofn3d',directive,idum))then
  meta_opt = 5
else
  meta_opt = 0
  write(*,*)'NO METADYNAMICS OPTION GIVEN'
end if
call meta_setup()
```

Algorithm B.2 Listing of the meta_curr_position subroutine.

```
subroutine meta_curr_position(nstep)
implicit none

integer, intent(in) :: nstep
md_count = nstep

! first get the current position - depends on option
! [atom indices are hard coded at the moment]
if(meta_opt==1) then
  call ofn_posZ(1,1,18)     ! OFN rotation
else if(meta_opt==3) then
  call ofn_posZ(1,1,18)     ! OFN rotation in 2 molecules
  call ofn_posZ(2,1117,18)
else if(meta_opt==5) then
  call ofn_posZ(1,1,18)     ! OFN rotation in 3 molecules
  call ofn_posZ(2,1117,18)
  call ofn_posZ(3,1387,18)
end if

! now can work out the force from the biasing potential
if(proc==1) then          ! in 1D can use list or hist
  if(meta_hist_on) then
    call hist_Fbias(1)
  else
    call list_Fbias(1)
  end if
else if(proc>1) then      ! >1D only list is implemented
  call list_Fbias_ND()    ! different routine for >1D
else                      ! otherwise something went wrong
  call meta_error(6)
end if

return
end subroutine
```

sible and simply redirect the calculations depending on the options specified. There are three of these routines that take care of the main metadynamics calculations: meta_current_position (Algorithm B.2), that finds the current position(s) in the CV space and then calls the routines to find the force due to the current value of the biasing potential at that position, meta_force (Algorithm B.3) that calls the routines specific to the type of metadynamics calculation to apply the correct forces to the appropriate atoms, and meta_add (Algorithm B.4), that adds a new Gaussian into the biasing potential.

Algorithm B.3 Listing of the meta_force subroutine.

```
subroutine meta_force()
implicit none

! redirect to the correct force routine depending on meta-option
! atom numbers are hardcoded
if(meta_opt==1) then
  call ofn_forceZ(1,1,18)    ! OFN rotation
else if(meta_opt==3) then
  call ofn_forceZ(1,1,18)    ! OFN rotation in 2 molecules
  call ofn_forceZ(2,1117,18)
else if(meta_opt==5) then
  call ofn_forceZ(1,1,18)    ! OFN rotation in 3 molecules
  call ofn_forceZ(2,1117,18)
  call ofn_forceZ(3,1387,18)
end if

return
end subroutine
```

Algorithm B.4 Listing of the meta_add subroutine.

```
subroutine meta_add()
implicit none

double precision :: h
meta_count = meta_count + 1

! this is parinello's smoothly converging algorithm,
! h varies according to the potential at the current position
if(meta_smooth) then
  h = smooth_height()
else
  h = meta_h  ! otherwise just use constant height from input
end if

! redirect to either add to list or histogram
if(meta_hist_on) then
  call hist_add(h)
else
  call list_add(h)
end if

return
end subroutine
```

Algorithm B.5 Listing of the hist_add subroutine.

```
subroutine hist_add(h)
implicit none

integer :: ps
double precision, intent(in) :: h

! find the correct position in the histogram
! to add a gaussian to, using meta_position function
ps = meta_position(current_pos(1))
! then add 'h' to that position
meta_shist(ps) = meta_shist(ps) + h
! write out addition
write(meta_out,'(i8,f12.4,2f8.2)')ps,current_pos(1),h,meta_w(1)

return
end subroutine
```

General metadynamics routines

These subroutines perform the actual calculations.

Histogram

These routines are specific to the histogram implementation for storing the bias potential. hist_add (Algorithm B.5) adds a new Gaussian into one of the histogram bins, while hist_Fbias (Algorithm B.6) loops through the histogram to return the force that should be applied given the current position in CV space.

List

These routines are specific to the list implementation for storing the bias potential. list_add (Algorithm B.7) adds a new entry into the list containing the Gaussian position and height, while list_Fbias (Algorithm B.8) loops through the current values in the list to return the force that should be applied given the current position in CV space. list_Fbias_ND (Algorithm B.9) performs the same task, but will loop through lists with Gaussian positions in many different dimensions.

Algorithm B.6 Listing of the hist_Fbias subroutine

```
subroutine hist_Fbias(p)
implicit none

integer :: i
integer, intent(in) :: p
double precision :: force, lim, ds

! loops over the metadynamics histogram and add contributions
! to the force (differential of sum of gaussians at each point)
current_force(p) = 0d0
force = 0d0
lim = 6d0 * meta_w(p) ! only look at closest contributions

do i = 1,meta_num     ! loop over histogram bins
! find the distance, ds, of bin from the current position
  if(meta_shist(i)>0d0) then
    if(meta_pbc(p)>0) then ! is using pbcs for CV find nearest image
      ds = meta_nim(current_pos(p),meta_center(i),meta_min(p),meta_max(p))
    else
      ds = current_pos(p) - meta_center(i)
    end if
!   don't calculate anything if too far from the gaussian
    if(abs(ds)>lim) then
      continue
    else
!   calculate and sum the forces
      force=force+meta_shist(i)*ds*exp(-ds*ds*meta_wsq(p)*0.5d0)
    end if
  end if
end do

! transfer this force to the globel variable
! metarad converts into degrees
current_force(p) = force * metarad * meta_wsq(p)
write(*,*)"current force:",current_force(p),force,p

return
end subroutine
```

Algorithm B.7 Listing of the list_add subroutine.

```
subroutine list_add(h)
implicit none

integer :: i
double precision, intent(in) :: h

! add the new h into the list
! note: no separate h/w for different dims
meta_hlist(meta_count) = h
! write out the first part of the line first
write(meta_out,'(i8$)')meta_count

! then add the positions, one for each meta dimension
do i = 1, proc
  meta_list(meta_count,i) = current_pos(i)
  write(meta_out,'(f8.2$)')current_pos(i)
end do
write(meta_out,'(2f8.3)')h,meta_w(1)

return
end subroutine
```

Well tempered metadynamics

The only modification needed to implement the well tempered form of metadynamics is this smooth_height function (Algorithm B.10) that scales the height of the added Gaussians depending on the value of the biasing potential at the current position of the collective variable.

Specific calculations for OFN rotation

The ofn_posZ subroutine (Algorithm B.11) takes the atomic positions of an octafluoronaphthalene molecule and uses them to calculate the molecular frame, then compares this to the starting position to get the current orientation. The ofn_forceZ routine (Algorithm B.12) calculates the directions the force should be applied to for each atom in the OFN molecule, to produce an overall torque on the molecule that matches the force coming from the biasing potential. There is no force on the centre of mass of the molecule.

Algorithm B.8 Listing of the list_Fbias subroutine.

```
subroutine list_Fbias(p)
implicit none

integer :: i
integer, intent(in) :: p
double precision :: ds, h, lim, force

! loop over the list and add contributions to the force
! from the differential of sum of gaussians at each point
current_force(p) = 0d0
force = 0d0
lim = 6d0 * meta_w(p)

do i = 1,meta_count

! get the height straight from the hlist
  h = meta_hlist(i)

! work out nearest image if using pbcs in CV
  if(meta_pbc(p)>0) then
    ds = meta_nim(current_pos(p),meta_list(i,p),meta_min(p),meta_max(p))
  else
    ds = current_pos(p) - meta_list(i,p)
  end if

!  don't anything if are too far from the gaussian
  if(abs(ds)>lim) then
    continue
  else
!calculate and sum the forces
    force = force + h*ds * exp(-ds*ds*meta_wsq(p)*0.5d0)
  end if
end do

! save the result in the global variable
! meterad converts to degrees
current_force(p) = metarad * meta_wsq(p) * force

return
end subroutine
```

Algorithm B.9 Listing of the list_Fbias_ND subroutine.

```
subroutine list_Fbias_ND()
implicit none

integer :: i, j
double precision :: Fbias(proc)
double precision :: ds(proc), ld, f, lim, length

! loop over the metadynamics list and add contributions from each point
current_force = 0d0 ; Fbias= 0d0 ; f = 0d0
! limit to use for the gaussian positions
lim = 6d0 * 6d0 * meta_w(1) * meta_w(1)

! loop through the list of gaussians
do i = 1,meta_count
  length = 0d0
  do j = 1, proc
!   check for pbcs
    if(meta_pbc(j)>0) then
      ds(j) = meta_nim(current_pos(j),meta_list(i,j),&
              & meta_min(j),meta_max(j))
    else
      ds(j) = current_pos(j) - meta_list(i,j)
    end if
    length = length + ds(j)*ds(j)
  end do
! if we're too far away from the gaussian then skip calc
  if(length>lim) then
    continue
  else
!   find the absolute distance between the current pos and the gaussian
    ld = SQRT(length)
!   this is then used to get the force size from the gaussian
    f = meta_hlist(i)*ld*exp(-length*meta_wsq(1)*0.5d0)
    do j = 1, proc   ! add correct component to each dimension
      Fbias(j) = Fbias(j) + f * ds(j)/ld
    end do
  end if
end do
! save in glabal variables
do i = 1, proc
  Fbias(i) = metarad * meta_wsq(1) * Fbias(i)
  if(meta_pbc(i)==0) then ! if no pbcs, reflect force
    if((current_pos(i)<meta_min(i)).or.(current_pos(i)>meta_max(i)))then
      current_force(i) = -Fbias(i)
    else
      current_force(i) = Fbias(i)
    end if
  else
    current_force(i) = Fbias(i)
  end if
end do
return
end subroutine
```

Algorithm B.10 Listing of the smooth_height function.

```
function smooth_height()

double precision :: smooth_height, v

! meta_vbias returns the value of the biasing potential at the
! current position.
v = meta_Vbias(1)
! use this with other input values to scale h
smooth_height = meta_h * exp(-v*meta_DT) *  float(meta_step)

return
end function
```

Algorithm B.11 Listing of the ofn_posZ subroutine.

```
subroutine ofn_posZ(p,st,nat)
implicit none

double precision :: c1(3),proj(3), dp, molx(3),molz(3)
integer, intent(in) :: p, nat, st
integer :: i,j

! find the y vector
call mid_vec(st+1,st+2,st+6,st+7,meta_moly)
call norm(meta_moly)

! calculate full frame (only needed for 1 molecule)
if(p==1) then
! X and Z:
  call mid_vec(st,st+8,st+3,st+5,meta_molx) ; call norm(meta_molx)
  call cross(meta_molx,meta_moly,meta_molz) ; call norm(meta_molz)

! on first step save as the reference
  if(meta_fstep) then
!  do a few iterations to make sure the axes are orthogonal
    call cross(meta_moly,meta_molz,molx) ; call norm(molx)
    call cross(molx,meta_moly,molz)      ; call norm(molz)
    call cross(meta_moly,molz,meta_molx) ; call norm(meta_molx)
    call cross(meta_molx,meta_moly,meta_molz) ; call norm(meta_molz)
    do i = 1,3
      st_x(i) = meta_molx(i) ; st_y(i) = meta_moly(i)
      st_z(i) = meta_molz(i)
    end do
    meta_fstep = .FALSE.
  end if
end if

! find the projection of y(t) onto the plane x(0)y(0)
call cross(meta_moly,st_z,c1) ; call cross(st_z,c1,proj)

! now use this to find the angle with the starting position
dp = dot_product(proj,st_y)
if(dp>1d0) dp = 1d0 ! just to check
current_pos(p) = acos(dp)*metarad

! check which side of the dot product we're on
if(dot_product(proj,st_x)<0d0) current_pos(p) = 0d0 - current_pos(p)

! to make bias potential symmetric (ie 0==180 etc)
if(meta_pbc(p)==2) then
  if(current_pos(p)>90d0) current_pos(p)=current_pos(p)-180d0
  if(current_pos(p)<=-90d0) current_pos(p)=current_pos(p)+180d0
end if

return
end subroutine
```

Algorithm B.12 Listing of the ofn_forceZ subroutine.

```
subroutine ofn_forceZ(p,st,nat)
implicit none

integer :: i, fin
integer, intent(in) :: p, st, nat
double precision :: torque, atorque,l,f(3),at(3)
double precision :: yt(3),yp(3),yp1(3)

! get the total force, calculated previously
torque = current_force(p)

! if the contributions are too small just return
if((abs(torque)<0.000001).and.(.not.force_step1)) return

! divide the torque by the number of atoms
atorque = torque/real(nat)

! set up the indices of the atoms we are interested in
fin = st + nat - 1

! find the centre of mass:
meta_cofm = 0d0
do i = st, fin
    meta_cofm(1) = meta_cofm(1) + xxx(i)
    meta_cofm(2) = meta_cofm(2) + yyy(i)
    meta_cofm(3) = meta_cofm(3) + zzz(i)
end do
do i = 1,3
  meta_cofm(i) = meta_cofm(i) / real(nat)
end do

! Loop over the atoms in the molecule and find the forces
do i = st, fin
! find the vector pointing from CofM to the atom
  at(1) = xxx(i) ; at(2) = yyy(i) ; at(3) = zzz(i)
  call vdiff(meta_cofm,at,yt)
! get the projection, yp
  call cross(yt,st_z,yp1) ; call cross(st_z,yp1,yp)
  l = length(yp)
! force is cross product of yp with normal to plane
  call cross(yp,st_z,f) ; call norm(f)
! scale them according to vbias and so torques are equal
  f(1) = f(1) * atorque / l ; f(2) = f(2) * atorque / l
  f(3) = f(3) * atorque / l
! and add to dlpoly force arrays
  fxx(i) = fxx(i) + f(1) ;   fyy(i) = fyy(i) + f(2)
  fzz(i) = fzz(i) + f(3)
end do
if(force_step1) force_step1 = .false.

return
end subroutine
```